Title

Measuring transversity in polarized p+p collisions with di-hadron correlations at $\sqrt{s} = 200$ GeV at the STAR experiment

Permalink

https://escholarship.org/uc/item/2912v1xm

Author

Landry, Keith

Publication Date

2016

Peer reviewed|Thesis/dissertation

UNIVERSITY OF CALIFORNIA

Los Angeles

Measuring transversity in polarized p+p collisions with di-hadron correlations at $\sqrt{s} = 200$ GeV at the STAR experiment

by

Keith David Landry

2016

Abstract of the Dissertation

Measuring transversity in polarized p+p collisions with di-hadron correlations at
$\sqrt{s} = 200$ GeV at the STAR experiment

by

Keith David Landry
Doctor of Philosophy in Physics
University of California, Los Angeles, 2016
Professor Huan Z. Huang, Chair

The transversity distribution, $h_1(x)$, of a transversely polarized proton describes the probability of partons with polarization parallel to the parent proton, carrying a momentum fraction x of the parent proton. This distribution is fundamental for our understanding of the proton spin structure but still very much unknown for values of x larger than about 0.15. We study transversely spin-polarized proton collisions at $\sqrt{s} = 200$ GeV from STAR, because polarized p+p collisions at RHIC can access this x region and, with a higher scale and transverse momentum, probe a different kinematic regime than SIDIS. We find sizable spin asymmetries in di-hadron correlations, which can be used to directly probe the transversity distribution of quarks inside protons because they arise from a transversely spin polarized quark fragmenting into two hadrons by the Interference Fragmentation Function.

The dissertation of Keith David Landry is approved.

Zhongbo Kang

David Saltzberg

George Igo

Stephen Trentalange

Huan Z. Huang, Committee Chair

University of California, Los Angeles

2016

To my brother who has and continues to be an

incredible role model and great friend.

TABLE OF CONTENTS

LIST OF FIGURES

List of Tables

ACKNOWLEDGMENTS

I first want to thank my parents, who have always been so supportive of me in anything I do. I want to thank my advisor Huan Huang as well as Stephen Trentalange for thier guidence. I aslo want to thank collaborators Anselm Vossen, Renee Fatemi, and Kevin Adkins. Finally I would like to thank my friends who helped make my time at UCLA such a fantastic experience.

Vita

May 2009   Bachelor of Science, University of Massachusetts, Amherst

2011-2016   Research Assistant, UCLA Experimental Nuclear Physics Group

CHAPTER 1

Introduction

We have carried out measurements of asymmetries in pion pair production from spin polarized proton collisions, which will allow for the extraction of the transversity distribution function, a fundamental function intrinsic to the description of the proton's internal structure. In this chapter we will give an introduction to important historical milestones leading to the current state of affairs. Therefore before delving into my analysis, I will include a brief overview of the relevant physics and motivation.

1.1 Substructure of the atom

From the ancient philosophers to modern scientists, people have always been curious about the structure of matter. In the early 1800s John Dalton took the first major step down an even longer path. Dalton noticed that elements reacted in ratios of small whole numbers. As an explanation, he proposed the idea of atoms. The next step came in 1897 when J.J. Thomson discovered the electron. He observed that cathode rays would bend in the presence of a magnet and therefore concluded that the rays were actually streams of particles carrying an electric charge. He was able to measure the charge to mass ratio which turned out much larger than expected. This indicated that the mass of the particle was very small. He deduced this particle to be a constituent of the atom, but incorrectly proposed a "plum pudding model" where the electrons were suspended in the accompanying positive charge making the neutral atom. Thomson's incorrect model of the atom

was not adjusted until 1911 by Rutherford.

Rutherford challenged Thomson's model when he scattered alpha particles (not yet known to be helium nuclei) into a sheet of gold foil. If the plum pudding was correct, Rutherford expected the alpha particles to be deflected only slightly. What he observed was the opposite. Although most of the particles passed straight through, some of them were deflected wildly. This indicated the positive charge of the atom was concentrated in a very small nucleus. Rutherford named the nucleus of the lightest atom proton, but it was not until Chadwick discovered the neutron in 1932 other nuclei could be understood [24].

As heavier nuclei were being described as multiple protons and neutrons, a natural question came up. *What is holding the nucleus together?* In fact with multiple protons all positively charged, one would expect the nucleus to fly apart. There must be another stronger force keeping it together. This conveniently became known as the strong force. In 1934 Yukawa proposed a theory for the strong force. It had to be very short ranged as we don't feel its effects on a large scale. Because of this Yukawa proposed it was mediated by a heavy particle, much like the electromagnetic force is mediated by the photon. It wasn't until 1947 when Powell discovered Yukawa's predicted particle and named it the pion. At the same time another lighter particle was discovered that behaved similarly to an electron and given the name muon. The proton and neutron were grouped together and called baryons, or heavy weight particles, the electron and muon were light weight particles called leptons, and the pion was in between and classified as a meson [24].

1.2   Quantum Mechanical Spin

The Pauli exclusion principle and atomic spectra in the presence of an external magnetic field both hinted at the need for the electron to have another quantum

number. This was thought to be due to the electron spinning about an axis. Today we think of the electron as a point particle which cannot rotate, however the name "spin" stuck. The electron spin has an associated magnetic moment, which could naturally describe the atomic spectra seen from the Zeeman-effect.

$$\vec{\mu}_s = \frac{-ge}{2m_e}\vec{S} \approx \mu_B \tag{1.1}$$

The magnitude of the magnetic moment is approximately equal to the Bohr magneton. The difference is due to QED corrections.

The eigenvalues of the spin operators and its z component are

$$S^2|s, m_s\rangle = \hbar^2 s(s+1)|s, m_s\rangle \qquad S_z|s, m_s\rangle = \hbar m_s|s, m_s\rangle \tag{1.2}$$

As the spin-statistics theorem states, all particles with half integer spins are considered fermions, subject to the Pauli exclusion principle, and follow Fermi-Dirac statistics. All integer spin particles are considered bosons, follow Bose-Einstein statistics, and are allowed to occupy the same quantum states.

1.3 Nucleon Structure

Since the proton is a fermion with spin 1/2, it is expected to have a spin magnetic moment similar to that of the electron. Just as the electron's spin magnetic moment was approximately equal to the Borh magneton, the proton's spin magnetic moment was expected to be approximately equal to the nuclear magneton $\mu_N = e\hbar/2m_p$. However the measured value of the proton's spin magnetic moment is $\mu_p \approx 2.8\mu_N$. Moreover, the neutron's spin magnetic moment, which should be zero due to the neutron's lack of charge, was found to be $\mu_n \approx -1.9\mu_N$. These deviations from the expected values were unexplainable but hinted at the fact that nucleons were not elementary particles. This was not the only evidence that nu-
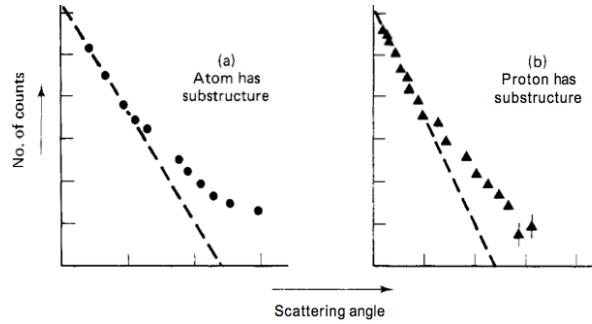
Figure 1.1: The dashed line shows expectation if positive charge was uniformly distributed in a) the atom and b) the proton [24].

cleons were not elementary. In a similar way Rutherford's scattering experiment suggested the positive charge was confined to a volume inside the atom which was much smaller than that for the negative charge, deep inelastic scattering experiments at SLAC showed evidence (Fig. 1.1) that the charge of the proton was not distributed uniformly. Instead there was evidence of three substructures in the proton. It wasn't until the quark model this could be explained.

1.4   quark model

In parallel with these developments, experiments detected particles that behaved differently from those currently known. In 1949 a neutral particle, eventually called the K^0, was found to decay into a π^+ and a π^-. In 1950 another neutral particle was found which decayed into a proton and a negatively charged pion. These newly discovered particles were labeled strange. By 1953 this strange label was found to be a quantum number that had to be conserved just like electric charge, which follows from the fact that these new strange particles are always created in pairs. In 1961 Gell-Mann was able to organize all the known particles using what he called the Eightfold Way. All the known mesons and baryons were arranged in a hexagon based on their electric charge and strangeness. Gell-Mann

went even further by proposing that these meson and baryons were actually composed of smaller particles called quarks. He used these quarks to explain why the mesons and baryons were able to be grouped so nicely. His model consisted of three quarks, the up quark, the down quark, and the strange quark. He also theorized these quarks were bound together by a force mediated by a gluon; a spin 1 boson. The quark makeup of the eight lightest baryons are shown in Table 1.1. Today we know that there are six quarks, not just the three that were originally proposed.

particle	quark content	rest mass	isospin	J^p	charge	strangeness
p	uud	938.27 MeV/c^2	1/2	1/2$^+$	+1	0
n	udd	939.57 MeV/c^2	1/2	1/2$^+$	0	0
Σ^+	uus	1189.37 MeV/c^2	1	1/2$^+$	+1	-1
Σ^0	uds	1192.64 MeV/c^2	1	1/2$^+$	0	-1
Σ^-	dds	1197.45 MeV/c^2	1	1/2$^+$	-1	-1
Λ^0	uds	1115.68 MeV/c^2	0	1/2$^+$	0	-1
Ξ^0	uss	1314.86 MeV/c^2	1/2	1/2$^+$	0	-2
Ξ^-	dss	1321.71 MeV/c^2	1/2	1/2$^+$	-1	-2

Table 1.1: The eight lightest baryons in the quark model

1.5 Electron-Proton Scattering and Structure Functions

The proton structure can be investigated through the study of electron-proton scattering. The differential cross section for electron-proton deep inelastic scattering, such as the experiments performed at SLAC, can be written in terms of two proton structure functions $W_1(Q^2, x)$ and $W_2(Q^2, x)$.

$$\frac{d\sigma}{d\Omega} = \left(\frac{d\sigma}{d\Omega}\right)_{mott} \left[2W_1 \tan^2\left(\frac{\theta}{2}\right) + W_2\right] \tag{1.3}$$

where $\left(\frac{d\sigma}{d\Omega}\right)_{mott}$ is the well-known Mott cross section.

In the deep inelastic scattering limit, where the momentum transfer $Q^2 \to \infty$ and proton momentum $p \to \infty$, but $x = -\frac{q^2}{2q \cdot p}$ stays fixed, Bjorken predicted the Q^2 dependence of the structure functions would disappear. We call this Bjorken scaling.

$$\lim_{Q^2 \to \infty, x \text{ fixed}} MW_1(Q^2, x) = F_1(x) \tag{1.4}$$

$$\lim_{Q^2 \to \infty, x \text{ fixed}} -\frac{q^2}{2Mx} W_2(Q^2, x) = F_2(x) \tag{1.5}$$

Although Bjorken scaling cannot hold exactly in any relativistic field theory [3], experiments have shown approximate Bjorken scaling. The structure functions in equations 1.4 and 1.5 can be written as $F_1(Q^2, x)$ and $F_2(Q^2, x)$ with the dependence on Q^2 being logarithmic. This can be seen in Fig. 1.2. It was found that Bjorken scaling up to logarithmic violations could be explained in asymptotically free field theories [25]. This led to the asymptotically free theory of Quantum Chromo Dynamics we have today.
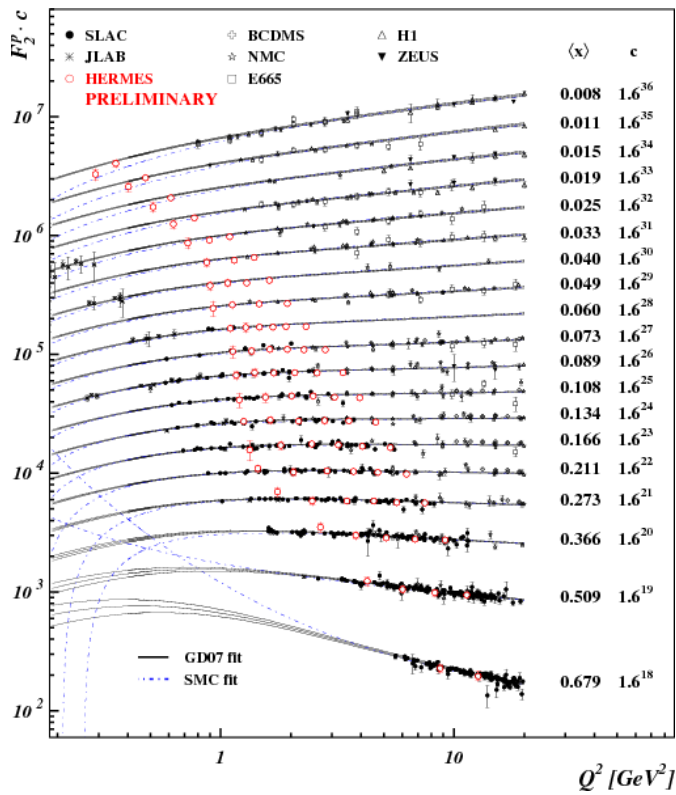
Figure 1.2: The proton stucture funtion shows approximate Bjorken scaling [39].

1.6 Factorization theorem and the unpolarized parton distribution function

The factorization theorem says that in the DIS limit, scattering occurs between free partons. Because of this, we are able build up the structure functions for the proton from distributions of its constituent partons.

$$F_1(Q^2, x) = \sum_a \int_x^1 \frac{d\xi}{\xi} f_a(\xi, \mu) H_{1a}\left(\frac{x}{\xi}, \frac{Q}{\mu}, \alpha_s(\mu)\right) + \text{ remainder} \tag{1.6}$$

$$\frac{1}{x} F_2(Q^2, x) = \sum_a \int_x^1 \frac{d\xi}{\xi} f_a(\xi, \mu) \frac{\xi}{x} H_{2a}\left(\frac{x}{\xi}, \frac{Q}{\mu}, \alpha_s(\mu)\right) + \text{ remainder} \tag{1.7}$$

Here $f_a(\xi, \mu)$ is the unpolarized parton distribution function of flavor "a". It gives the probability of finding a free quark for flavor a inside the proton with momentum fraction ξ. The renormalization scale, μ, is free to be chosen. The functions H_{1a} and H_{2a} are the hard scattering coefficients which can be calculated. The convenient choice of $\mu = Q$ will be used [20]. At leading order, the form of the structure functions simplify [24].

$$F_2(Q^2, x) = 2x F_1(Q^2, x) = \frac{1}{2} \sum_a e_a^2 f_a(x, Q) \tag{1.8}$$

Where e_a is the charge of parton a.

The factorization theorem can also be applied directly to the cross sections. In this manner, we can write the cross section of electron-proton scattering directly in terms of parton distribution functions and parton cross sections as seen in Fig. 1.3b.

$$\sigma_{ep} = \sum_a \int_x^1 d\xi f_a(\xi) \hat{\sigma}_{ea}\left(\frac{x}{\xi}, Q^2\right) \tag{1.9}$$

Where $\hat{\sigma}_{ea}$ is a calculable cross section for electron scattering off a parton of type a. In this way the factorization theorem can be generalized to other high energy processes [20]. The unpolarized distribution function $f_1(x)$ is well known. It can be extracted by fitting a large number of data points from different DIS experiments

(a) Electron proton scattering

(b) Scattering becomes electron off quark a in factorization picture
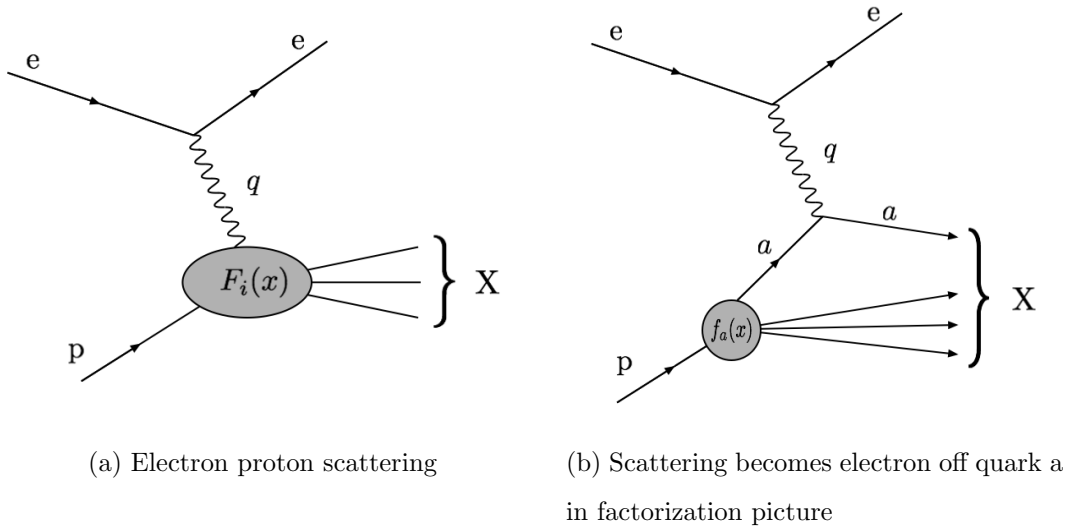
Figure 1.3: Factorization theorem of e + p → X

at different values of Q^2 and x [9]. In Fig. 1.4 the unpolarized distribution functions for different partons are shown. Not surprisingly partons carrying the largest momentum fraction x are the up quark and down quark.
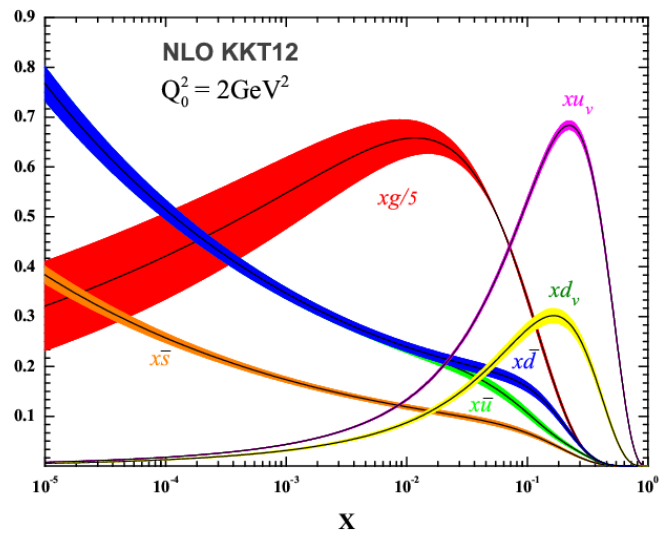
Figure 1.4: The unpolarized parton distribution functions as a function of x at initial scale $Q_0^2 = 2$ GeV^2 in the NLO approximation [9].

CHAPTER 2

Spin Physics

While the unpolarized distribution tells us some information about the number density of quarks inside a proton, it does not give a complete picture, and does nothing to answer the question about the origin of proton spin. For this we need to look at spin-dependent physics, which gives rise to spin-dependent parton distribution functions. One of which will be of interest in the remainder of this thesis.

2.1 Logintudinally Polarized Deep Inelastic Scattering

A good starting point for the study of spin physics is the polarized version of deep inelastic scattering. Specifically we are interested in a longitudinally polarized lepton beam scattering off of a longitudinally polarized proton. Similarly to the unpolarized case, we can describe it in terms of two structure functions G_1 and G_2. The difference in cross sections when the beam and proton are polarized in the same versus opposite directions is given by

$$\frac{\mathrm{d}^2\theta^{\overleftarrow{\leftarrow}}}{\mathrm{d}\Omega\mathrm{d}E'} - \frac{\mathrm{d}^2\theta^{\overleftarrow{\rightarrow}}}{\mathrm{d}\Omega\mathrm{d}E'} = \frac{4\alpha^2 E'}{Q^2 E}\left[(E + E'cos\theta)MG_1(\nu, Q^2) - Q^2 G_2(\nu, Q^2)\right], \quad (2.1)$$

where E and E' are the energies of the lepton in the initial and final states, $\nu = p \cdot q/M$, and G_1 and G_2 are spin-dependent structure functions. In the deep inelastic scattering limit the structure functions G_1 and G_2 can be written in terms

of dimensionless structure functions that show approximate Bjoken scaling [13].

$$\lim_{Q^2 \to \infty, x \text{ fixed}} M^2 G_1(\nu, Q^2) = g_1(x) \tag{2.2}$$

$$\lim_{Q^2 \to \infty, x \text{ fixed}} M\nu^2 G_2(\nu, Q^2) = g_2(x) \tag{2.3}$$

At leading twist[1], the contribution from g_2 vanishes. The spin-dependent structure function g_1 can be built up from parton distribution functions in the same way as the unpolarized structure functions. At leading order g_1 is given by

$$g_1(x, Q^2) = \frac{1}{2} \sum_a e_a^2 \left(\Delta f_a(x, Q^2) + \Delta \bar{f}_a(x, Q^2) \right). \tag{2.4}$$

Called the "helicity distribution function", Δf describes, in the infinite momentum frame of the proton, the number of quarks inside a longitudinally polarized proton with their spin aligned minus the number of quarks with their spin anti-aligned with the proton's spin, carrying momentum fraction x [13].

In 1997 the HERMES collaboration measured g_1 using a combination of inclusive and semi-inclusive lepton-nucleon deep inelastic scattering data [4]. The data was taken with 27.6 GeV longitudinally polarized positron beam scattering off a longitudinally polarized hydrogen gas target. They constructed a single spin asymmetry $A_\parallel$ in the number of scattered positrons.

$$A_\parallel = \frac{N^- L^+ - N^+ L^-}{N^- L_P^+ + N^+ L_P^-} \tag{2.5}$$

Where $N^+(N^-)$ is the number of positrons scattered when the target spin is parallel(antiparallel) to the positron beam spin. The luminosities are L^+, L^- when the target spin is parallel or antiparallel with the beam spin, while L_P^+, L_P^- are weighted luminosities. The structure function g_1 was extracted based on its relation to this asymmetry,

$$\frac{g_1}{F_1} = \frac{1}{1 + \gamma^2} \left[\frac{A_\parallel}{D} + (\gamma - \eta) A_2 \right] \tag{2.6}$$

---

[1] Twist t relates to order $1/Q^{t-2}$ [30]
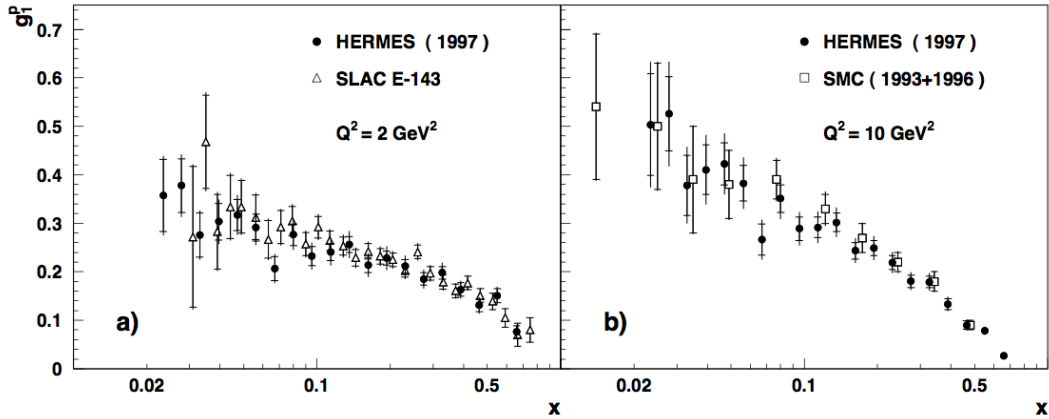
Figure 2.1: The helicity distribution as a function of momentum fraction x for Q^2 = 2 GeV^2 and 10 GeV^2 [4].

where $\gamma = 2Mx/\sqrt{Q^2}$. Here A_2 was previously measured to be small [4][1]. HERMES is not the only collaboration to extract the helicity distribution. The HERMES data, along with other data from other experiments, is shown in figure 2.1.

2.2   Proton Spin Crisis

However the spin of the proton comes about, it must be conceived from the spin of the quarks, Σ, the orbital angular momentum of the quarks, L_q, the orbital angular momentum of the gluons, L_g, and the spin of the gluon, ΔG. These must sum to equal the spin of the proton.

$$\frac{1}{2} = \frac{1}{2}\Sigma + L_q + L_g + \Delta G \qquad (2.7)$$

In the naive quark model, it was expected that the entirety of the proton spin would be carried by the three valence quarks. In a relativistic theory with QCD corrections, only about 60% of the proton spin is thought to be carried by the quarks. The initially measured value of $\int_0^1 \mathrm{d}x g_1(x)$, however corresponds to a value

of Σ of 0.120±0.16 or consistent with zero [32]. This suggests that virtually none of the proton spin in carried by valence quarks. More recent measurements provide a value of 0.27 ± 0.05 for Σ, still much smaller than the theoretical expectation from relativistic models [32].

It is possible that the contribution to proton spin from gluon spin is larger than previously thought. A global analysis of data from both STAR and PHENIX suggest the contribution from ΔG is sizable after all [23]. More data is needed to form a more conclusive answer.

2.3   Transversity Distribution Function

So far only logintudinal spin has been taken into account. Another piece to the proton spin puzzle deals with transverse spin. This can be described by another parton distribution function (written h_1 or $\Delta_T f$), which wasn't even considered until Ralston and Soper introduced it in 1979 [38], called the "transversity distribution function". This distribution function describes the number of quarks with their spin aligned minus the number of quarks with their spin anti-aligned with the proton's spin carrying momentum fraction x when the proton's spin is perpendicular to its direction of motion. One might think this is equivalent to the helicity distribution function as the probability of finding a parton whose spin is aligned versus anti-aligned with the proton spin shouldn't depend on the direction of the proton spin. This is true for a proton in its rest frame. However this interpretation of the helicity and transversity distributions are only viable in the infinite momentum frame of the proton. In a relativistic setting such as this, Lorentz boosts cause these distributions to differ [11].

Unlike the helicity distribution function, the transversity distribution function does not appear in lepton inclusive deep inelastic scattering due to its chiral-odd nature. In order to observe its effects, it must be paired with another chiral-odd

object to create a chiral-even observable, making it harder to access. Because of this, the transversity distribution function is currently not very well-known.

2.4 First Experimental Measurements of Transversity

2.4.1 In Single Hadron Production semi-inclusive DIS

The detection of a single hadron in the final state introduces another chiral-odd piece to the cross section in the form of a quark fragmentation function which describes how probable it is for a quark to fragment into a given hadron. When paired with the transversity distribution, a chiral-even observable is created, allowing the transversity distribution to be probed. This was first done by HERMES through semi-inclusive DIS of positrons off of a polarized proton target with a single hadron detected in the final state [5, 8],

$$e + p^\uparrow \rightarrow e + h + X. \tag{2.8}$$

Just as in the experiment to measure the helicity distribution, a single spin asymmetry was detected [5],

$$A_{UT}^h(\phi, \phi_S) = \frac{1}{|S_T|} \frac{N_h^\uparrow(\phi, \phi_S) - N_h^\downarrow(\phi, \phi_S)}{N_h^\uparrow(\phi, \phi_S) + N_h^\downarrow(\phi, \phi_S)} \tag{2.9}$$

where $N_h^{\uparrow(\downarrow)}(\phi, \phi_S)$ is the number of hadrons produced at azimuthal angle ϕ and angle ϕ_S to the proton spin when the spin is polarized up(down), and $|S_T|$ is the polarization of the target proton spin.

There are two sources of this asymmetry present in the cross section. These are the Collins azimuthal moment $\langle \sin(\phi + \phi_S) \rangle_{UT}^h$ and the Sivers moment $\langle \sin(\phi - \phi_S) \rangle_{UT}^h$. These were both measured and can be seen in figures 2.2a, 2.2b. From these transversity could be extracted [8].

Figure 2.2: Single Spin Asymmetry in SIDIS single hadron production measurements from HERMES [5]

(a) Measurement of Collins moment

(b) Measurement of Sivers moment
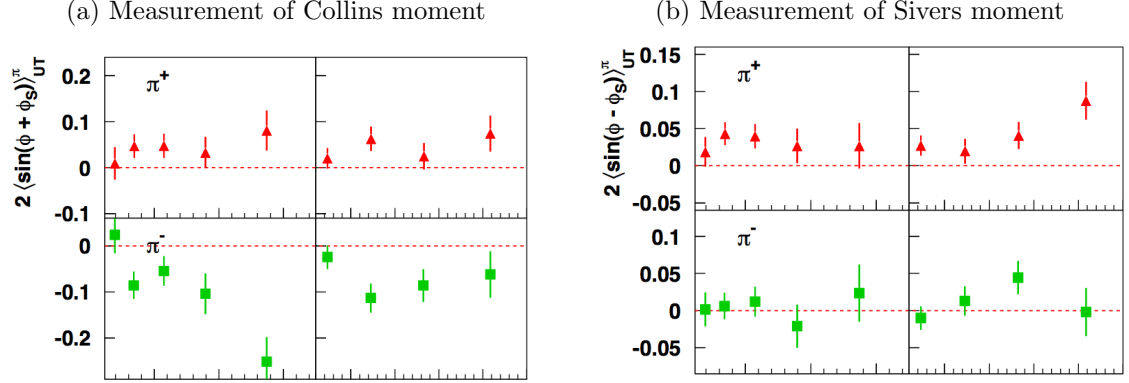
2.4.2 In Double Hadron Production semi-inclusive DIS

Quark fragmentation into two hadrons in the same jet, as described by the interference fragmentation function (IFF) and shown in Fig. 2.3, can also be paired with transversity to create a chiral-even observable [22, 15]. This was done by the COMPASS collaboration [17] and the HERMES collaboration [16] via the process

$$e + p^{\uparrow} \rightarrow e + (\pi^{+}, \pi^{-})_{jet} + X. \tag{2.10}$$
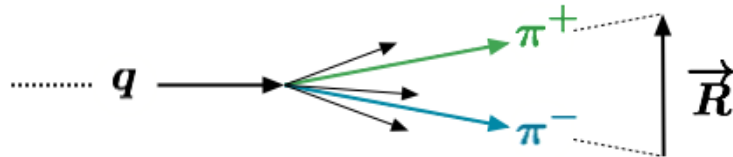
Figure 2.3: an outgoing quark fragments into a $\pi^{+}\pi^{-}$ pair. This is described by the Interference Fragmentation Function (IFF). The Vector $\vec{R}$ gives the orientation of the pair.
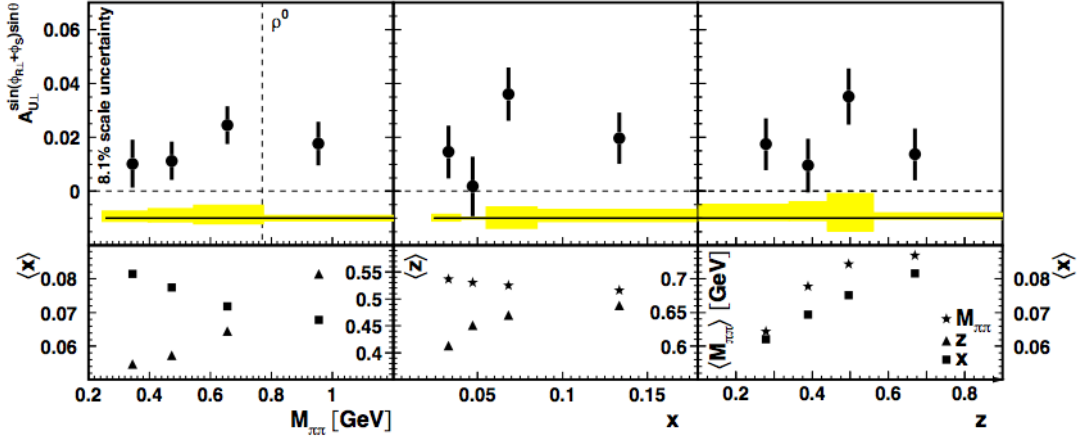
Figure 2.4: Single Spin Asymmetry measured by the HERMES collaboration [16]

Once again a singe spin asymmetry was measured. This is shown in figure 2.4 for HERMES data. This asymmetry is related to the transversity distribution by [16],

$$A_{UT}^{\sin(\phi_{R\perp}+\phi_S)\sin\theta} = -\frac{1-y}{1-y-\frac{y^2}{2}}\frac{1}{2}\sqrt{1-4\frac{M_\pi^2}{M_{\pi\pi}^2}}\frac{\sum\limits_q e_q^2 h_1^q(x)H_{1,q}^{\triangleleft,sp}(z,M_{\pi\pi})}{\sum\limits_q e_q^2 f_1^q(x)D_{1,q}(z,M_{\pi\pi})} \qquad (2.11)$$

where $y = (P\cdot q)/(P\cdot k)$, q and k are the momenta of the virtual photon and incoming positron respectively, $H_{1,q}^{\triangleleft,sp}(z,M_{\pi\pi})$ is the IFF describing the probability of transversely polarized quark q fragmenting into a pion pair with invariant mass $M_{\pi\pi}$ retaining momentum fraction z of the fragmenting quark, and $D_{1,q}(z,M_{\pi\pi})$ is the unpolarized partner of the IFF, $h_1^q(x)$ is the transversity distribution for parton q while $f_1^q(x)$ is the unpolarized parton distribution for parton q.

The asymmetry observed in this dihadron production does not depend on parton transverse momentum allowing it to be analyzed in the collinear framework. The single hadron production must be analyzed in the Transverse Momentum Dependent (TMD) framework. TMD factorization has been shown to depend on physical processes; however, collinear factorization is the same from process to process. This makes the asymmetry in dihadron production a useful observable

17

when comparing results in lepton scattering and hadronic collisions as well as when making predictions [35].

2.4.3 Transversity measurement in $p + p$ Collisions

There are several benefits in measuring the transversity distribution in proton-proton collisions as well. First of all, it can test the universality of the parton distributions. Furthermore, in proton-proton collisions, the momentum fraction carried by the interacting quarks is much higher than the fixed target SIDIS experiments previously discussed. This allows us to extend our knowledge we have of the transversity distribution into a new kinematic regime.

There are several ongoing measurements at STAR which are sensitive to the transversity distribution, and will thus test the consistency of the extracted transversity. One such experiment uses a single charged hadron, typically a pion, production $p^\uparrow + p \to \pi + X$ at mid-rapidity coupled to the Collins Fragmentation Function. Another is mid-rapidity W and Z boson production coupled to the Sivers Function. At forward rapidity, neutral pion production is sensitive to the transversity distribution through the Collins function.

The rest of this thesis will cover the measurement of transversity through double charged hadron production $p^\uparrow + p \to h_1^+ h_2^- + X$ at mid-rapidity. As mentioned in chapter 2.4.2, this is coupled with the Interference Fragmentation Function. Therefore in order to obtain useful information about the transversity distribution, we need a measurement of the IFF.

2.5 Measuring the Interference Fragmentation Function at BELLE

In our experiment, transversity only shows up as a convolution with the interference fragmentation function, $h_1 H_1^{\sphericalangle}$. In order to isolate transversity in our data we need to know how the interference fragmentation function behaves. The BELLE experiment at KEK has already done this work [42]. They performed an electron-positron annihilation experiment detecting back-to-back $\pi^+ \pi^-$ pairs. The relative angle between the two pions was determined and the modulation, a_{12}, of the number of back-to-back pairs found at different values of the relative angle was measured. This modulation, called the Artuo-Collins asymmetry, is related to two IFFs.

$$a_{12} \propto \frac{1}{2} \frac{\sin^2 \theta}{1 + \cos^2 \theta} \left[\sum_{q,\bar{q}} e_q^2 z_1^2 z_2^2 H_1^{\sphericalangle q}(z_1, m_1^2) H_1^{\sphericalangle \bar{q}}(z_2, m_2^2) \right]$$
$$\times \left[\sum_{q,\bar{q}} e_q^2 z_1^2 z_2^2 D^q(z_1, m_1^2) D^{\bar{q}}(z_2, m_2^2) \right]^{-1} \quad (2.12)$$

Here θ is the polar angle defined between the beam axis and the reference axis, D^q is the unpolarized equivalent of the IFF, $z_{1(2)}$ is the energy fraction pion pair 1(2) has, and $m_{1(2)}$ is the invariant mass of pair 1(2). BELLE reported the modulation a_{12} for different z_1, z_2 bins as well as different m_1, m_2 bins for different quark flavors [42]. The modulation a_{12} is shown in Fig. 2.5 plotted versus the invariant mass. With this data, Courtoy *et al* [10] were able to extract the Interference Fragmentation Function.
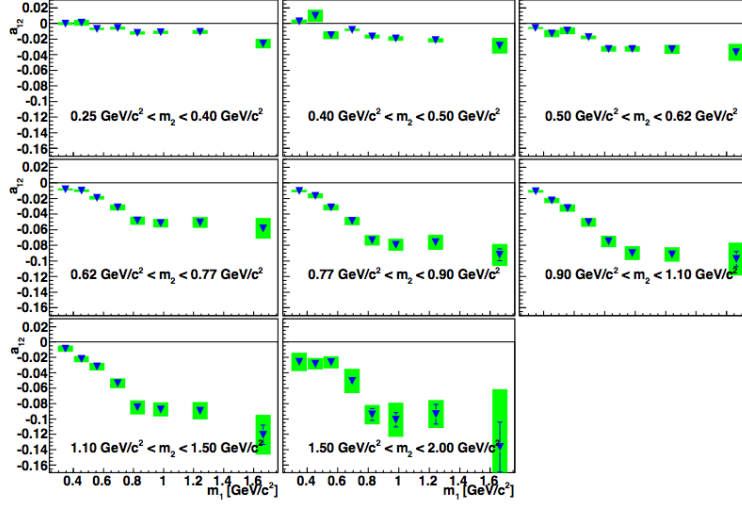
Figure 2.5: Asymmetry in the number of back-to-back pion pairs seen at BELLE plotted *vs* the invariant mass [42].

2.6 Extracting IFF

The interference fragmentation function was extracted from the BELLE data using the replica method [10]. N sets of replica data points were produced by shifting the experimentally determined data points by gaussian noise with the same width as the measured error. It was found that roughly 100 replicas were sufficient for the mean and standard deviation of the replicated data points to accurately reflect the measurements [36].

By integrating over the antiquark jet, the Arturo-Collins asymmetry from equation 2.12 becomes proportional to

$$a_{12} \propto \frac{H(z_1, m_1; Q^2)}{D(z_1, m_1; Q^2)}, \qquad (2.13)$$

where $D(z_1, m_1; Q^2)$ is estimated from PYTHIA calculations [21]. Restricting to only up and down quarks and requiring $n_u^\uparrow(Q^2) = -n_d^\uparrow(Q^2)$ gives

$$H(z_1, m_1; Q^2) = \frac{|\boldsymbol{R}|}{m_1} H_1^{\triangleleft u}(z_1, m_1; Q^2) n^\uparrow(Q^2). \qquad (2.14)$$

20
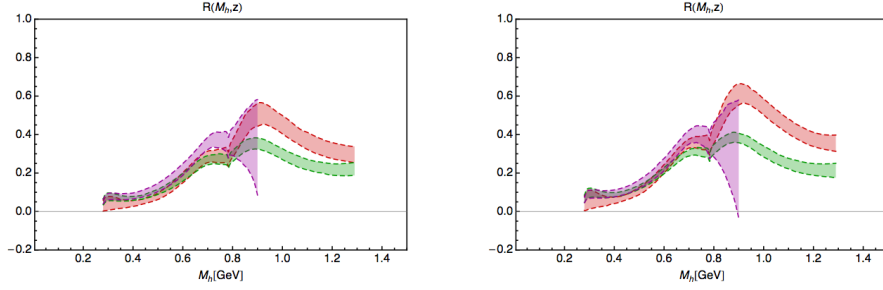
Figure 2.6: The ratio $R(z, M_h)$ as a function of M_h for three values of z: $z = 0.25$(purple), $z = 0.45$(green), and $z = 0.65$(red). The left panel is for $\alpha_s = 0.125$, and the right pannel is for $\alpha_s = 0.139$ [37]. Note: In their notation, $M_h = m_1$ is the invariant mass of the pion pair coming from the quark.

Here the normalization $n^\uparrow(Q^2) = \int dz \int dm_1 H(z_1, m_1; Q^2)$.

The theoretical value, $H^{TH}(z_1, m_1, Q^2; \{p\})$, is a complicated function [37] with parameter vector $\{p\}$ containing 9 parameters. These best-fit parameters were found for each replicated data set by minimizing the error

$$E_r^2(\{p\}) = \sum_{ij} \left(H_{ij}^{TH}(z_1, m_1, Q^2; \{p\}) - H_{ij}(z_1, m_1; Q^2) \right)^2 / \sigma_{ij}^2 \qquad (2.15)$$

where index i runs over the data points in invariant mass bin j. This results in $N = 100$ different parameter vectors. A value of $H_1^{\triangleleft u}(z_1, m_1; Q^2)$ is calculated from $H^{TH}(z_1, m_1, Q^2; \{p\})$ using the best fit parameters for each replica. The largest and smallest 16% of the N calculated values are rejected leaving a 68% confidence interval for the IFF.

$$R(z_1, m_1) = \frac{|\mathbf{R}|}{m_1} \frac{H_1^{\triangleleft u}(z_1, m_1; Q^2)}{D_1^u(z_1, m_1; Q^2)} \qquad (2.16)$$

To visualize the IFF, a ratio, which can be seen as a function of m_1 for different values of the fractional energy z in Fig. 2.6, is constructed. Each colored band represents one of these values of z and corresponds to 68% of the 100 replicas. Now armed with $H_1^{\triangleleft}$, we can access the transversity in our analysis.

21

2.7 Summary

To leading order, the parton kinematics inside a proton can be described by three parton distribution functions (Fig. 2.7); the unpolarized distribution function, $f_1(x)$, the helicity distribution function $\Delta f(x)$, and the transversity distribution function, $h_1(x)$ [28]. The first two are well-known from DIS experiments, while the transversity distribution is not. Due to its chiral odd nature, a different type of experiment is required to probe the transversity of partons inside the proton. The IFF, which is used to describe how a transversely polarized quark fragments into a pair of oppositely charged pions is used as the second chiral odd object to pair with the transversity distribution function in order to construct an observable. A more detailed overview of the physics involved in the analysis will be given in chapter 4.
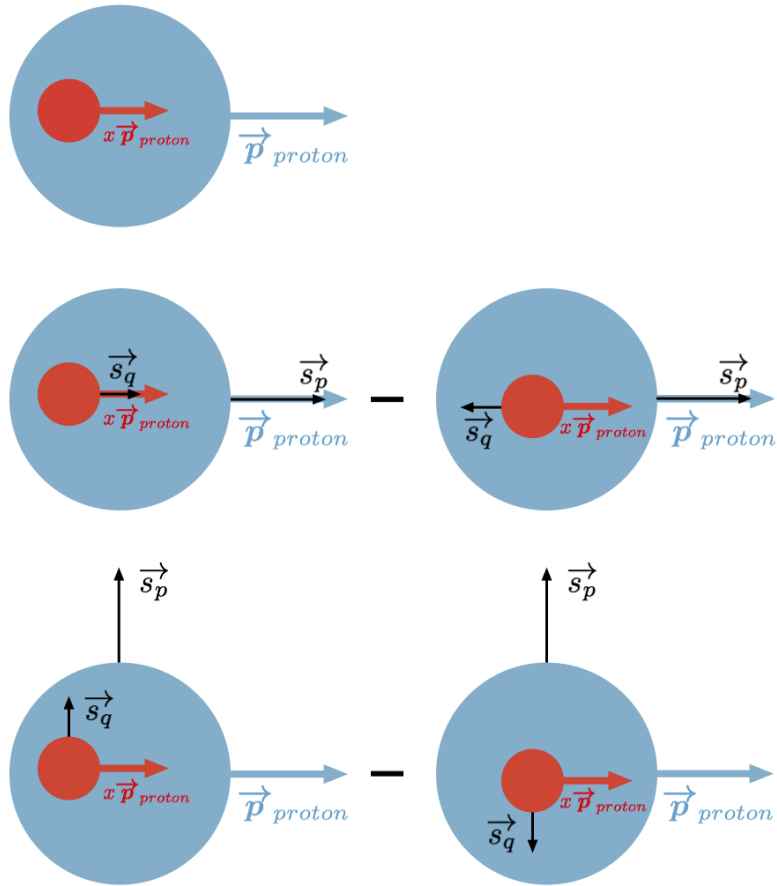
Figure 2.7: Top: Unpolarized distribution function $f_1(x)$

Middle: Helicity distribution function $\Delta f(x)$

Bottom: Transversity distribution function $h_1(x)$

CHAPTER 3

RHIC and The STAR Experiment

3.1 The RHIC complex

The Relativistic Heavy Ion Collider (RHIC), located at Brookhaven Nation Laboratory, is the only collider in the world that allows for spin-polarized proton collisions, as well as heavy nuclei collisions as the name suggests. The RHIC complex, shown in Fig. 3.1, is composed of a chain of accelerators which boost the energy in steps before finally injecting the particles into the large ring of RHIC. Heavy nuclei are first delivered to the Booster Synchrotron where they are accelerated to 95 MeV per nucleon. After which they are transferred to the Alternating Gradient Synchrotron (AGS). Here they are re-bunched into four bunches and accelerated to 10.8 GeV per nucleon, at which point they are injected into the RHIC ring and accelerated to their final energy. The highest energy RHIC can accommodate for heavy ions is 100 GeV per nucleon for gold nuclei. The story for protons is a little different. They are injected already spin polarized into the Booster Synchrotron from an older LINAC accelerator. From this point they are accelerated in the Booster and AGS before being injected into the RHIC storage ring. Here they are accelerated up to a maximum 250 GeV. In order to keep the spin polarization for the proton beam, special magnets called Siberian Snakes are used. These magnets flip the proton spin twice per revolution by 180 degrees in two orthogonal directions. The RHIC storage ring itself actually consists of two independent rings 3.8 km in circumference. This allows for the collisions of different species. The independent rings intersect at six locations. the STAR

detector is located at one such intersection points [33].

Acceleration of polarized protons in a circular accelerator can encounter resonant conditions which act to depolarize the beam. Special magnets called Siberian Snakes are used to overcome these depolarizing resonances. Each Siberian Snake consists of 4 superconducting helical dipole magnets. The role of the Siberian Snakes are to rotate the proton spin as shown in Fig. 3.2. If the spin rotation from the Siberian Snakes is much larger than that of the depolarizing resonances, the beam polarization is kept intact. In the RHIC ring, this is achieved with a pair Siberian Snakes in each ring which rotate the proton spin by 180 degrees in orthogonal directions for each orbit. The lower energy of the AGS calls for only partial Siberian Snakes which rotate less than 180 degrees, but still enough to maintain beam polarization [26]. Along with the Siberian Snakes, spin rotators are located at the experimental interaction points. These allow for the proton spin to be rotated from the transverse plane to the longitudinal plane before collisions, depending on the requirements of each experiments [26].

Polarized protons start out as polarized H^- ions produced from an optically pumped proton ion source (OPPIS). This source produces 9×10^{11} polarized H^- ions per 300μs pulse. These polarized ions are then accelerated to 200 MeV in the LINAC. They are then stripped of the electrons and injected into the Booster where they are further accelerated to 10.5 GeV. From here they are sent to the AGS and accelerated to 25 GeV. The final step is a transfer to RHIC for acceleration to a maximum of 250 GeV and storage [26].
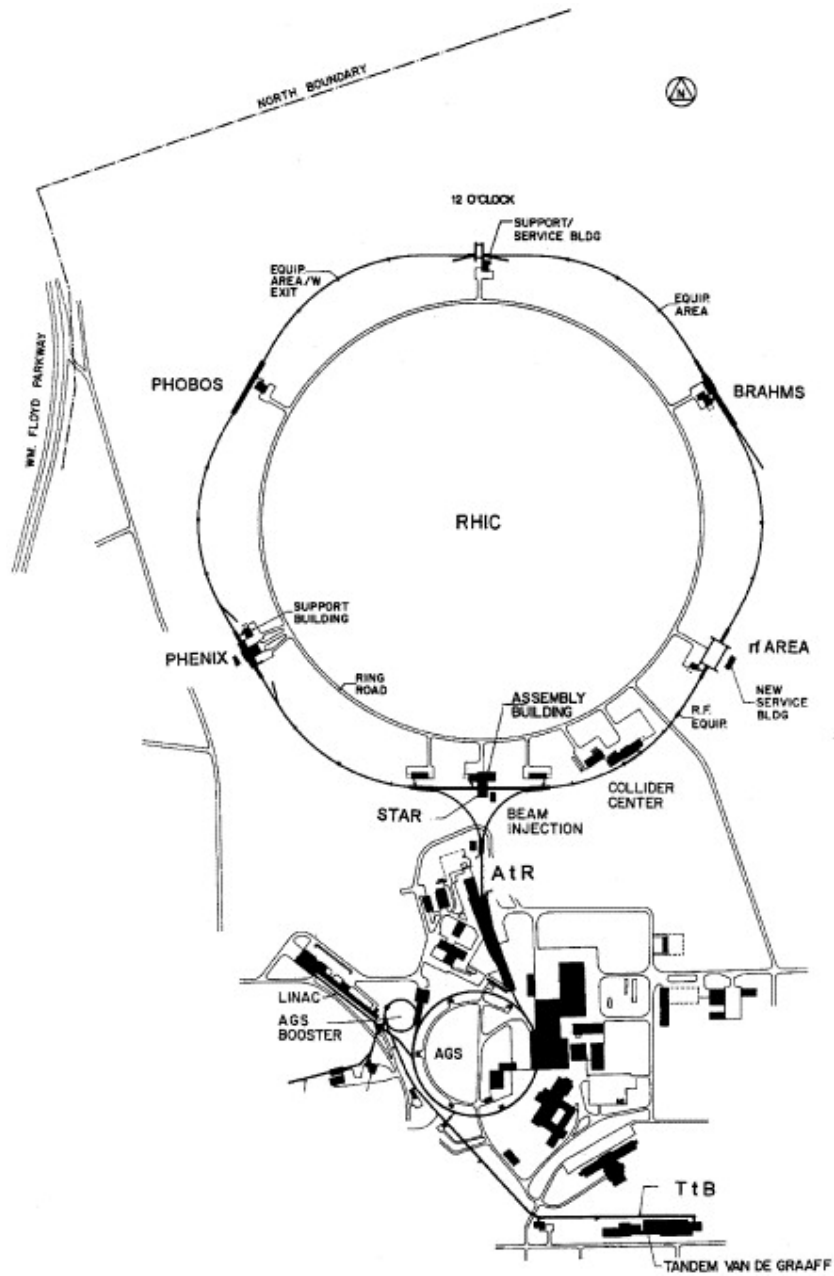
Figure 3.1: The RHIC complex

26
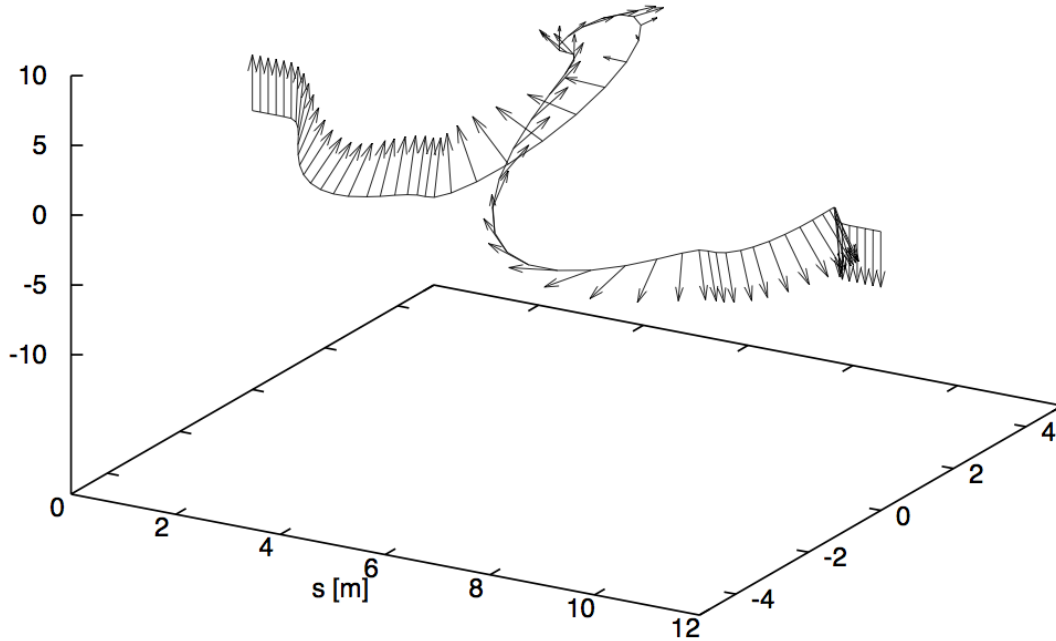
Figure 3.2: 180 degree proton spin flip by Siberian Snake

3.2 The STAR Detector

The Solenoid Tracker at RHIC (STAR) is located at the 6 o'clock position on the RHIC ring. It consists of several sub-detectors working in conjunction to detect, identify, and track particles.

3.2.0.1 Time Projection Chamber

One of they key detectors of STAR is the Time Projection Chamber (TPC). It is tasked with tracking particles, measuring momenta, and detecting ionization energy loss, dE/dx, to aid in particle identification. The TPC is the large cylindrical gas chamber covering ± 1.8 units of pseudorapidity around the interaction point. It's filled with a mixture of 10% methane and 90% argon at a pressure of 2 mbar above atmospheric pressure. As a charged particle passes through the
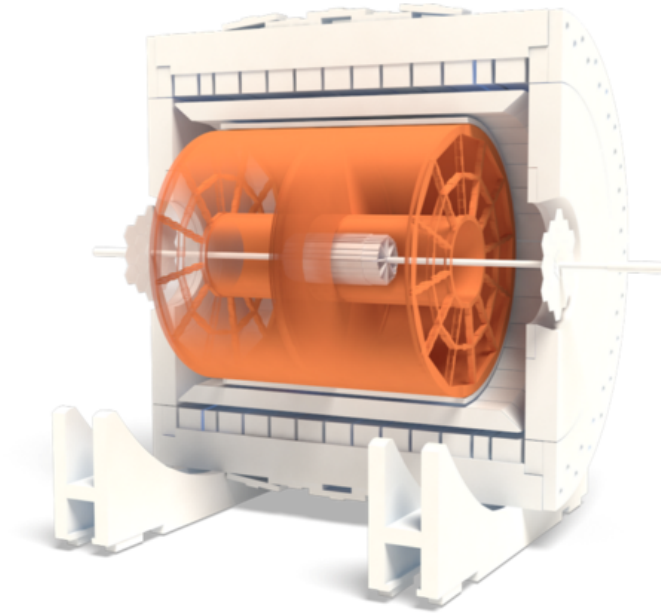
Figure 3.3: STAR Time Projection Chamber

TPC, the gas is ionized, leaving a trail of electrons in it's wake. These electrons drift to the end caps of the TPC under a uniform electric field of about 135 V/cm where they are collected in a proportional chamber to record their drift time and location in the $r - \phi$ plane and along the z direction. This information can be analyzed to reconstruct the track of the ionizing particle. The particle's path will curve due to the presence of STAR's magnetic field an amount proportional to the particles charge and it's velocity, allowing for the measurement of particle momenta, charge, and ionization energy loss.

At the center of the TPC is a central membrane which splits the TPC in two halves. This membrane is kept at 28 kV while the two end caps are at ground. A field cage is located around the TPC to create 182 equipotential slices in the TPC. This set up allows for a very uniform electric field to be kept.

A mixture of 10% methane and 90% argon is chosen for the TPC gas due to its relatively large drift velocity. This drift velocity also peaks at the operating

electric field (135 V/cm) making it relatively unaffected by subtle fluctuations in the electric field.

The TPC gas drift velocity is calibrated with a laser system. Thirty six aluminum stripes are positioned on either side of the central membrane and are illuminated with an ultraviolet laser. This causes photo-ejection of electrons which drift to the end caps where they are read. The position of the aluminum stripes are known with such precision that the time it takes the ejected electrons to reach the end cap readouts, as well as the position they reach, can be used for calibration.

The end cap is equipped with 12 modular sectors arranged covering 180 degrees in azimuth. These sectors are arranged like a clock with only 3 mm separating them. Each sector, shown in figure 3.4, has a grid of readout pads and a wire proportional chamber consisting of three wire grids; a gating grid, a shield (or ground) grid and an anode grid. The gating grid is required to keep boundary conditions with the central membrane and field cage in order to achieve the uniform electric field, and is thus arranged to do so. It prohibits ions generated from avalanches on the anode wire from drifting back into the main TPC region and effecting the drift field. The anode wire plane is made up of 20μ wires aligned radially around the sector. This is to achieve maximum precision of the measurement of momenta from high momentum (straight) tracks. The anode grid is completed by wires in the other direction separated by 4 mm.

As the drifting electrons reach the anode grid an avalanche occurs triggering a temporary image charge to be induced on the read-out pads. The width of each read-out pad is optimized to ensure that at least three read-out pads will share the signal from a single avalanche. This allows for the best centroid reconstruction. The grid of read-out pads is broken up into two sections. The outer portion of the grid has continuously packed read-out pads measuring 6.7 mm by 20 mm optimized for good dE/dx resolution. These pads are located 4 mm behind the anode grid. The inner portion has smaller read-out pads measuring 3.35 mm by
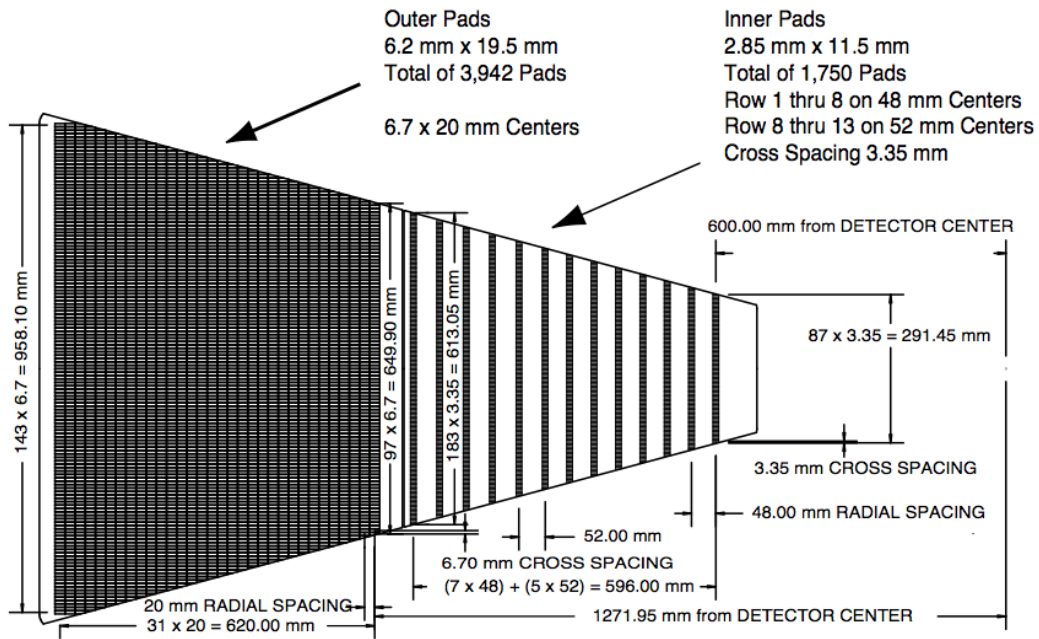
Figure 3.4: One of the 12 anode sectors of the TPC. The outer portion has densely packed pads, while the inner portion is composed of wider rows.

12 mm optimized for good 2-hit detection. This helps with the large track density seen in the inner portion of the TPC. Due to the nature of the small pads, the space for electronics was limited. Unfortunately the electronic boards for read-out were not compact enough in the late 1990's when the TPC was constructed to fit in this available space. Because of this, it was impossible to have continuous radial coverage for the inner section as in the outer section. Instead they are arrange in strips as seen in Fig. 3.4. This arrangement prohibits the inner section to be much help in dE/dx resolution [7].
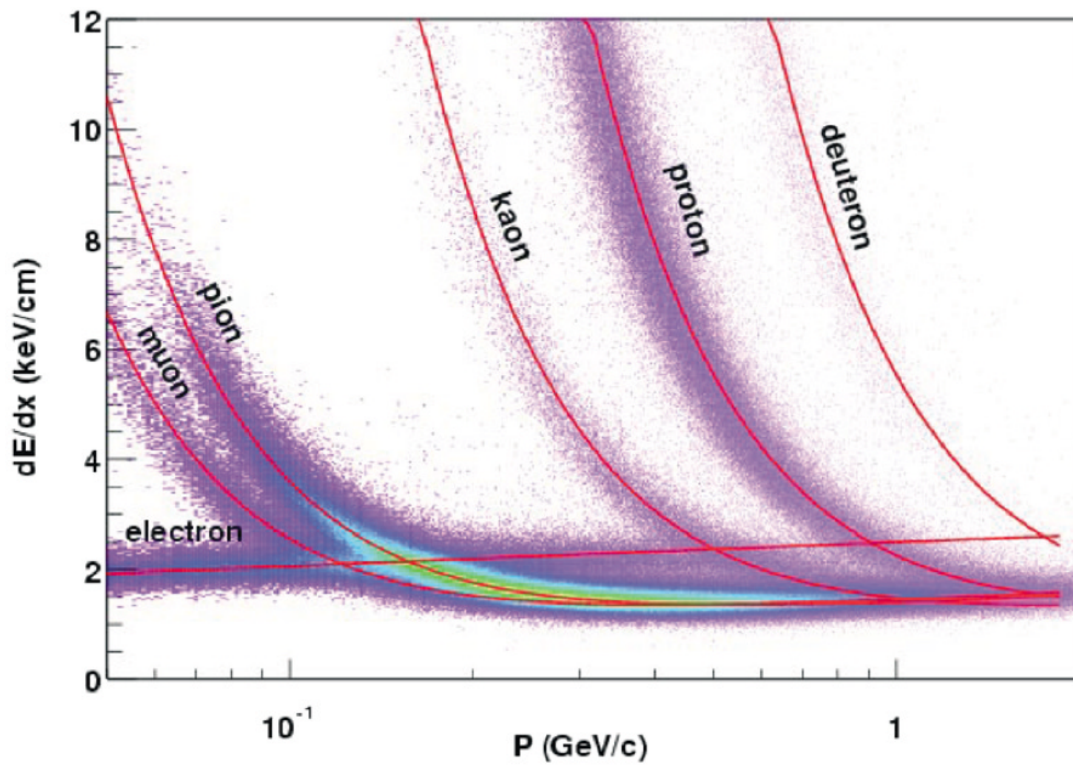
Figure 3.5: Ionization energy loss in TPC gas. Different species show different energy loss signature. This aids in particle identification.

3.2.0.2 Barrel Electromagnetic Calorimeter
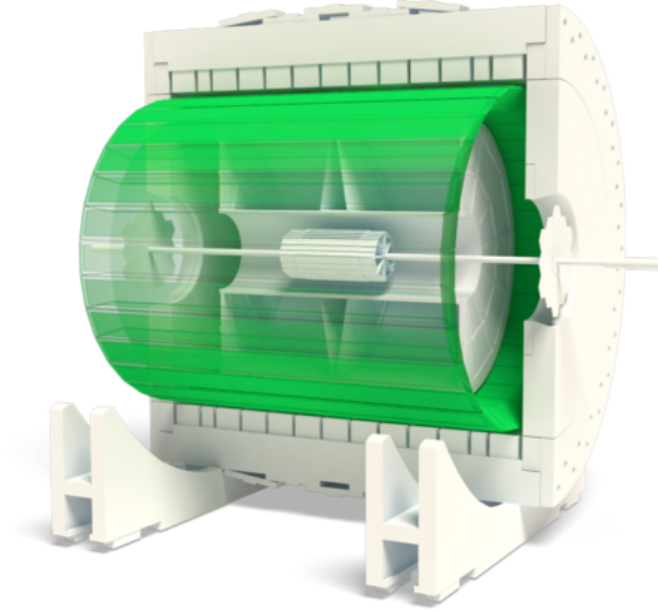
Figure 3.6: Barrel Electromagnetic Calorimeter (BEMC)

The Barrel Electromagnetic Calorimeter (BEMC) is a large array of lead and plastic scintillator sampling calorimeter sitting outside the TPC and inside the STAR magnet. At $\eta = 0$ the BEMC is roughly 20 radiation lengths thick allowing it to contain electromagnetic showers up to 60 GeV. Optical fibers are used to carry scintillation light from the BEMC array to outside the STAR magnet where it is fed into photomultiplier tubes (PMT).

The BEMC is composed of a total of 4800 towers, each one subtending 0.05° in ϕ and 0.05 units in η. A tower consists of 20 layers of 5 mm thick lead, 19 layers of 5 mm thick scintillator, and two layers of 6 mm thick scintillator. The tower geometry is projective toward the nominal interaction point, as seen in Fig. 3.8.

The BEMC is equipped with a pre-shower detector which provide readings of the longitudinal shower development after 1 to 1.5 radiation lengths. Made up of the first two (6 mm) scintillating layers of the tower, the pre-shower detector

aids in distinguishing between π^0 and γ as well as between electrons and hadrons. Electrons will typically have a larger energy loss inside the BEMC than hadrons resulting in roughly 63% of electrons showering before the pre-shower volume and 84% by the middle of the pre-shower detector compared to only 3% and 6% for hadrons. The pre-shower detector consists of two 6 mm thick layers of scintillator instead of the 5 mm thick scintillator layers in the rest of the BEMC.

The active scintillating layers, both pre-shower and regular, are made of Kuraray SCSN81 and light from each layer is carried out with wavelength-shifting fiber embedding into the scintillator layer. The scintillation light from each layer is transferred to a 2.1 m long optical fiber which carries it through gaps in the magnet steel to boxes containing an array of photomultipliers which are mounted outside the magnet. Here the light from all 21 layers in a tower, including the two pre-shower layers, are combined and fed into a single PMT. The pre-shower detector also passes a second sample of scintillation light from layers 1 and 2 to a separate PMT, this time not combined with light from any other layers.

Some neutral particles, such as π^0, ρ, *etc.* do not ionize the TPC gas, but may decay to daughter particles which interact electromagnetically. The BEMC is tasked with providing spatial resolution of such species. Instead of making the size of each tower of the BEMC comparable to the Moliere radius in the lead-plastic scintillator, a shower maximum detector (SMD) is added into the BEMC for spatial resolution. The SMD, set at about 5.6 radiation lengths at $\eta = 0$, is composed of an aluminum plate with channels on either side. As seen in Fig. 3.9, a 50μm gold-plated tungsten anode wire lies in each channel. The wires run along the barrel. As $e + e^-$ pairs generated in the electromagnetic shower enter the gas volume, a large ionization signal is generated. Detection strips are located on the top and bottom faces of the aluminum plate. One set of strips runs parallel to the wires and provides the spatial distribution of the shower in the η direction. The other set, running perpendicular to the wires provides the spatial distribution in
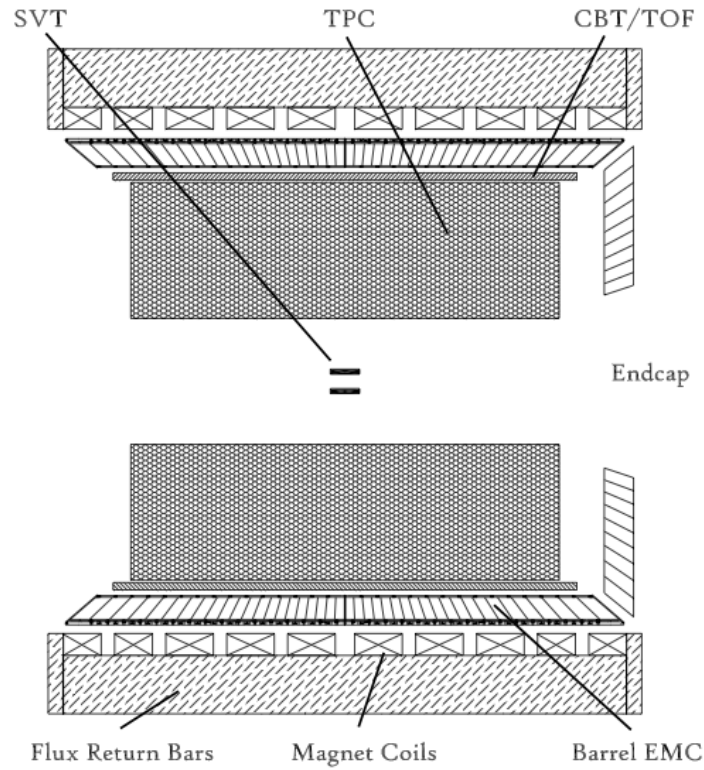
Figure 3.7: The BEMC is located outside the TPC but inside the STAR magnet and magnet flux return bars. The scintillation light is transported through gaps in the flux return bars where it is read out by PMTs.
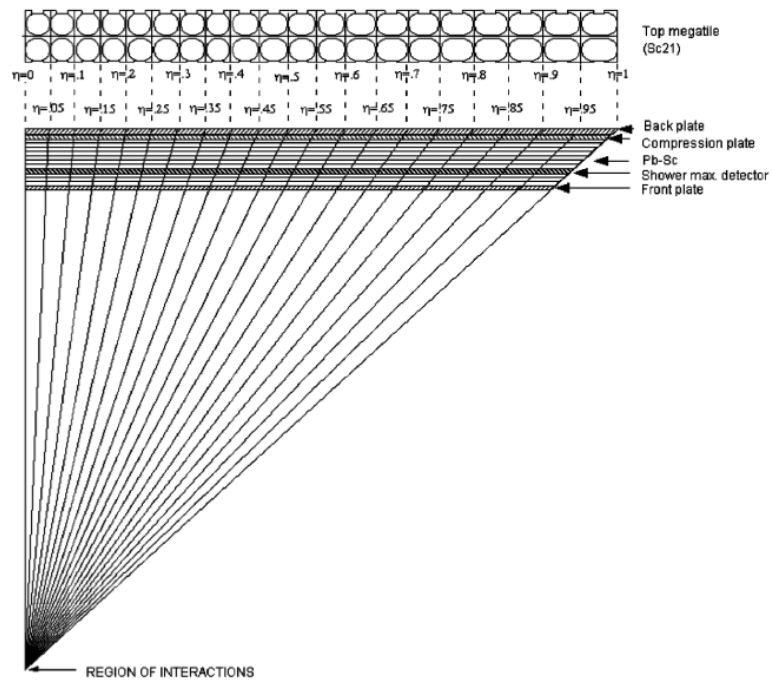
Figure 3.8: Each geometrical shape of each tower of the BEMC is projective, back to the nominal interaction region of STAR. The shower max detector as well as the individual scintillator/lead layers are shown.

Back Strip PCB 150 strips are parallel to the anode wires

Aluminum extrusion   30 cells on each side   Epoxy   60 anode wires   Cathode strips

Front Strip PCB   150 strips are perpendicular to the anode wires
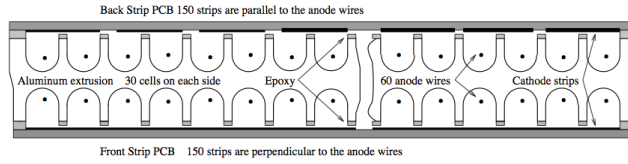
Figure 3.9: Cross sectional view of the shower max detector. Aluminum extrusion in the center containing two sets of anode wires. Cathode strips on the top and bottom face run either parallel or perpendicular to the anode wires.

Electromagnetic
Shower

5X0 EMC

Back plane   Front plane
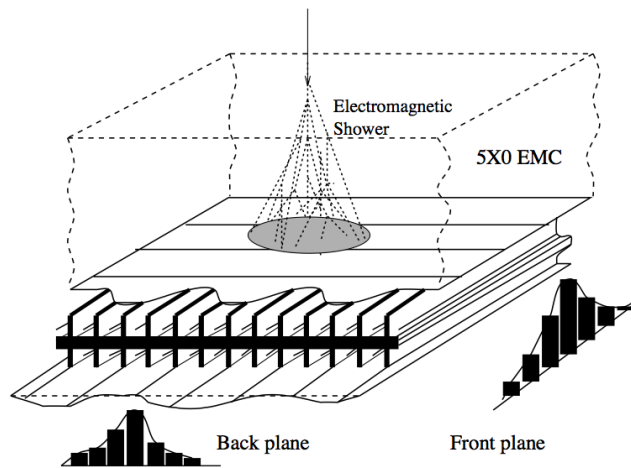
Figure 3.10: Schematic of spatial reconstruction in SMD. The cathode strips on the top and bottom faces read the induced charged in the ϕ and η directions separately.

the ϕ direction. A schematic of this is shown in Fig. 3.10. Together they give a full description of the shower position [14].

3.2.0.3   Time of Flight

STAR has a time-of-flight system for particle identification. The system is composed of two different detectors, the Time of Flight Patch Detector (TOF) and the Vertex Position Detector (VPD). Together these detectors allow for direct 2σ $\pi/K/p$ identification for track momenta up to about 1.7 GeV/c.
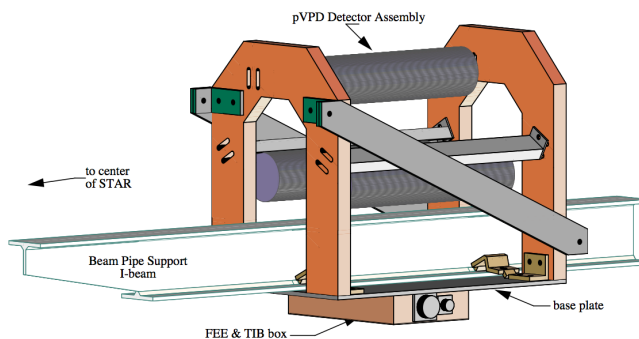
Figure 3.11: The VPD detector is mounted in the assembly.

The VPD is responsible for starting the clock of the time-of-flight system. It consists of two segmented plastic scintillator detectors, one on either side of the STAR interaction region, at a distance of 5.6 m from the center of the STAR detector. Both are positioned very close to the beam pipe and detect very forward, high energy photons produced in the collision. The average of the start time for both detectors to see this photon pulse is declared the "start time" for the event. The scintillation light is read out by PMTs.

The VPD starts the clock for the event and the TOF stops it. The TOF uses the multi-gap resistive plate chamber (MRPC) technology developed by the ALICE group. The MRPC, shown in Fig. 3.12, is a stack of resistive plates with uniform gas gaps in between. Applying a high voltage to electrodes on the outer plates creates a strong electric field in each gap. An avalanche is generated in the gaps when a charged particle passes through. Copper pickup pads located outside the electrodes are used to read out the signal [19].

The TOF consists of 120 "trays". Each tray, shown in Fig. reffg:starToF, consists of 32 MRPC modules. The trays are arranged at the outer radius of the TPC, 60 on the east side and 60 on the west. In total they cover two units in pseudorapidity ($-1 < \eta < 1$), and give full azimuthal coverage. The total time resolution of the TOF system is 87 ps [19].
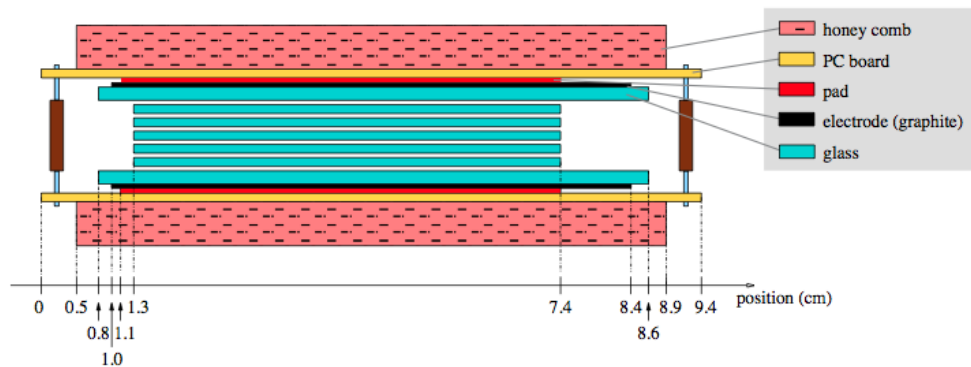
Figure 3.12: multi-gap resistive plate chamber (MRPC) used in the TOF detector [19]
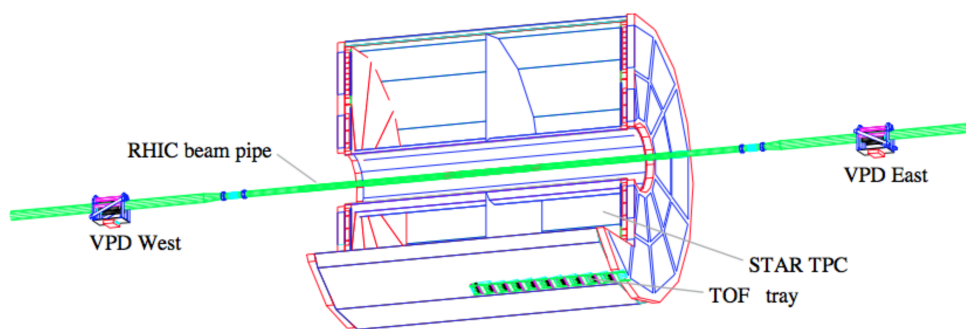
Figure 3.13: One tray of the Time-of-Flight Detector is shown at the 7 o'cock position of STAR. Also shown here are the two VPD detectors on either side of the STAR detector.

Once the clock is stopped a value of β for the track can be calculated as in Eqn. 3.1.

$$\frac{1}{\beta} = \frac{c\tau}{s} \tag{3.1}$$

Here c is the speed of light, τ is the time measured by the time-of-flight system, and s is the path length of the track using the reconstructed path of the TPC. From here the mass of the particle can be found using the momentum of the track measured in the TPC.

$$M^2 = \frac{p^2}{\beta^2} - p^2 \tag{3.2}$$
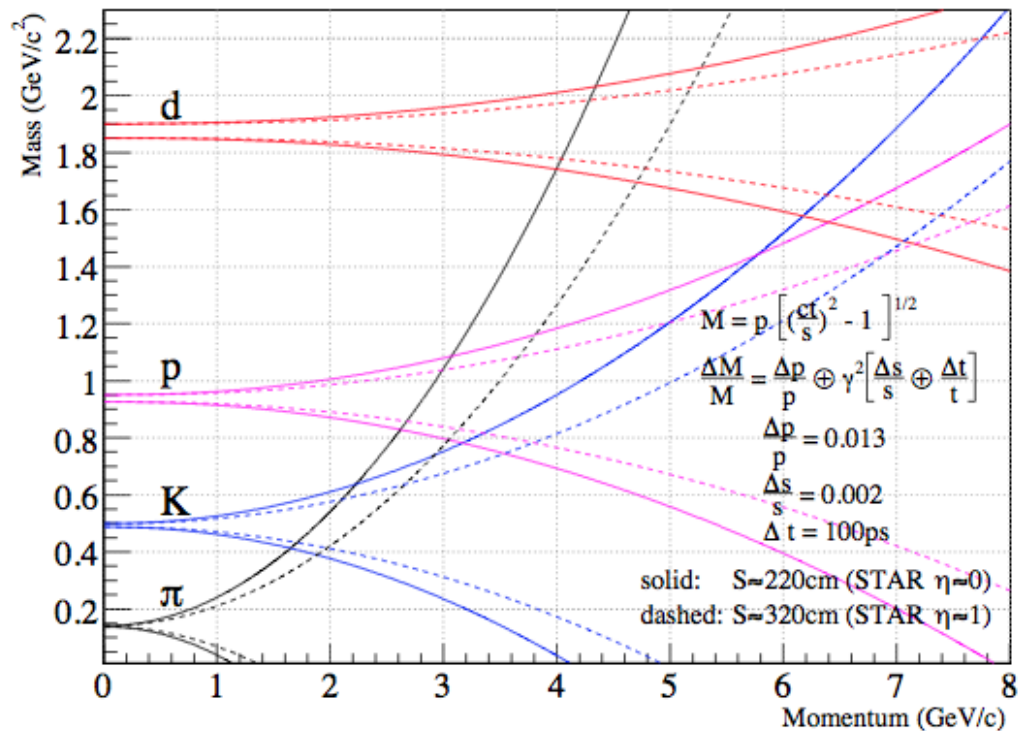
Figure 3.14: Particle mass resolution of the STAR TOF system. Solid lines correspond to tracks near $\eta = 0$, dashed lines correspond to tracks near $\eta = 1$. Particles can be identified with greater than 2σ confidence in areas where lines do not overlap [19].

CHAPTER 4

Theoretical Background for Analysis

One of the most theoretically clean ways to access the transversity distribution function is through the observation of a single spin asymmetry(SSA) in a semi-inclusive deep inelastic scattering(SIDIS) process between transversely polarized and unpolarized protons where a hadron pair is detected [6]. This thesis will be focused mainly on the case where the hadron pair is $\pi^+\pi^-$. At leading twist, only one source for a SSA exists [6].

The process we are interested in is $p_a p_b^\uparrow \to \pi^+\pi^- + X$, where unpolarized proton a collides with transversely polarized proton b with spin $\boldsymbol{s}_b$. Outgoing pions with momentum $p_{h,1}$ for the positively charged pion and $p_{h,2}$ for the negatively charged pion are detected. The total pair momentum $\boldsymbol{P}_h$ is the sum of $p_{h,1}$ and $p_{h,2}$, the transverse component of which is written as $P_T^{\pi^+\pi^-}$. The difference of the pion momenta is defined as $\boldsymbol{R} = (p_{h,1} - p_{h,2})/2$.

The difference between cross sections when proton b is polarized up and down can be written in a factorized form which includes the transversity distribution h_1, and the IFF, $H_1^{\sphericalangle}$.

$$\mathrm{d}\sigma^\uparrow - \mathrm{d}\sigma^\downarrow = \mathrm{d}\sigma_{UT} = 2P_T^{\pi^+\pi^-} \sum_{a,b,c,d} |\boldsymbol{s}_b| \frac{|\boldsymbol{R}|}{M_{inv}^{\pi^+\pi^-}} \sin(\phi_{RS}) \int \frac{dx_a dx_b}{8\pi^2 z_c} f_1(x_a) h_1(x_b) \frac{d\Delta\hat{\sigma}_{ab^\uparrow \to c^\uparrow d}}{d\hat{t}}$$

$$\times \sin\theta H_1^{\sphericalangle c}\left(\bar{z}_c, \cos\theta, M_{inv}^{\pi^+\pi^- 2}\right)$$

(4.1)

Where θ is the angle between $p_{h,1}$ in the center of mass frame of the pair and $\boldsymbol{P}_h$ in the lab frame. In the above expression, $\phi_{RS} = \phi_S - \phi_R$, where ϕ_S is the angle

between the spin vector of proton b and the scattering plane and ϕ_R is the angle between the scattering plane and the two hadron plane. These angles are shown in Fig. 4.1 and defined as [6]

$$\cos\phi_S = \frac{(\hat{\boldsymbol{P}}_b \times \boldsymbol{P}_h)}{|\hat{\boldsymbol{P}}_b \times \boldsymbol{P}_h|} \cdot \frac{(\hat{\boldsymbol{P}}_b \times \boldsymbol{S}_b)}{|\hat{\boldsymbol{P}}_b \times \boldsymbol{S}_b|} \qquad \sin\phi_S = \frac{(\boldsymbol{P}_h \times \boldsymbol{S}_b) \cdot \hat{\boldsymbol{P}}_b}{|\hat{\boldsymbol{P}}_b \times \boldsymbol{P}_h||\hat{\boldsymbol{P}}_b \times \boldsymbol{S}_b|}$$

$$\cos\phi_R = \frac{(\hat{\boldsymbol{P}}_h \times \boldsymbol{P}_a)}{|\hat{\boldsymbol{P}}_h \times \boldsymbol{P}_a|} \cdot \frac{(\hat{\boldsymbol{P}}_h \times \boldsymbol{R})}{|\hat{\boldsymbol{P}}_h \times \boldsymbol{R}|} \qquad \sin\phi_R = \frac{(\boldsymbol{P}_a \times \boldsymbol{R}) \cdot \hat{\boldsymbol{P}}_h}{|\hat{\boldsymbol{P}}_h \times \boldsymbol{P}_a||\hat{\boldsymbol{P}}_h \times \boldsymbol{R}|} \qquad (4.2)$$

where $\boldsymbol{P}_a$ and $\boldsymbol{P}_b$ are the momenta of protons a and b respectively.

Also appearing in Eqn. 4.1 is the calculable hard scattering cross section of parton a scattering off of transversly polarized parton b into transversely polarized parton c and parton d. Parton c then goes on to fragment into a $\pi^+\pi^-$ pair keeping a fraction z_c of parton c's momentum as described by $H_1^{\sphericalangle}$.

Comparing this to the cross section when both initial state quarks are unpolarized we see several similarities.

$$d\sigma_{UU} = 2P_T^{\pi^+\pi^-} \sum_{a,b,c,d} \int \frac{dx_a dx_b}{8\pi^2 z_c} f_1^a(x_a) f_1^b(x_b) \frac{d\hat{\sigma}_{ab\to cd}}{d\hat{t}} D_1^c(\bar{z}_c, \cos\theta_C, M_C^2) \qquad (4.3)$$

As similar as Eqns. 4.1 and 4.3 look, there are some important differences worth noting. Obviously the polarization isn't there since we now are dealing with unpolarized scattering. The sinusoidal modulation has also disappeared. The transversity distribution has turned into a second unpolarized distribution, and the IFF has turned into D_1^c which is the unpolarized counterpart to the IFF.

The most important thing to mention is that the sine modulation seen in unpolarized-transversely polarized (U-T) scattering is not seen in unpolarized-unpolarized (U-U) scattering. This means that there is a bias to the yield of $\pi^+\pi^-$ pairs in U-T scattering when compared to U-U scattering. We can observe this by looking at the number of $\pi^+\pi^-$ pairs at a given value of ϕ_{RS} when the polarization of the proton beam is $\hat{y}$ vs the number when the polarization is $-\hat{y}$. We then normalize by the number we see at that value of ϕ_{RS} for U-U scattering,

which gives the Single Spin Asymmetry (SSA) A_{UT}.

$$A_{UT} \sin(\phi_{RS}) = \frac{1}{|\boldsymbol{s}_b|} \frac{d\sigma^\uparrow - d\sigma^\downarrow}{d\sigma_{UU}} \quad (4.4)$$

In our experiment we never scatter unpolarized protons, so we have to be clever about the cross section seen in the denominator of Eqn. 4.4. If we sum over the two spin states we are left with the entire unpolarized cross section $d\sigma^\uparrow + d\sigma^\downarrow = d\sigma_{UU}$. Using this, Eqn. 4.4 can be rewritten as [6, 11, 29]

$$A_{UT} \sin(\phi_{RS}) = \frac{1}{|\boldsymbol{s}_b|} \frac{d\sigma^\uparrow - d\sigma^\downarrow}{d\sigma^\uparrow + d\sigma^\downarrow}. \quad (4.5)$$

This is the only source of a single spin asymmetry at leading twist [6]. It is important to keep this single spin asymmetry differential in as many kinematic variables as possible, otherwise it is likely to average to zero [27]. In this analysis the asymmetry will be kept differential in $M_{inv}^{\pi^+\pi^-}$, $P_T^{\pi^+\pi^-}$, and $\eta^{\pi^+\pi^-}$ individually. $\eta^{\pi^+\pi^-}$ acts as a surrogate for momentum fraction x, as partons with higher x will fragment into hadrons at larger η. The asymmetry will also be kept differential in two of the three variables simultaneously (*i.e.*, $M_{inv}^{\pi^+\pi^-}/P_T^{\pi^+\pi^-}$, $M_{inv}^{\pi^+\pi^-}/\eta^{\pi^+\pi^-}$, and $P_T^{\pi^+\pi^-}/\eta^{\pi^+\pi^-}$).

Important physics can be seen by performing a partial-wave expansion of the cross section [12]. Expanding $\sin\theta H_1^\sphericalangle$ and looking at the first two terms,

$$\sin\theta H_1^{\sphericalangle c}(\bar{z}_c, \cos\theta, M_{inv}^{\pi^+\pi^-2}) \approx H_{1,ot}^{\sphericalangle c}(\bar{z}_c, M_{inv}^{\pi^+\pi^-2}) \sin\theta$$
$$+ H_{1,lt}^{\sphericalangle c}(\bar{z}_c, M_{inv}^{\pi^+\pi^-2}) \sin\theta \cos\theta \quad (4.6)$$

The first term, S/P wave interference, is due to the interference between amplitudes for a decay into an $L = 0$ $\pi^+\pi^-$ pair and an $L = 1$ transversely polarized $\pi^+\pi^-$ pair. The second term, P/P wave interference, is due to the interference between amplitudes for a decay into an $L = 1$ $\pi^+\pi^-$ pair and an $L = 1$ transversely polarized $\pi^+\pi^-$ pair. The $L = 1$ contributions comes from a $\pi^+\pi^-$ pair that went
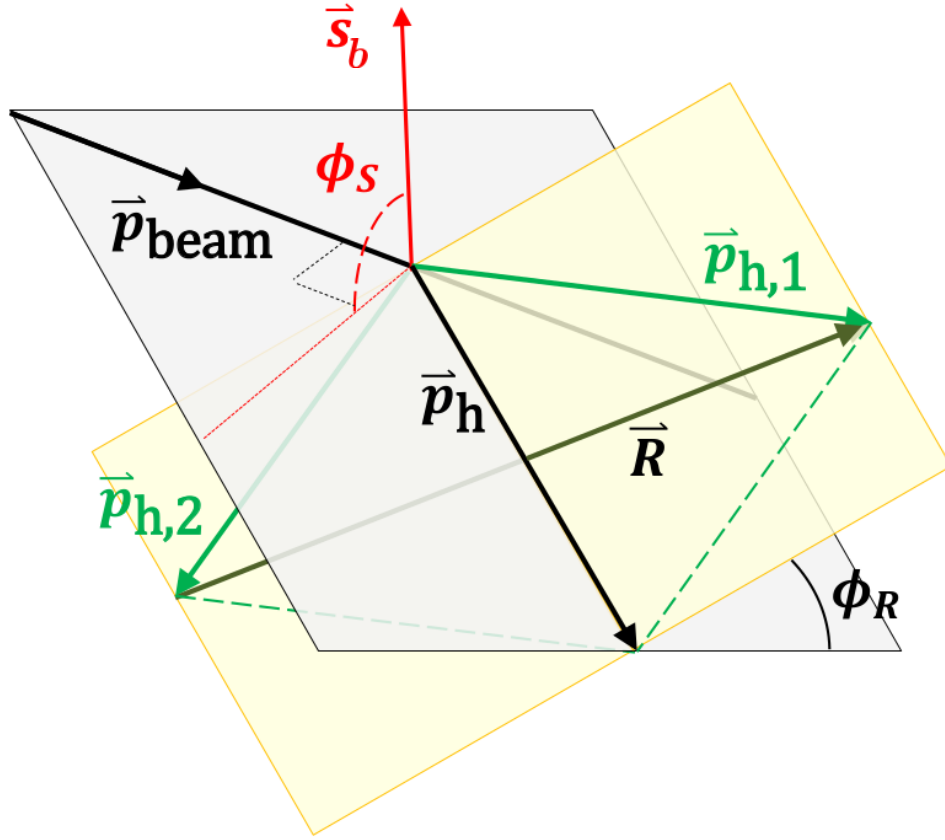
Figure 4.1: Visual representation of angles ϕ_R and ϕ_S. $\phi_{RS} = \phi_R - \phi_S$

$\vec{p}_{h,1}$ is the momentum of the positive hadron while $\vec{p}_{h,2}$ is the momentum of the negative hadron.

through a spin-1 intermediate state. One such intermediary we have the ability and statistics to look for is the ρ meson. We expect there to be an enhancement in the IFF, and thus the asymmetry, in the invariant mass region of the ρ (770 MeV) [6, 41].

CHAPTER 5

2006 Analysis and Simulation

The 2006 data set gave us the first glimpse of this asymmetry in $p+p$ collisions. The analysis of the 2006 data set was done mostly by Dr. Anselm Vossen from Indiana University with an integrated luminosity of $1.8\,\mathrm{pb}^{-1}$ of 200 GeV transverse proton proton collisions. The average beam polarization was 60% [2].

Figure 5.1 shows the asymmetry as a function of the pion pair invariant mass. As hinted from the theory there is an increase in the asymmetry around the ρ meson mass for both forward ($\eta > 0$) and backward pairs ($\eta < 0$).

Varying the opening angle of the pion pair addresses the z dependence of the asymmetry. The fraction of the fragmenting quark momentum the pion pair retains, z, influences the size of the IFF. It turns out the asymmetry increases as the opening angle decreases as seen in Fig. 5.2.

As stated previously, $\eta^{\pi^+\pi^-}$ acts as a surrogate for the momentum fraction of the polarized parton, as a larger partonic momentum fraction will cause the pion pair to be produced in a more forward direction. The asymmetry is plotted as a function of $\eta^{\pi^+\pi^-}$ in Fig. 5.3. As one might expect, the asymmetry is larger the more forward the pion pair is. This is explained by the fact that pairs from more forward pseudorapidity result from polarized partons with larger momentum fractions, allowing for a larger spin transfer.

A supplemental analysis was done on simulated data to investigate partonic momentum fractions as well as biases introduced by STAR triggers. Figure 5.4 shows the momentum fraction of the fragmenting quark for pairs in the forward

45
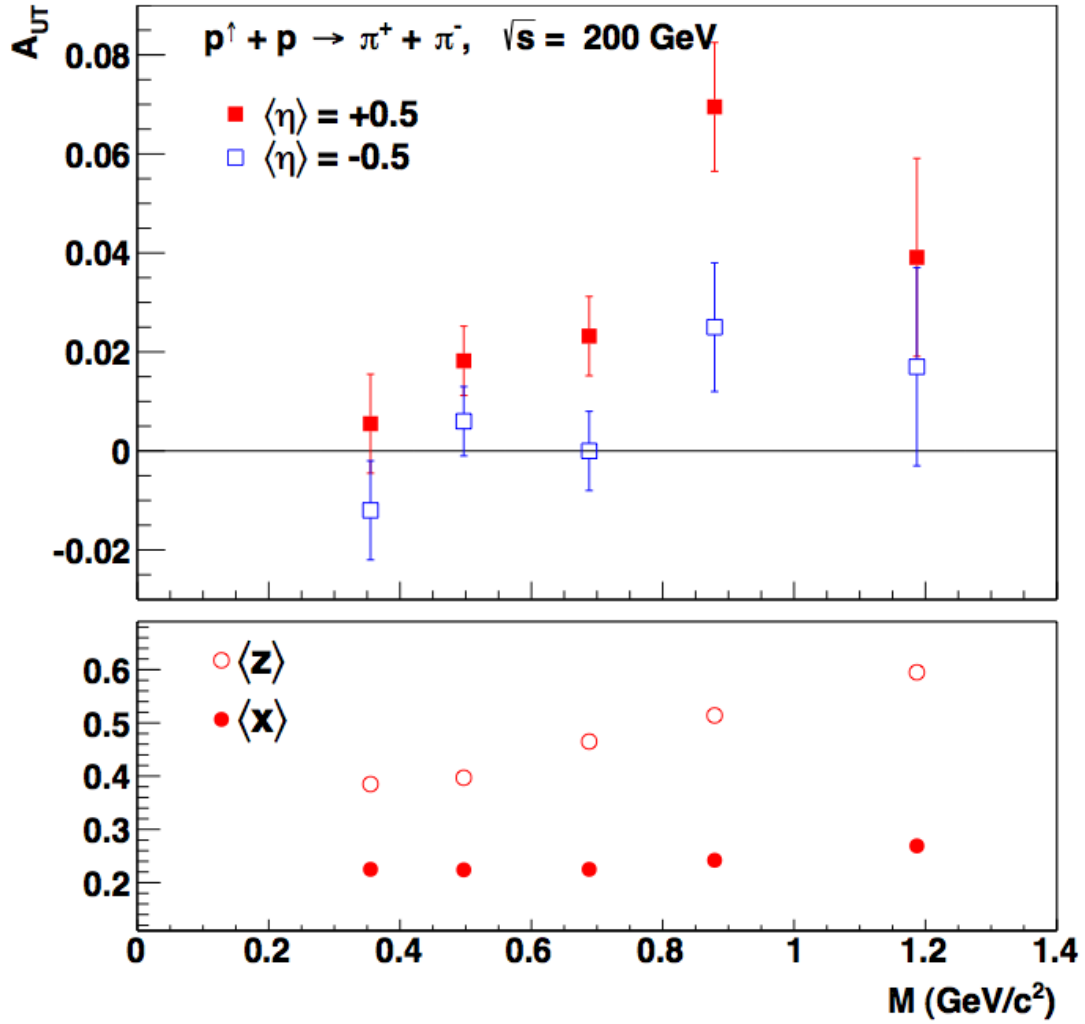
Figure 5.1: Asymmetry versus invariant mass of the $\pi^+\pi^-$ pair for the 2006 data set for pairs scattering in the forward direction (red) and in the backward direction (blue).
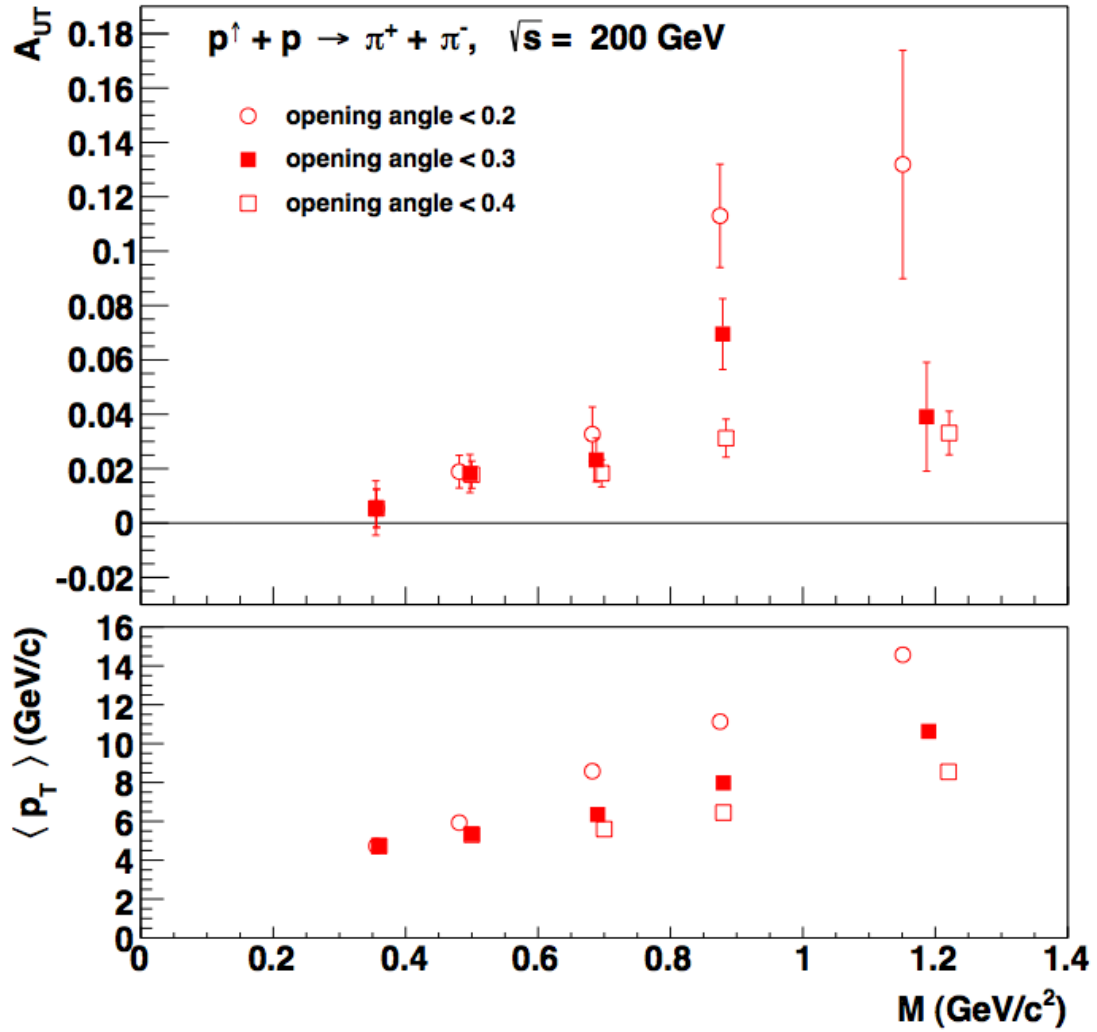
Figure 5.2: Asymmetry versus invariant mass of the $\pi^+\pi^-$ pair for the 2006 data set for different opening angles of pairs are scattered into the forward direction.

47
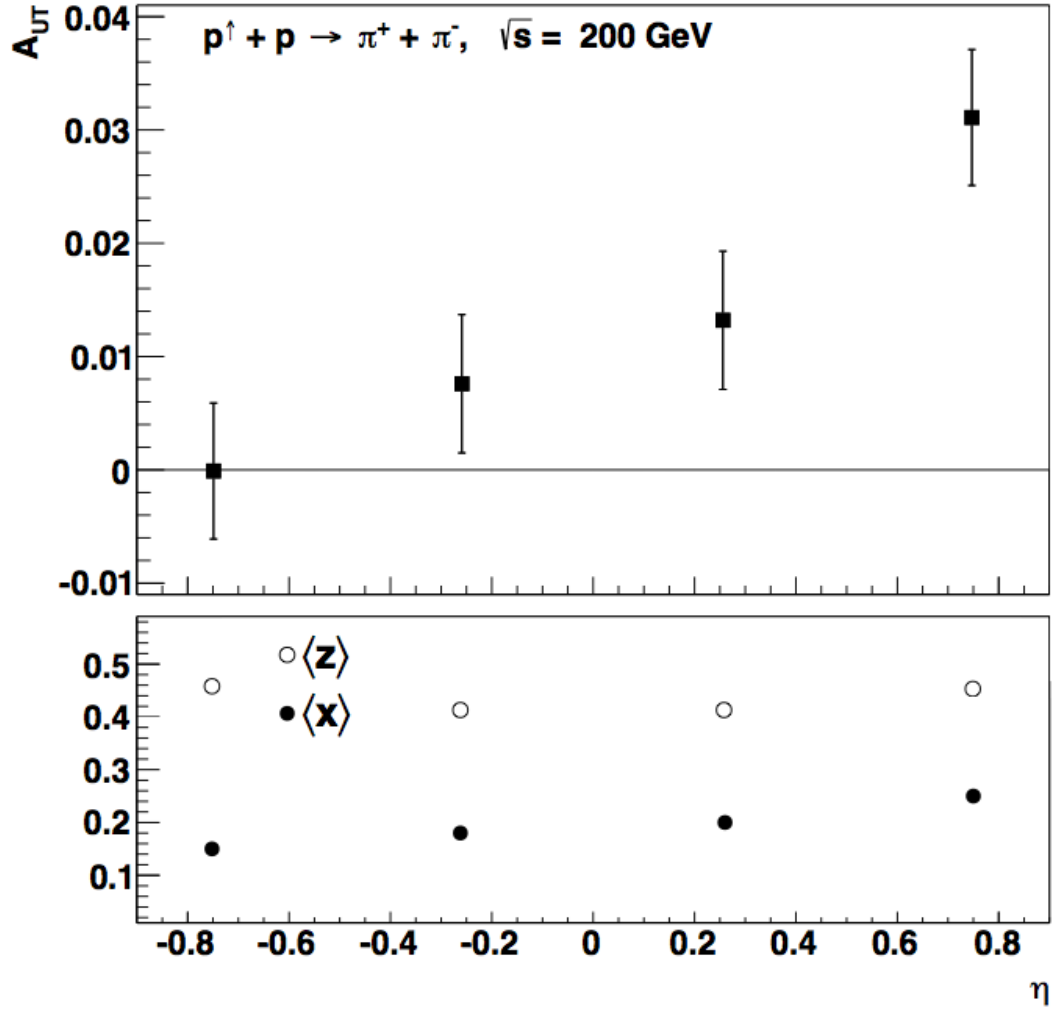
Figure 5.3: Asymmetry versus $\eta^{\pi^+\pi^-}$ for the 2006 data set

and reverse directions. This bias toward higher x events is shown in Fig. 5.5. A more in-depth discussion about the need for an analysis on simulated data as well as the results of the analysis on the 2012 simulation is given in appendix B.

These results are the first sign of non-zero asymmetries in $\pi^+\pi^-$ pair correlation in polarized proton collisions. More can be read about the 2006 study in reference [2].
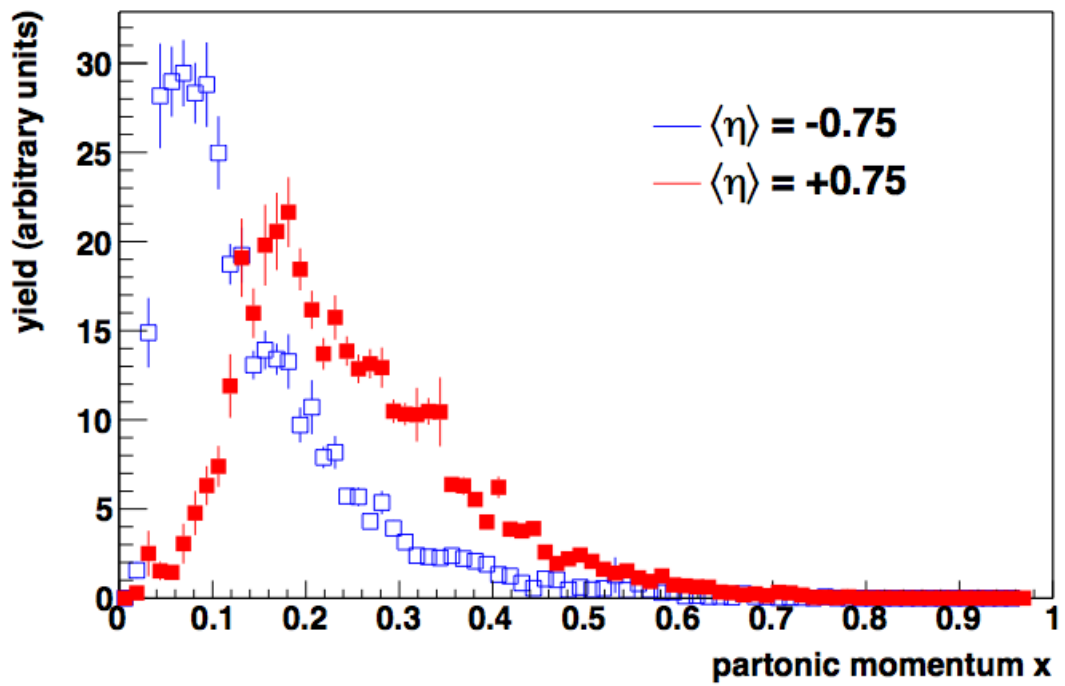
Figure 5.4: Partonic momentum fraction x obtained from simulation for the parton from the polarized proton in the forward (red) and backward (blue) direction
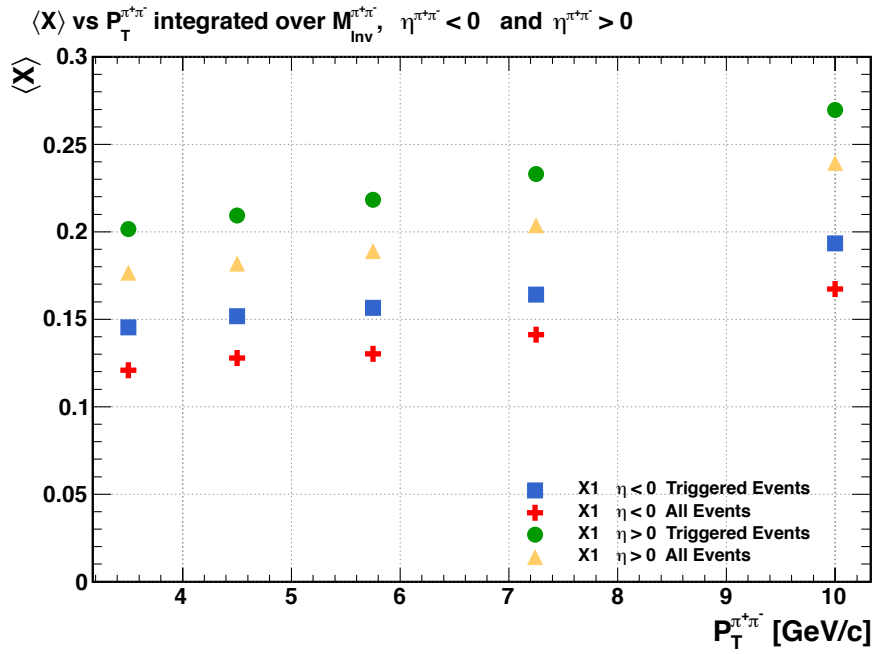
Figure 5.5: The averge momentum fraction x of the polarized quark (quark 1) is larger for triggered events than for all events. This effefct is seen in both the forward and backward directions and for all $\pi^+\pi^-$ transverse momenta. Note: this figure is caclulated for the 2006 detector configuration and triggers.

CHAPTER 6

2012 IFF Analysis

6.1 Data Set, Triggers, and Cuts

The total integrated luminosity for the 2012 200GeV transverse proton data set was 7.74 pb^{-1} [18]. The runs from the 2012 production that passed quality tests and are eligible to be used in the analysis are listed in the table below. The average beam polarization from pairs found in these runs is 61.618 $\pm$.003%.

|							
13044126	13045001	13045003	13045005	13045006	13045007	13045012	13045029
13045056	13045133	13045134	13045135	13045138	13045145	13045146	13045164
13046001	13046002	13046003	13046004	13046011	13046012	13046013	13046014
13046015	13046017	13046121	13047003	13047004	13047022	13047023	13047024
13047026	13047027	13047028	13047029	13047030	13047031	13047032	13047033
13047034	13047035	13048010	13048011	13048012	13048013	13048014	13048015
13048016	13048017	13048018	13048019	13048030	13048031	13048032	13048040
13048041	13048042	13048043	13048044	13048045	13048046	13048049	13048050
13048051	13048052	13048053	13048087	13048088	13048089	13048090	13048091
13048092	13048093	13049031	13049032	13049035	13049039	13049041	13049042
13049044	13049045	13049046	13049047	13049048	13049049	13049050	13049072
13049073	13049080	13049081	13049082	13049089	13049093	13049094	13049096
13049098	13049099	13049101	13050001	13050007	13050009	13050011	13050012
13050015	13050016	13050020	13050022	13050023	13050028	13050029	13050031
13050032	13050033	13050036	13050037	13050038	13050039	13050041	13050043
13050044	13050046	13050047	13050049	13050050	13051011	13051012	13051015
13051016	13051017	13051019	13051020	13051021	13051022	13051023	13051024
13051026	13051028	13051074	13051080	13051081	13051083	13051085	13051086
13051087	13051088	13051092	13051093	13051095	13052001	13052002	13052003
13052004	13052005	13052009	13052010	13052011	13052012	13052013	13052014
13052015	13052016	13052017	13052018	13052020	13052021	13052022	13052037
13052039	13052042	13052043	13052045	13052048	13052050	13052051	13052052
13052053	13052054	13052056	13052088	13053004	13053005	13053006	13053007
13053012	13053013	13053015	13053027	13053028	13054022	13054023	13054044
13054045	13054060	13054061	13054062	13054063	13054064	13054065	13054066
13054068	13054069	13054084	13054085	13055004	13055006	13055007	13055008
13055009	13055010	13055011	13055014	13055016	13055017	13055018	13055019
13055020	13055021	13055022	13055023	13055024	13055035	13055036	13055037
13055038	13055039	13055068	13055070	13055072	13055075	13055076	13055080
13055081	13055082	13055086	13055087	13056005	13056007	13056008	13056020
13056021	13056022	13056023	13056024	13056025	13056026	13056027	13056028
13056029	13056030	13056031	13056033	13056034	13056035	13056037	13056038

13056039	13057011	13057014	13057015	13057016	13057017	13057018	13057019
13057021	13057022	13057023	13057024	13057025	13057026	13057027	13057044
13057045	13057046	13057047	13057048	13057049	13057050	13057051	13057052
13057053	13057055	13057056	13057057	13057058	13058002	13058015	13058016
13058017	13058018	13058025	13058026	13058028	13058029	13058030	13058031
13059084	13060010	13061024	13061025	13061026	13061030	13061031	13061035
13061054	13061055	13061059	13061060	13061061	13062001	13062002	13062004
13062005	13062006	13062007	13062013	13062025	13062026	13062028	13062029
13062049	13062050	13062052	13062059	13062060	13062061	13062062	13062063
13063009	13063010	13063011	13063020	13063022	13063023	13063030	13063031
13063032	13063033	13063034	13063035	13063036	13063053	13063054	13063062
13063063	13063065	13063067	13063068	13063071	13063072	13063073	13063074
13063076	13064001	13064002	13064003	13064004	13064005	13064006	13064012
13064014	13064020	13064021	13064022	13064023	13064024	13064025	13064026
13064028	13064029	13064030	13064031	13064032	13064052	13064055	13064056
13064057	13064059	13064061	13064064	13064065	13064066	13064068	13064070
13064074	13064075	13065005	13065006	13065007	13065008	13065009	13065013
13065014	13065015	13065016	13065017	13065018	13065019	13065020	13065021
13065022	13065047	13065048	13065049	13065050	13065052	13065053	13065055
13065056	13065058	13065059	13065060	13066021	13066022	13066023	13066024
13066025	13066026	13066027	13066028	13066029	13066030	13066031	13066033
13066034	13066035	13066036	13068084	13068088	13068090	13069001	13069002
13069003	13069004	13069005	13069006	13069007	13069014	13069016	13069017
13069018	13069020	13069021	13069022	13069023	13069024	13069026	13069027
13069029	13069030	13069031	13069035	13069036	13069066	13069067	13069068
13069069	13069073	13070006	13070008	13070010	13070011	13070012	13070014
13070015	13070016	13070017	13070018	13070019	13070020	13070021	13070022
13070024	13070025	13070026	13070027	13071009	13071010	13071011	13071012
13072006	13072014	13072015	13072016	13072017	13072018	13072019	13072020

From these runs, events were selected which triggered at least one of the following STAR triggers of interest: JP0, JP1, JP2, AJP, BHT0VPD, BHT1VPD, BHT2BBC, or BHT2. These were chosen because they were most similar to the triggers used to select events in the 2006 analysis, thus allowing for a proper comparison of the results. The thresholds for these triggers can be found in table 6.2.

Tracks from these triggered events were then scrutinized. As the BEMC only covers a finite range in η, tracks at pseudorapidity greater than 2 and less than -2 were rejected. To ensure good track resolution in the TPC necessary for particle identification, tracks with less than five fit points were also rejected. Since different trajectories in the TPC offer a different number of possible fit points, tracks are also required to have at least half of the possible fit points. The position of the vertex the track originated is required to be less than 60 cm from the center of the

Trigger	Threshold
BEMC-JP0	20
BEMC-JP1	28
BEMC-JP2	36
BEMC-HT0	11
BEMC-HT1	15
BEMC-HT2	18
VPD-TACdiff-MAX	4083
VPD-TACdiff-MIN	3883
VPD-East-ADC-SUM	10
VPD-West-ADC-SUM	10
BBC-Small-TACdiff-MAX	4933
BBC-Small-TACdiff-MIN	3267
BBC-Small-East-ADC-SUM	20
BBC-Small-West-ADC-SUM	20

Table 6.2: Relevant Trigger Thresholds

STAR detector. This helps the detector reconstruct the correct kinematic location of the particle. The track is also required to have a transverse momentum larger than 1.5 GeV/c. If a track possesses all the required attributes, it is included in the analysis.

6.2 Particle Identification and Contamination

Once a track is selected for the analysis, identification of the particle type is an important next step. As charged particles traverse the TPC, they lose energy when ionizing the TPC gas. This specific energy loss is a function of velocity,
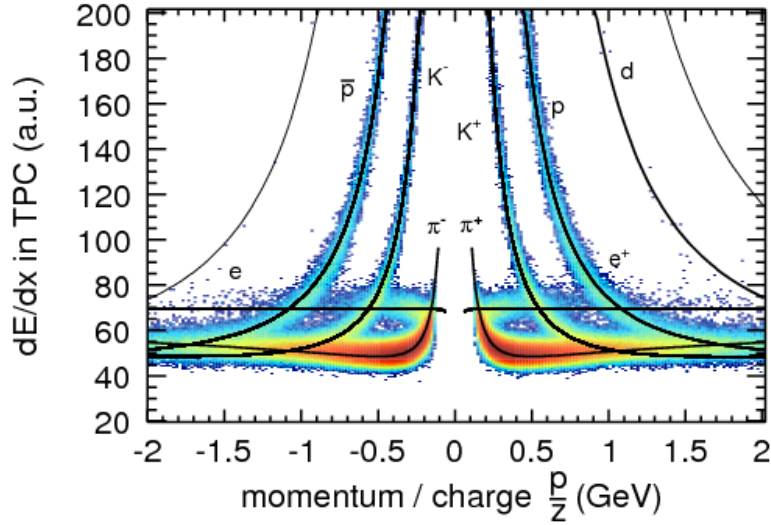
Figure 6.1: Ionization energy loss as a function of particle momentum divided by electric charge for TPC tracks

and is therefore different for different particles at a given momentum. A value, $n_\sigma(\pi)$, is given to each track in an event describing how many standard deviations away it's energy loss is from the expected energy loss for a pion on the ionization energy loss curve shown in Fig. 6.1; the ideal curves showing the expected energy loss for each species are given as black lines. Each track is also given values of $n_\sigma(p)$, $n_\sigma(k)$, and $n_\sigma(e)$ describing how close they are to ideal protons, kaons, and electrons. For example if a track has an $n_\sigma(\pi)$ value of zero and a momentum at which the ideal energy loss curves don't intersect, it is very likely a pion and should be included in the analysis.

If the data set strictly contained pions, the $n_\sigma(\pi)$ distribution would be gaussian centered around zero. However as seen in Fig. 6.2 it is not exactly gaussian. Although it looks gaussian near $n_\sigma(\pi) = 0$, there is a clear shoulder on the left side due to kaon and proton contamination and a smaller shoulder to the right from electron contamination. To account for this contamination, we fit the $n_\sigma(\pi)$

distribution with a 5-gaussian fit; one gaussian for each particle species plus one gaussian to account for the tail at high $n_\sigma(\pi)$ most likely due to pile up or merged tracks.

Several of the degrees of freedom of the fit can be constrained for physical reasons. First, the expected $n_\sigma(\pi)$ value of an ideal kaon can be readily found from fitting a plot of $n_\sigma(\pi)$ vs $n_\sigma(k)$ as in Fig. 6.3. The separation between the pion and kaon gaussians in the 5-gaussian fit is required to be equal to the value of $n_\sigma(\pi)$ at $n_\sigma(k) = 0$. This is repeated to constrain the separation between the pion and proton gaussians, as well as the separation between the pion and electron gaussians. Secondly, kaons and protons are required to have the same width. Third the "pile up" gaussian is required to have a smaller amplitude and be located at a larger $n_\sigma(\pi)$ than the electron gaussian. This is to make sure it actually does fit the high $n_\sigma(\pi)$ tail. This tail is more prominent at higher track momentum but is sometimes absent at lower momentum.

Armed with this fitting procedure, the location and amount of each particle species becomes clear (Fig. 6.4). A clean sample of pions can be found by selecting tracks with an $n_\sigma(\pi)$ between -1 and 2.5. This choice maximizes the number of pions included in the analysis while not compromising the purity of the pion sample too much.

When interpreting the asymmetry results, it is important to quantify the pion purity of the data. As the ionization energy loss curves show (Fig. 6.1), the energy loss depends on track momentum. More importantly, each particle species displays a different energy loss behavior. Some of these energy loss curves even cross each other at track momentum between 1 and 2 GeV/c, making it hard to determine the contamination in the pion data set all at once. Instead the data set is broken into 5 bins in track momentum and 5 in detector θ (the polar angle measured with respect to the beam direction). In each of these bins, the 5-gaussian fitting procedure is repeated. The 5 gaussian fits are shown in Fig. 6.5 to 6.9. For the
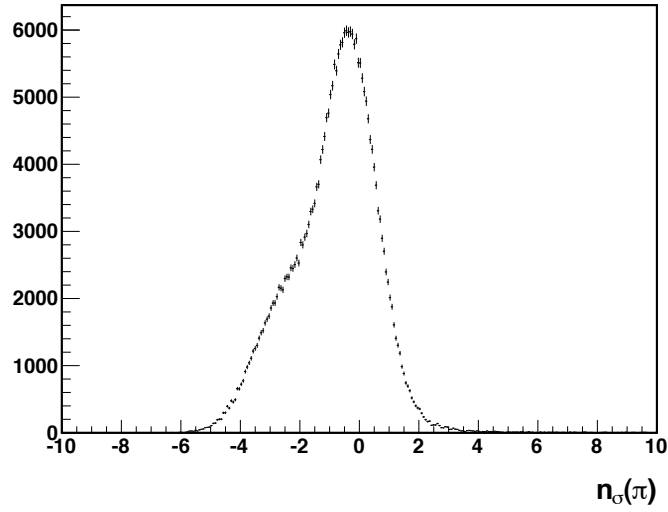
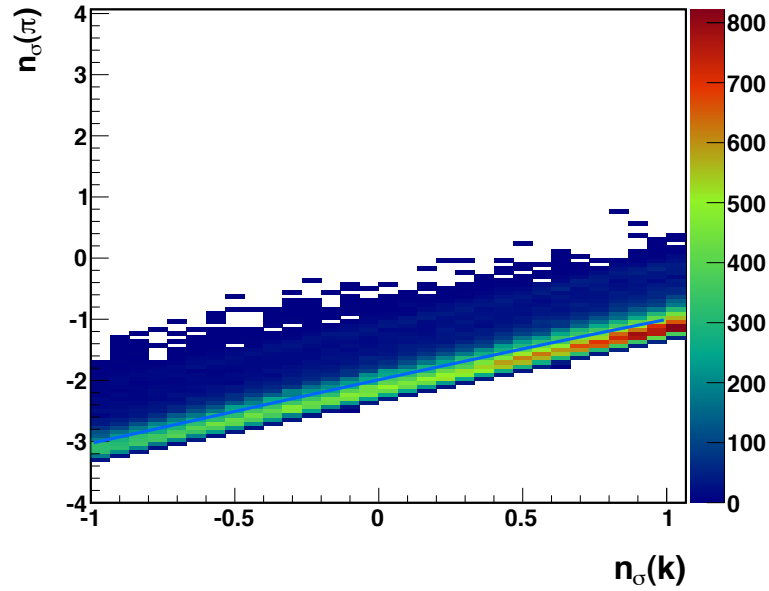Figure 6.2: $n_\sigma(\pi)$ distribution of TPC tracks

Figure 6.3: $n_\sigma(\pi)$ versus $n_\sigma(k)$ The blue line is a 3rd order polynomial fit of the profile. The $n_\sigma(\pi)$ value at $n_\sigma(k) = 0$ is taken as the separation between the pion gaussian and the kaon gaussian in the 5-gaussian fit.

56
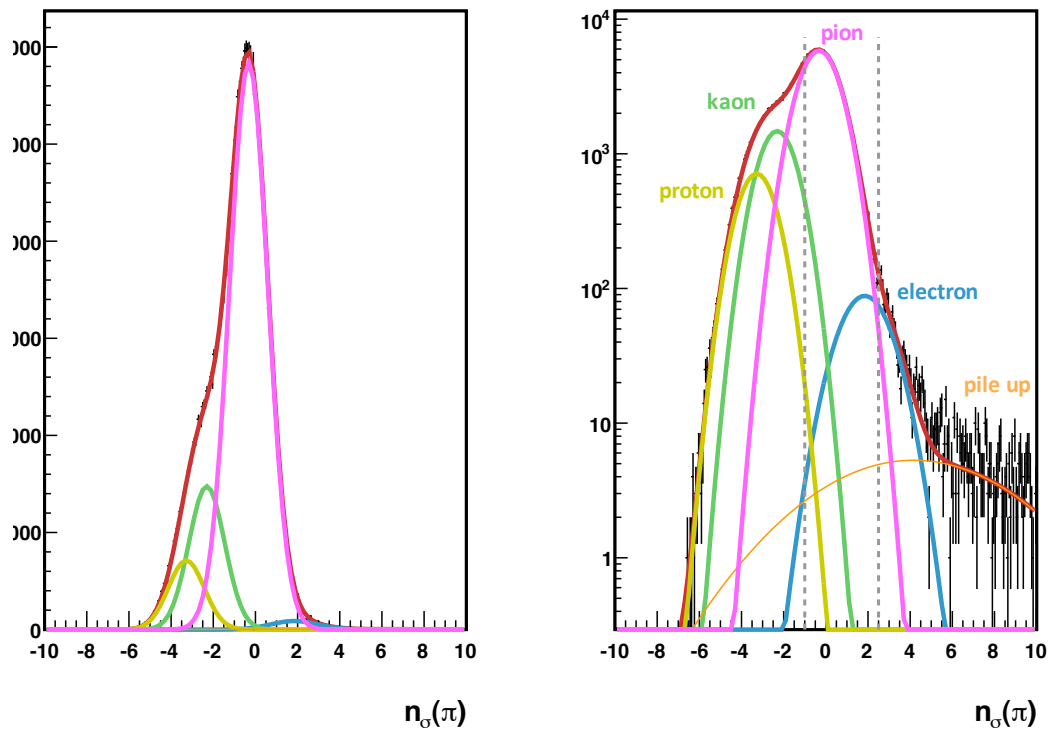
Figure 6.4: 5-gaussian fit of $n_\sigma(\pi)$ distribution. The pion peak is shown in pink, the kaon peak in green, the proton peak in yellow, the electron peak in blue, and the pile up peak in orange. Right panel is a log scale for better visibility of smaller peaks. The red line is the sum of all gaussian fits and matches the histogram almost perfectly. The dashed lines indicate the $-1 < n_\sigma(\pi) < 2.5$ range chosen for the analysis.

four highest track momentum bins, the pion fraction is calculated by integrating the pion gaussian from $n_\sigma(\pi) = -1$ to $n_\sigma(\pi) = 2.5$ and dividing by the integral of the total fit in the same range. As seen in Fig. 6.1, the proton and pion energy loss curves start to overlap in the smallest track momentum bin used (1.5 GeV/c $<$ $p <$ 2.04 GeV/c). This prohibits an accurate determination of the pion fraction using the same method. Luckily in this low momentum range, the time-of-flight can accurately distinguish protons and pions. A two dimensional histogram of M^2 versus $n_\sigma(\pi)$ given in Fig. 6.10 shows how the protons are distinguished from pions. Any particle above the red line is taken to be a proton. The proton fraction is then computed by dividing the number of tracks above the red line by the total number of tracks. The kaon, electron, and pile up fractions can still be computed from integrating the 5-gaussian fits, and the pion fraction is determined by the relationship: $1 - F_k - F_p - F_e - F_{pile-up} = F_\pi$.

Since the actual asymmetry analysis is binned in pion pair transverse momentum, invariant mass, and pseudorapidity, we need to find pion fractions for these bins. These purity fractions were computed from the known pion fractions found in the track momentum and detector θ bins using a weighted mean. The purity values for the analysis binning can be found in tables 6.3 and 6.4. The error for these purity values are on the order of 1×10^{-3}.

Table 6.3: pion purity for 1D binning

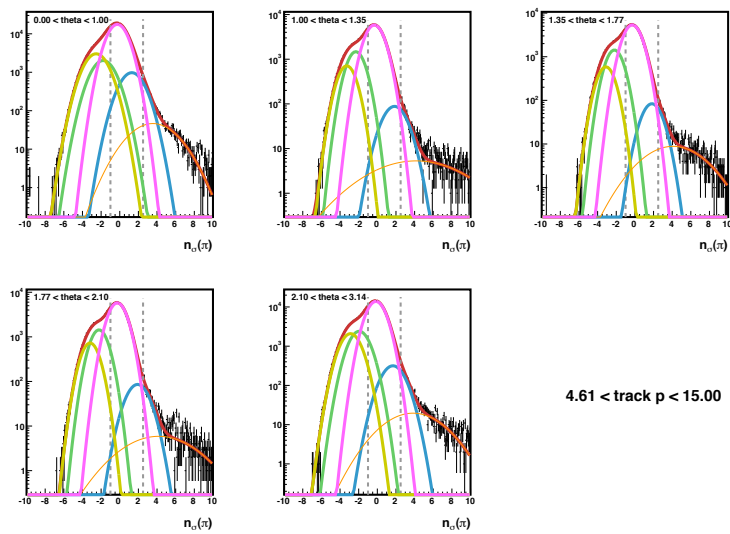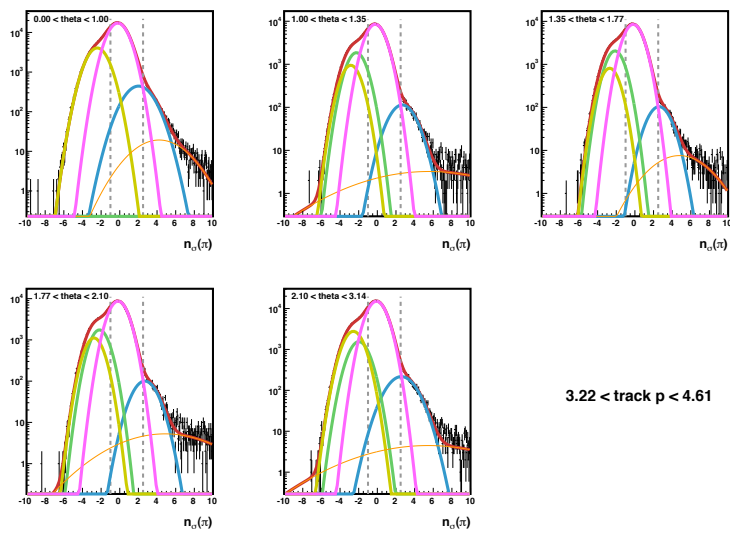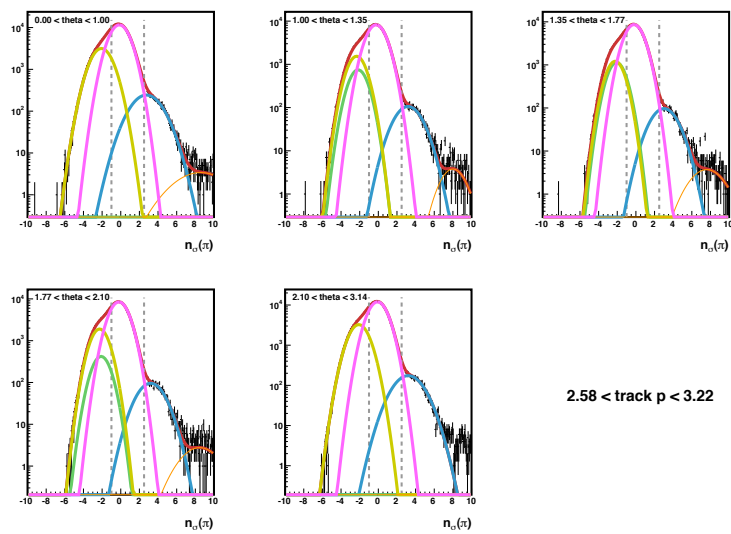| $\eta^{\pi^+\pi^-}$	pion %	$M_{inv}^{\pi^+\pi^-}$	pion %	$P_T^{\pi^+\pi^-}$	pion %
-2.00 $-$ -0.60	95	0.00 $-$ 0.38	94	3.00 $-$ 3.70	93
-0.60 $-$ -0.30	95	0.38 $-$ 0.44	94	3.70 $-$ 4.15	95
-0.30 $-$ 0.00	95	0.44 $-$ 0.50	94	4.15 $-$ 4.63	95
0.00 $-$ 0.40	95	0.50 $-$ 0.56	94	4.63 $-$ 5.19	95
0.40 $-$ 0.75	95	0.56 $-$ 0.62	95	5.19 $-$ 5.87	95
0.75 $-$ 2.00	92	0.62 $-$ 0.72	95	5.87 $-$ 6.80	95
		0.72 $-$ 0.86	95	6.80 $-$ 7.80	94
		0.86 $-$ 1.10	94	7.80 $-$ 10.00	94
		1.10 $-$ 100	94	10.00 $-$ 50.00	94

Figure 6.5

Figure 6.6

Figure 6.7

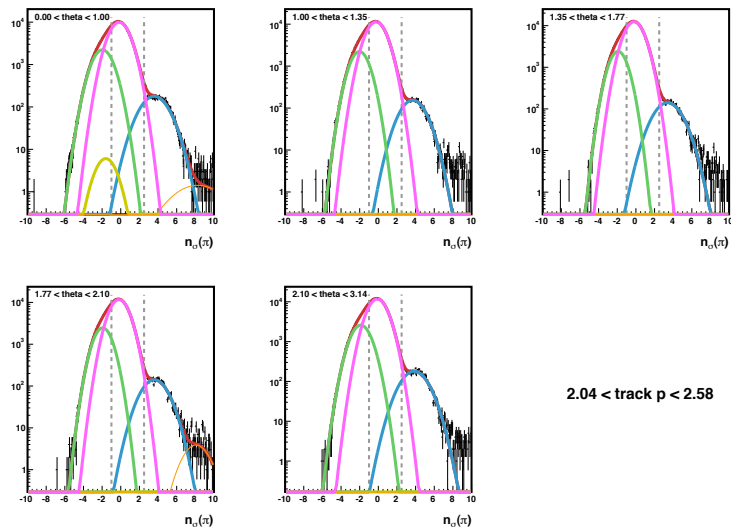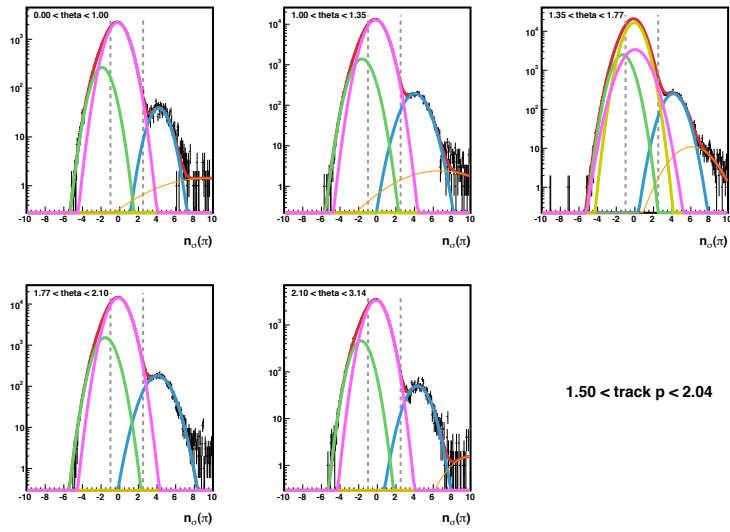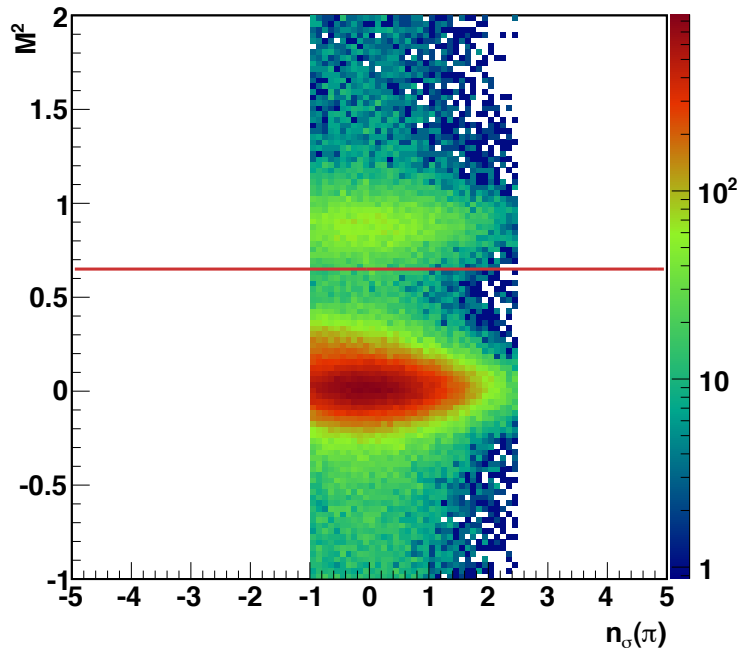Figure 6.8

Figure 6.9

Figure 6.10

Table 6.4: pion purity for 2D binning

| $M_{inv}^{\pi^+\pi^-}$	$\eta^{\pi^+\pi^-}$	pion %	$P_T^{\pi^+\pi^-}$	$M_{inv}^{\pi^+\pi^-}$	pion %	$P_T^{\pi^+\pi^-}$	$\eta^{\pi^+\pi^-}$	pion %
$0.00 - 0.40$	$-2.00 - $ -0.50	96	$3.00 - 4.00$	$0.00 - 0.40$	94	$3.00 - 4.00$	$-2.00 - $ -0.50	95
$0.00 - 0.40$	-0.50 $- 0.00$	94	$3.00 - 4.00$	$0.40 - 0.60$	94	$3.00 - 4.00$	-0.50 $- 0.00$	93
$0.00 - 0.40$	$0.00 - 0.50$	94	$3.00 - 4.00$	$0.60 - 0.80$	94	$3.00 - 4.00$	$0.00 - 0.50$	93
$0.00 - 0.40$	$0.50 - 2.00$	94	$3.00 - 4.00$	$0.80 - 1.00$	94	$3.00 - 4.00$	$0.50 - 2.00$	94
$0.40 - 0.60$	$-2.00 - $ -0.50	96	$3.00 - 4.00$	$1.00 - 100.50$	94	$4.00 - 5.00$	$-2.00 - $ -0.50	96
$0.40 - 0.60$	-0.50 $- 0.00$	94	$4.00 - 5.00$	$0.00 - 0.40$	94	$4.00 - 5.00$	-0.50 $- 0.00$	95
$0.40 - 0.60$	$0.00 - 0.50$	94	$4.00 - 5.00$	$0.40 - 0.60$	94	$4.00 - 5.00$	$0.00 - 0.50$	94
$0.40 - 0.60$	$0.50 - 2.00$	94	$4.00 - 5.00$	$0.60 - 0.80$	94	$4.00 - 5.00$	$0.50 - 2.00$	94
$0.60 - 0.80$	$-2.00 - $ -0.50	96	$4.00 - 5.00$	$0.80 - 1.00$	94	$5.00 - 6.50$	$-2.00 - $ -0.50	96
$0.60 - 0.80$	-0.50 $- 0.00$	94	$4.00 - 5.00$	$1.00 - 100.50$	94	$5.00 - 6.50$	-0.50 $- 0.00$	95
$0.60 - 0.80$	$0.00 - 0.50$	94	$5.00 - 6.50$	$0.00 - 0.40$	95	$5.00 - 6.50$	$0.00 - 0.50$	94
$0.60 - 0.80$	$0.50 - 2.00$	94	$5.00 - 6.50$	$0.40 - 0.60$	94	$5.00 - 6.50$	$0.50 - 2.00$	94
$0.80 - 1.00$	$-2.00 - $ -0.50	96	$5.00 - 6.50$	$0.60 - 0.80$	94	$6.50 - 8.00$	$-2.00 - $ -0.50	96
$0.80 - 1.00$	-0.50 $- 0.00$	94	$5.00 - 6.50$	$0.80 - 1.00$	94	$6.50 - 8.00$	-0.50 $- 0.00$	94
$0.80 - 1.00$	$0.00 - 0.50$	94	$5.00 - 6.50$	$1.00 - 100.50$	94	$6.50 - 8.00$	$0.00 - 0.50$	94
$0.80 - 1.00$	$0.50 - 2.00$	94	$6.50 - 8.00$	$0.00 - 0.40$	94	$6.50 - 8.00$	$0.50 - 2.00$	94
$1.00 - 100.50$	$-2.00 - $ -0.50	96	$6.50 - 8.00$	$0.40 - 0.60$	94	$8.00 - 50.00$	$-2.00 - $ -0.50	95
$1.00 - 100.50$	-0.50 $- 0.00$	95	$6.50 - 8.00$	$0.60 - 0.80$	94	$8.00 - 50.00$	-0.50 $- 0.00$	94
$1.00 - 100.50$	$0.00 - 0.50$	94	$6.50 - 8.00$	$0.80 - 1.00$	94	$8.00 - 50.00$	$0.00 - 0.50$	93
$1.00 - 100.50$	$0.50 - 2.00$	94	$6.50 - 8.00$	$1.00 - 100.50$	94	$8.00 - 50.00$	$0.50 - 2.00$	94
			$8.00 - 50.00$	$0.00 - 0.40$	94			
			$8.00 - 50.00$	$0.40 - 0.60$	94			
			$8.00 - 50.00$	$0.60 - 0.80$	94			
			$8.00 - 50.00$	$0.80 - 1.00$	94			
			$8.00 - 50.00$	$1.00 - 100.50$	94			

6.3 Finding $\pi^+\pi^-$ Pairs

Once a clean pion sample is found, π^+s and π^-s must be combined into $\pi^+\pi^-$ pairs. An example of an event of interest can be seen in Fig. 6.11a. Here we see a positively charged pion and negatively charged pion produced in close proximity by the proton collision. This is what we refer to as a pion pair. Every combination of π^+ and π^- in an event is checked. Since the two pions are required to be from the same fragmenting quark, they are taken as a pair and used in the analysis if they pass the individual track cuts and if they are contained in a cone of a certain radius in $\eta - \phi$ space (Fig. 6.11b). For 1D binning, radii of 0.2, 0.3, and 0.4 are used, while 0.7 is used in 2D binning in order to increase statistics. Even the largest of these radii should still be effective to ensure the the two pions are from the same fragmenting quark.

Figure 6.11: Schematic of Analysis

(a) pion pair produced in collision

(b) radius check on pion pair
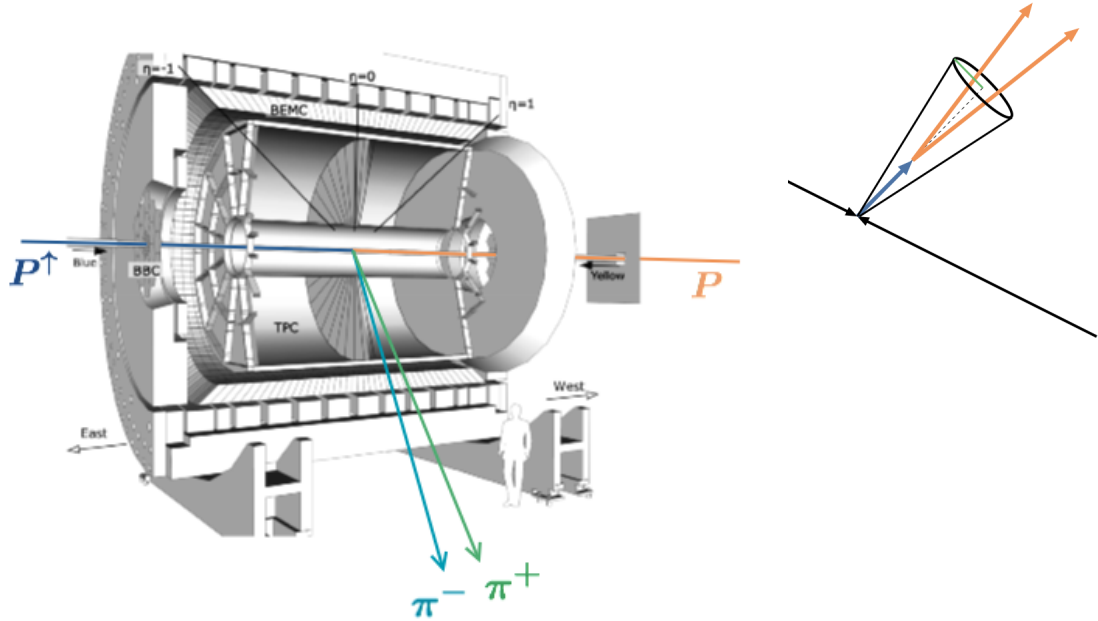
6.4   Pair Distributions

The entire data set provides 17544516 $\pi^+\pi^-$ pairs in a radius between 0.05 and 1.0 in η, ϕ space before trigger information is used. The minimum radius cut of 0.05 is used because when the tracks are very close together, the uncertainty in track position can cause the orientation of the pairs to flip. Since the orientation of the pair is so important to the observed asymmetry, this is unacceptable for our analysis.

Once the data set was ready, quality tests were performed on the pion pairs. These included looking at the invariant mass, transverse momentum, and pseu-dorapidity distributions for the pairs. Quality control plots of relevant kinematic variables of individual pions and pion pairs with a maximum radius of 0.3 can be seen in Figs. 6.12 to 6.29.
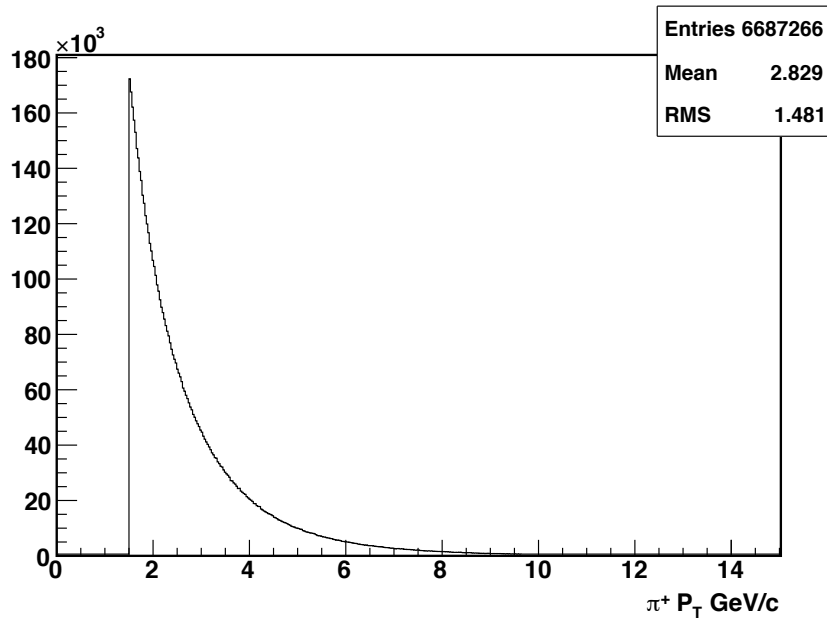
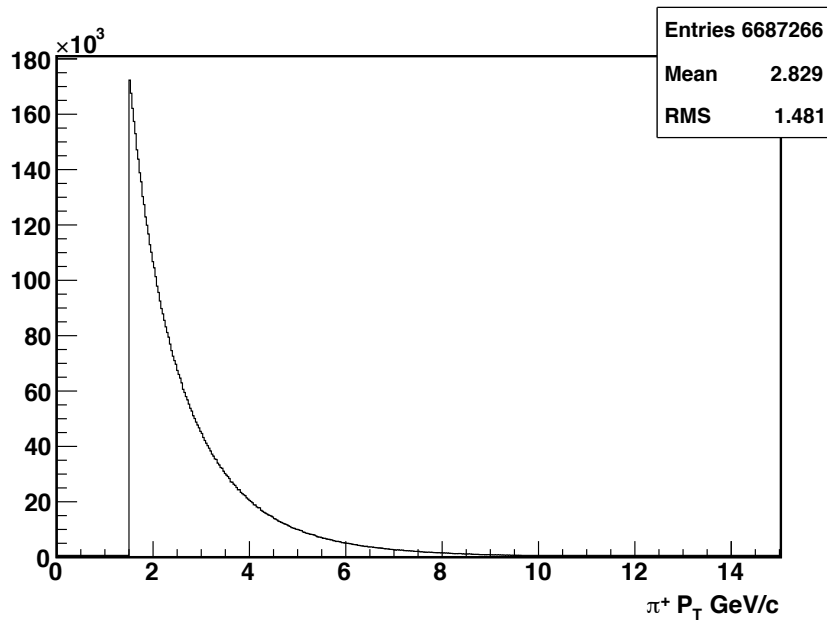Figure 6.12: P_T distribution of π^+

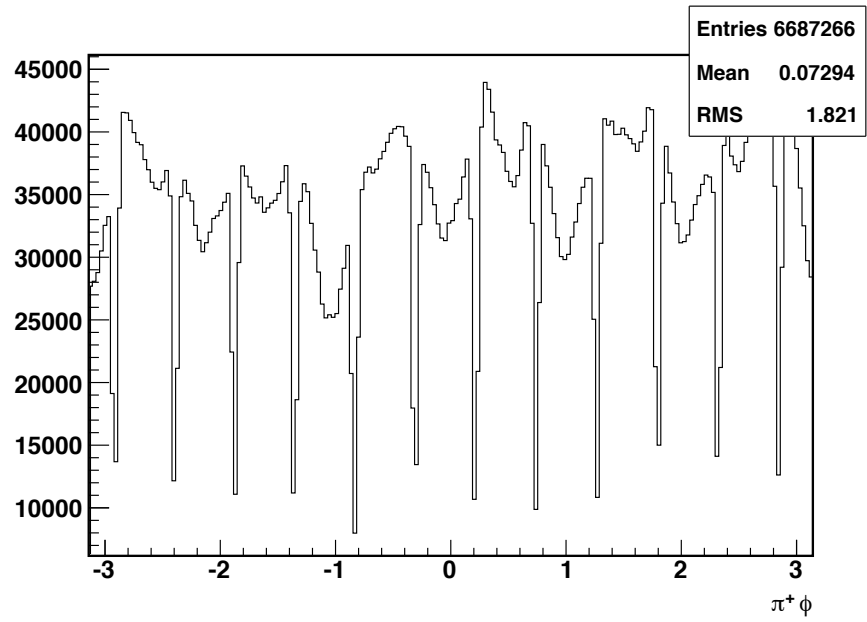Figure 6.13: P_T distribution of π^-
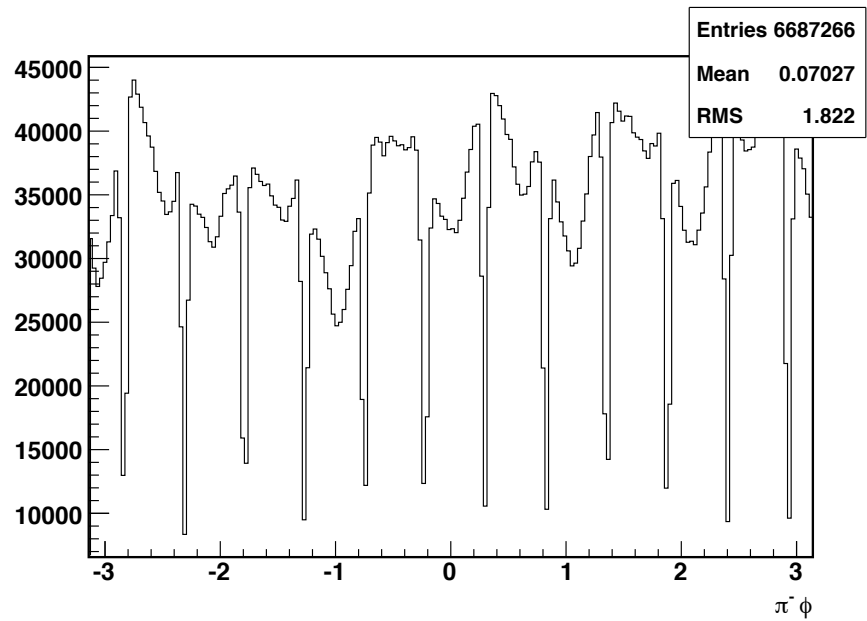
Figure 6.14: ϕ distribution of π^+

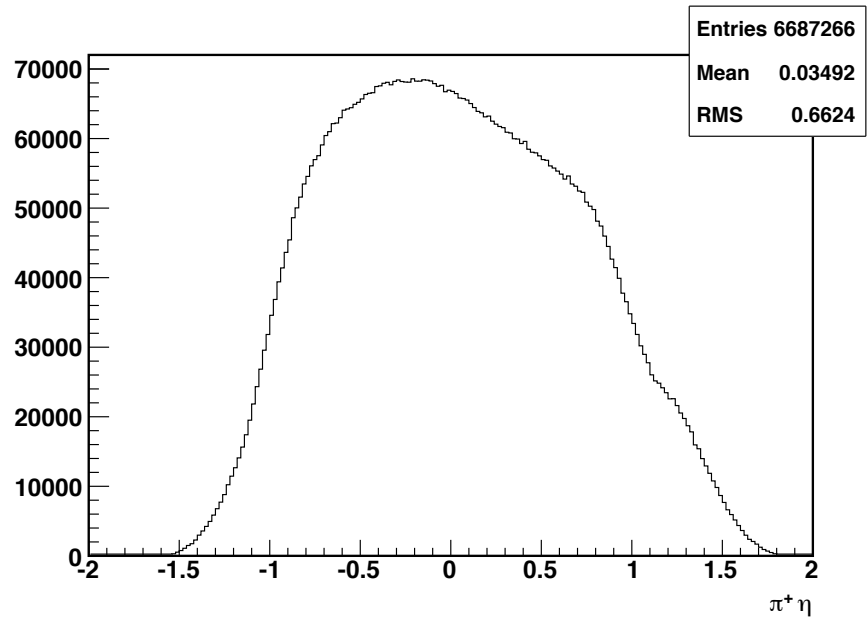Figure 6.15: ϕ distribution of π^-

65

Figure 6.16: η distribution of π^+
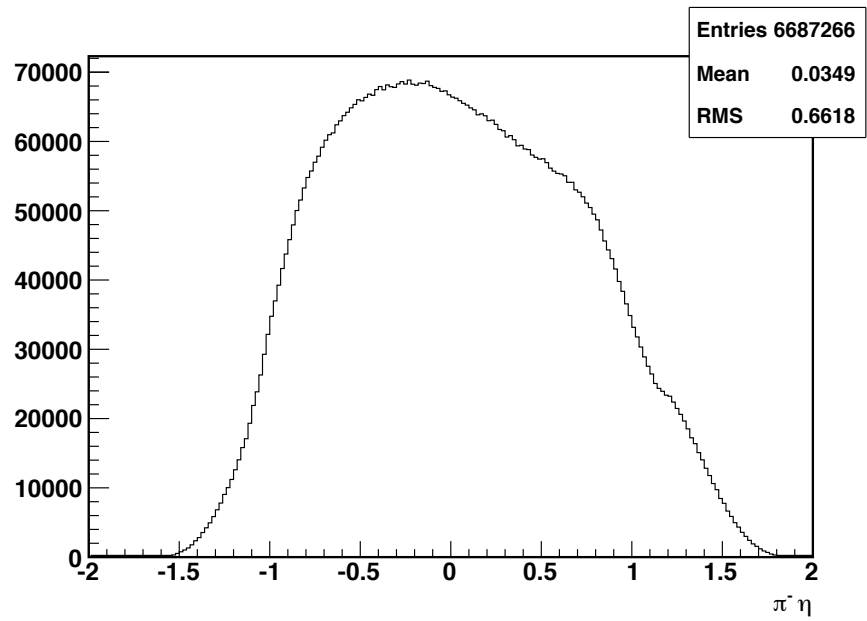

Figure 6.17: η distribution of π^-
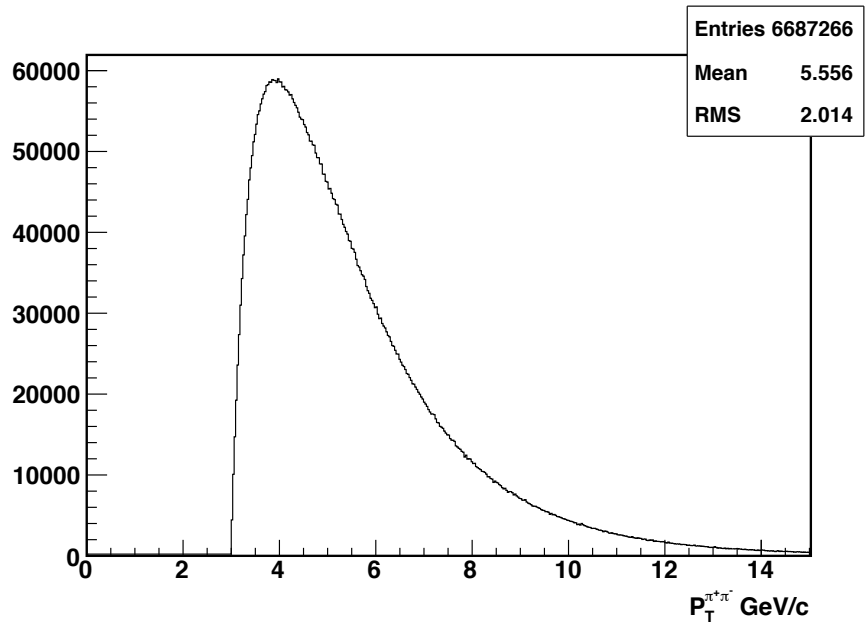
Figure 6.18: P_T distribution of $\pi^+\pi^-$ pair

Figure 6.19: ϕ distribution of $\pi^+\pi^-$ pair

67
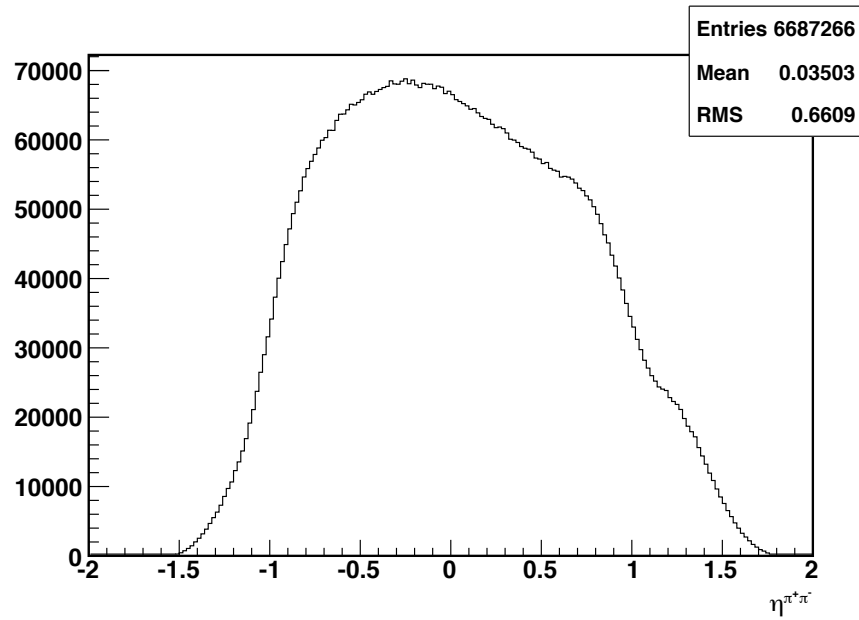
Figure 6.20: η distribution of $\pi^+\pi^-$ pair
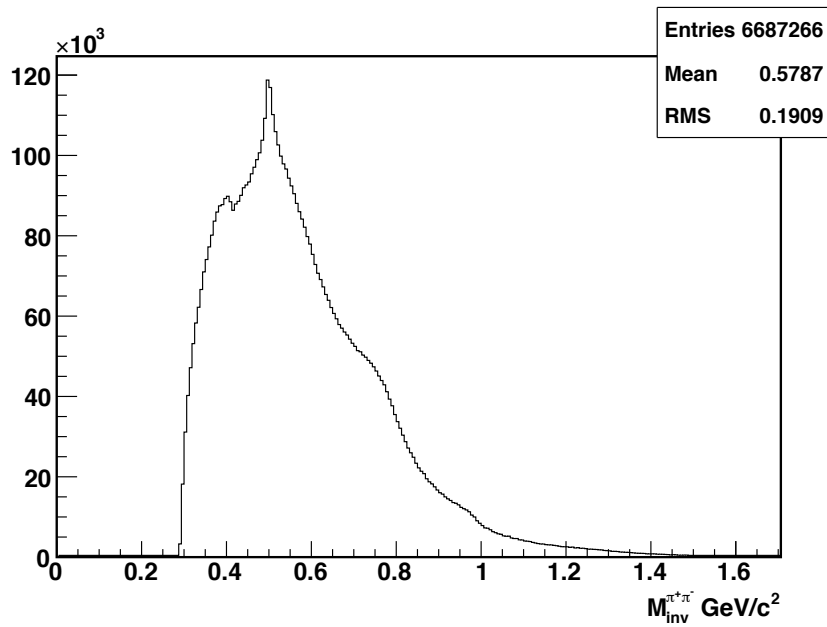
Figure 6.21: Invariant mass distribution of $\pi^+\pi^-$ pair

Figure 6.22: ϕ_R distribution of $\pi^+\pi^-$ pair with reference to the yellow beam polarization

69
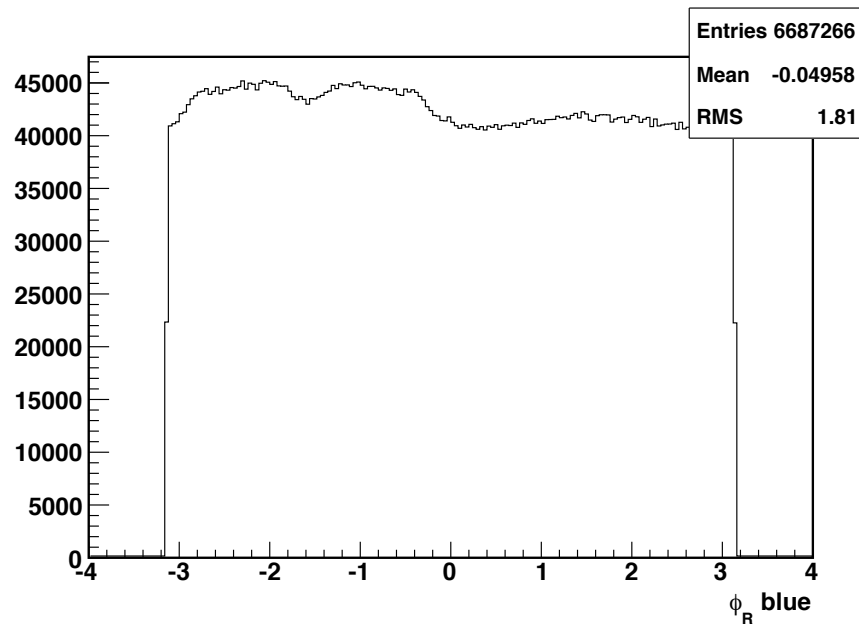
Figure 6.23: ϕ_R distribution of $\pi^+\pi^-$ pair with reference to the blue beam polarization
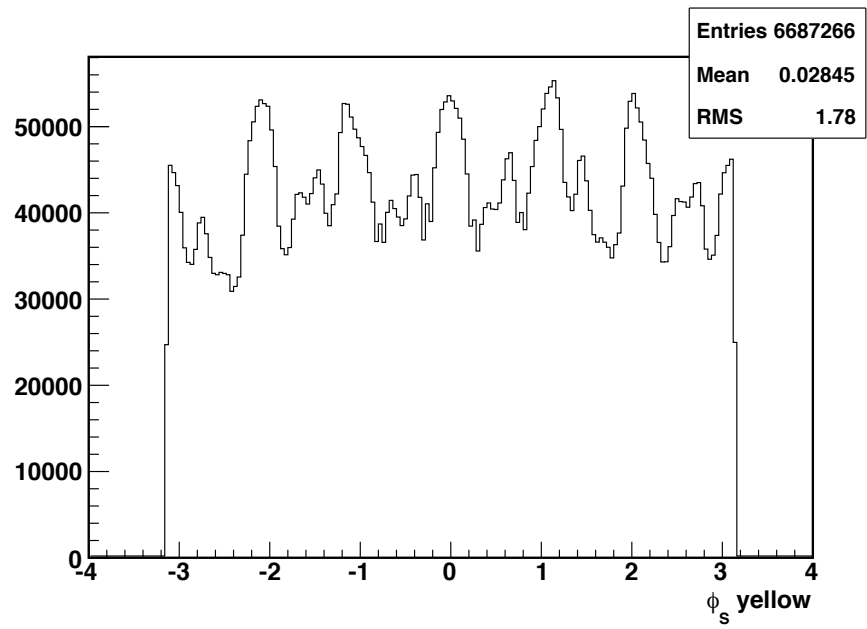
Figure 6.24: ϕ_S distribution of $\pi^+\pi^-$ pair with reference to the yellow beam polarization
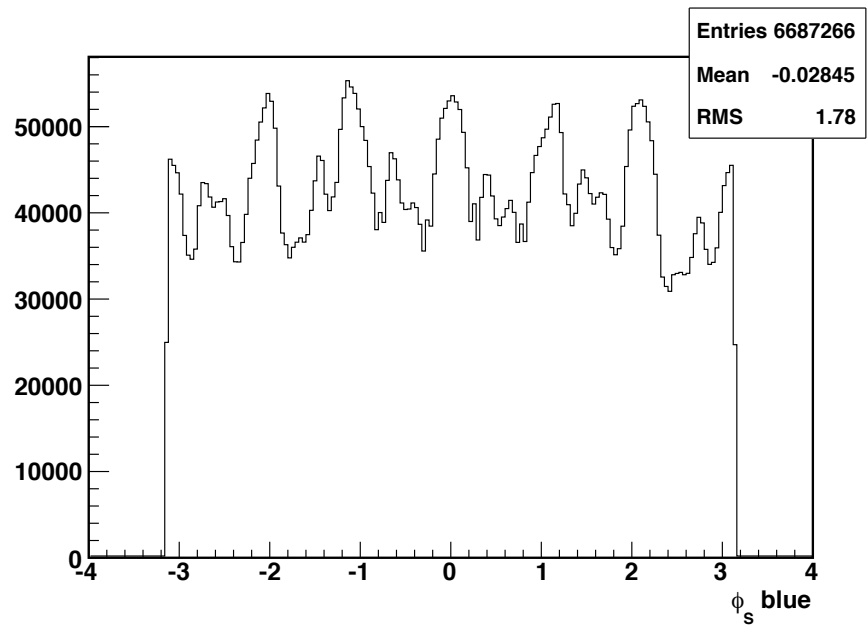
Figure 6.25: ϕ_S distribution of $\pi^+\pi^-$ pair with reference to the blue beam polarization
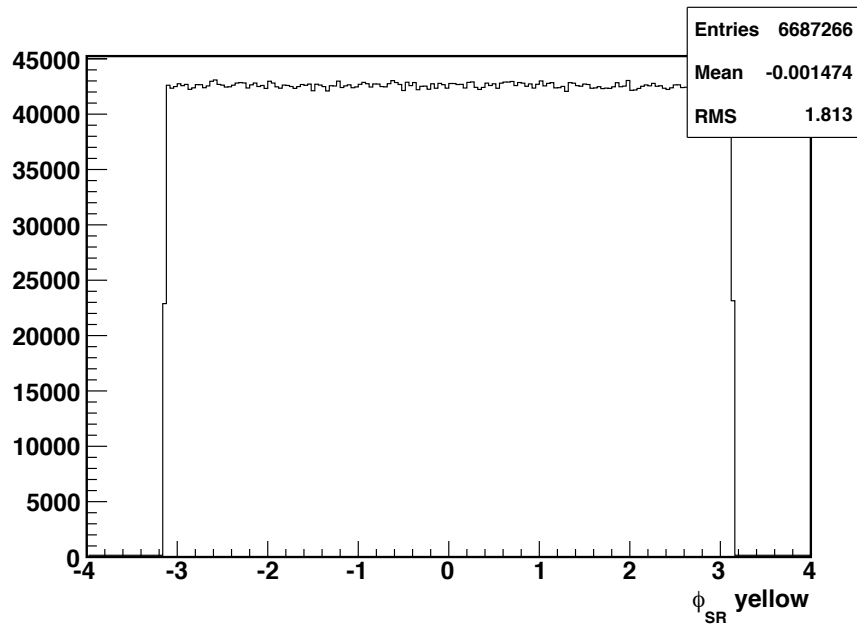
Figure 6.26: ϕ_{RS} distribution of $\pi^+\pi^-$ pair with reference to the yellow beam polarization. This is the angle of interest in the sinusoidal modulation in asymmetry and is expected to be flat when spin state is integrated over as it is here.

Figure 6.27: ϕ_{RS} distribution of $\pi^+\pi^-$ pair with reference to the blue beam polarization. This is the angle of interest in the sinusoidal modulation in asymmetry and is expected to be flat when spin state is integrated over as it is here.

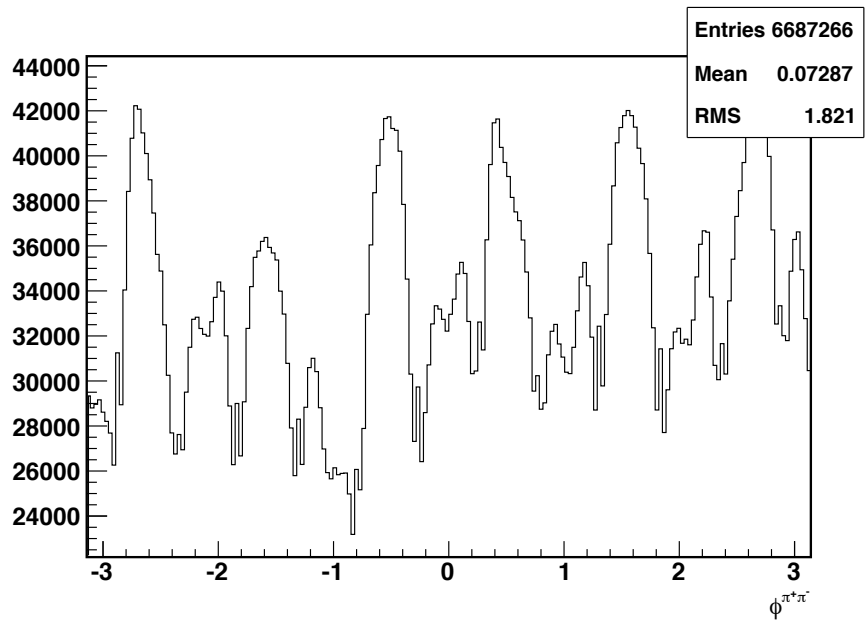| Entries	6687266
Mean	1.565
RMS	0.3216
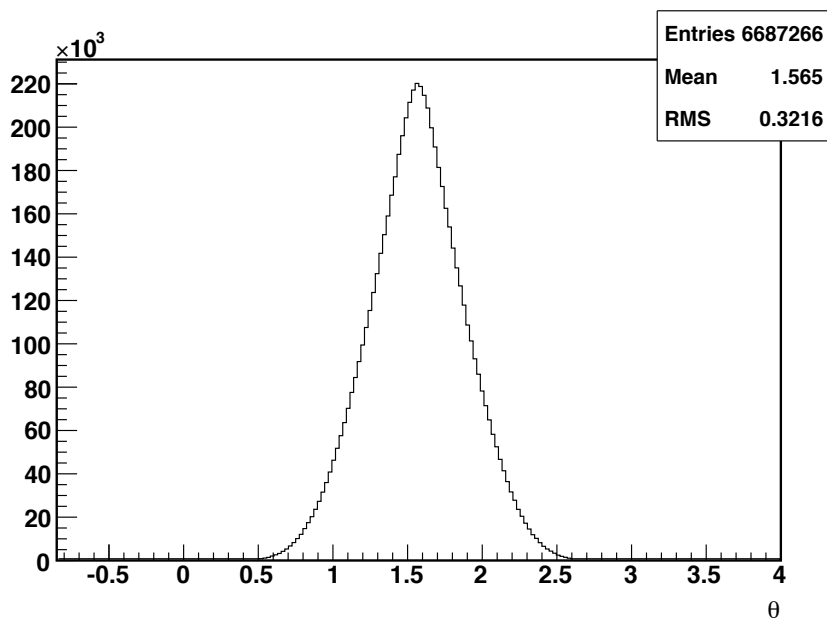
Figure 6.28: θ distribution of $\pi^+\pi^-$ pair
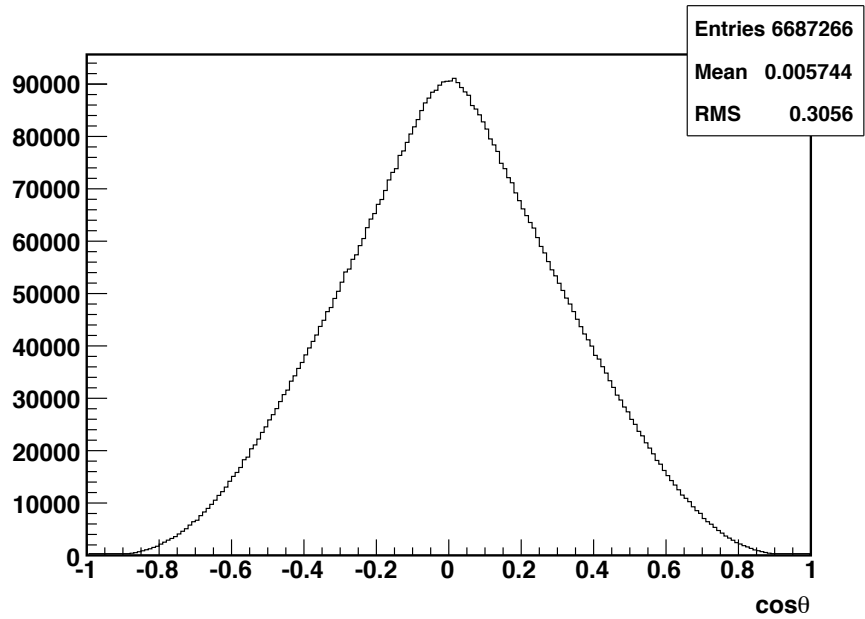
Figure 6.29: $\cos\theta$ distribution of $\pi^+\pi^-$ pair
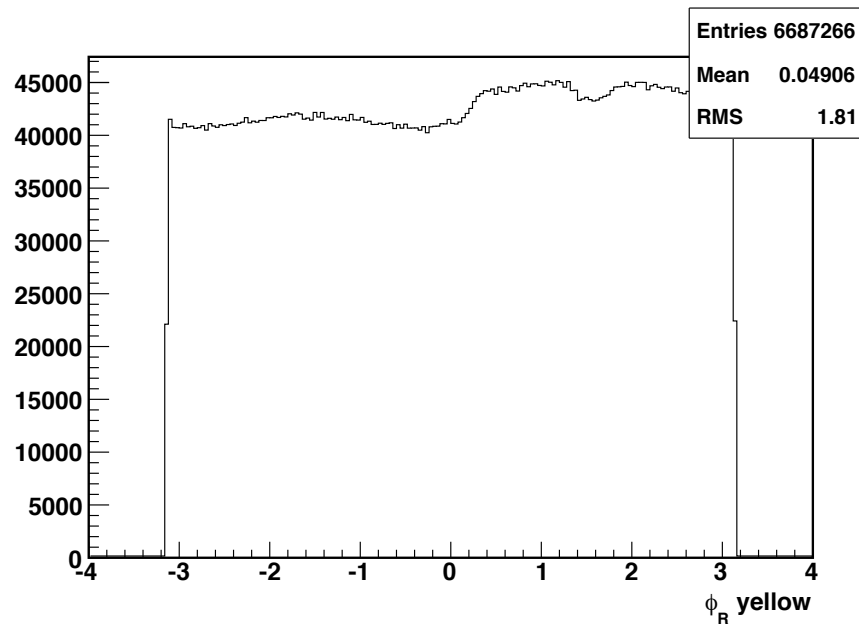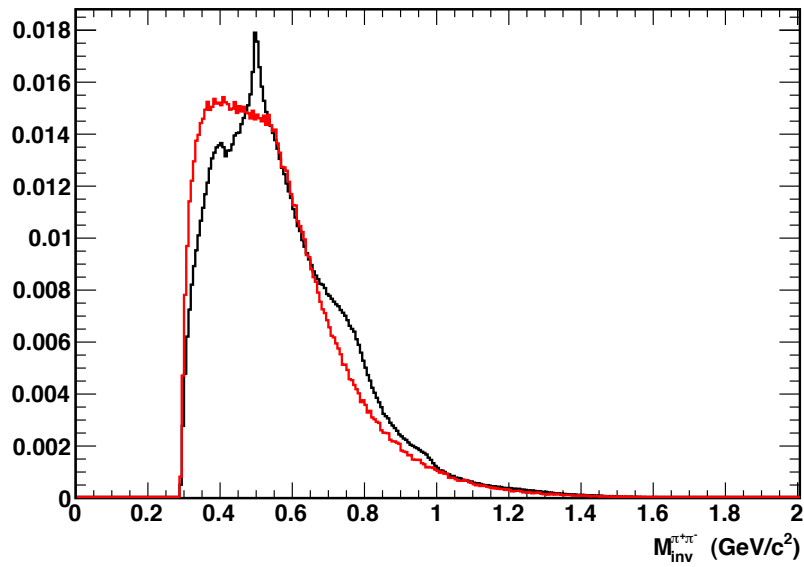

Figure 6.30: Invariant mass of $\pi^+\pi^-$ pairs (black) and $\pi^+\pi^+,\pi^-\pi^-$ pairs (red). The histograms are normalized to a total area of 1 unit to account for differing numbers of opposite and same sign pairs found.

6.5 Calculating The Asymmetry

6.5.1 Luminosity Method

The asymmetry is calculated as in Eqn. 6.1. We take the ratio of the difference of pion pairs from spin up events and spin down events, weighted by the luminosity of the beam state, to the total number of pion pairs produced.

$$A_{UT}P\sin\left(\phi_{RS}\right) = \frac{\frac{N^{\uparrow}}{L^{\uparrow}} - \frac{N^{\downarrow}}{L^{\downarrow}}}{\frac{N^{\uparrow}}{L^{\uparrow}} + \frac{N^{\downarrow}}{L^{\downarrow}}} \tag{6.1}$$

Where ϕ_{RS} can take values from $-\pi$ to π.

This method requires the knowledge of beam luminosity. Since this is not known exactly, the presence of the luminosity in the calculation introduces another source of error. This is not ideal especially for such a sensitive analysis. We introduce here another way to determine the asymmetry.

6.5.2 Cross Ratio Method

A more clever way of constructing the asymmetry is with the cross ratio method [34]. I break the angle ϕ_{RS} up into 32 bins. I then count the number of pion pairs in that ϕ_{RS} bin when the polarization is up $N^{\uparrow}_{\phi_{RS}}$.

$$N^{\uparrow}_{\phi_{RS}} = L^{\uparrow}I_{\phi_{RS}}(\theta)\left[1 + A_{UT}P\sin(\phi_{RS})\right] \tag{6.2}$$

In the above equation $I_{\phi_{RS}}(\theta)$ is the unpolarized cross section into the designated ϕ_{RS} bin and polar angle θ, $L^{\uparrow}$ is the luminosity when the beam is in the spin up polarization, and P is the polarization of the beam. Next we look at the number of pairs we see in the same ϕ_{RS} bin when the spin is down.

$$N^{\downarrow}_{\phi_{RS}} = L^{\downarrow}I_{\phi_{RS}}(\theta)\left[1 - A_{UT}P\sin(\phi_{RS})\right] \tag{6.3}$$

This time the spin is down so the plus sign in Eqn. 6.2 becomes a negative. Next we want to look at what happens when we change the ϕ_{RS} bin by π. Still counting

when the polarization is spin down we see that:

$$N^{\downarrow}_{\phi_{RS}+\pi} = L^{\downarrow}I_{\phi_{RS}+\pi}(\theta)\left[1 + A_{UT}P\sin(\phi_{RS})\right] \tag{6.4}$$

Since $\sin(x + \pi) = -\sin(x)$, the negative sign from Eqn. 6.3 has flipped again. Finally if we look at bin $\phi_{RS} + \pi$, with a spin up polarization we see the sign flip one more time.

$$N^{\uparrow}_{\phi_{RS}+\pi} = L^{\uparrow}I_{\phi_{RS}+\pi}(\theta)\left[1 - A_{UT}P\sin(\phi_{RS})\right] \tag{6.5}$$

We then define "left" and "right"[1] as

$$\mathcal{L} = \sqrt{N^{\uparrow}_{\phi_{RS}}N^{\downarrow}_{\phi_{RS}+\pi}} = \sqrt{L^{\uparrow}L^{\downarrow}I_{\phi_{RS}}I_{\phi_{RS}+\pi}}\left[1 + A_{UT}P\sin(\phi_{RS})\right] \tag{6.6}$$

$$\mathcal{R} = \sqrt{N^{\downarrow}_{\phi_{RS}}N^{\uparrow}_{\phi_{RS}+\pi}} = \sqrt{L^{\uparrow}L^{\downarrow}I_{\phi_{RS}}I_{\phi_{RS}+\pi}}\left[1 - A_{UT}P\sin(\phi_{RS})\right] \tag{6.7}$$

The combination $\frac{\mathcal{L}-\mathcal{R}}{\mathcal{L}+\mathcal{R}}$ gives an expression independent of luminosities.

$$\frac{\mathcal{L}-\mathcal{R}}{\mathcal{L}+\mathcal{R}} = \frac{\sqrt{N^{\uparrow}_{\phi_{RS}}N^{\downarrow}_{\phi_{RS}+\pi}} - \sqrt{N^{\downarrow}_{\phi_{RS}}N^{\uparrow}_{\phi_{RS}+\pi}}}{\sqrt{N^{\uparrow}_{\phi_{RS}}N^{\downarrow}_{\phi_{RS}+\pi}} + \sqrt{N^{\downarrow}_{\phi_{RS}}N^{\uparrow}_{\phi_{RS}+\pi}}} = A_{UT}P\sin(\phi_{RS}) \tag{6.8}$$

or in other words

$$A_{UT}\sin(\phi_{RS}) = \frac{1}{P}\frac{\sqrt{N^{\uparrow}_{\phi_{RS}}N^{\downarrow}_{\phi_{RS}+\pi}} - \sqrt{N^{\downarrow}_{\phi_{RS}}N^{\uparrow}_{\phi_{RS}+\pi}}}{\sqrt{N^{\uparrow}_{\phi_{RS}}N^{\downarrow}_{\phi_{RS}+\pi}} + \sqrt{N^{\downarrow}_{\phi_{RS}}N^{\uparrow}_{\phi_{RS}+\pi}}} \tag{6.9}$$

Equation 6.9 is called the cross ratio and is used throughout this analysis. As stated above, this form of the asymmetry has the advantage that luminosity and detector effects are canceled. This helps us for multiple reasons. The uncertainty in luminosity is difficult to pin down as the luminosity can fluctuate. So not

---

[1]Called left and right because the cross ratio was first used in experiments measuring asymmetries in particle production detected in two different detectors. One of these detectors was situated to the left of the incident beam and the other to the right.

having to take this into account is very beneficial. Also detector irregularities causing more pairs to be found near a "hot tower" are canceled.

One thing to note is that only 16 of the original 32 ϕ_{RS} bins are unique because of double-counting. This is because I use the same number for $N^{\uparrow}_{\phi_{RS}}$ for ϕ_{RS} bin 1 and for $N^{\uparrow}_{\phi_{RS}+\pi}$ for ϕ_{RS} bin 9. The unique range of ϕ_{RS} I choose to use is $-\pi/2$ to $\pi/2$

In order to extract the asymmetry, a histogram of $\frac{1}{P}\frac{\mathcal{L}-\mathcal{R}}{\mathcal{L}+\mathcal{R}}$ is constructed. This is then fit with a sine function with the resulting amplitude of the fit is taken as A_{UT}. This is done for different kinematic bins. An example of this fitting for different pair transverse momentum bins and a radius cut of 0.3 is shown in figure 6.31.

The errors for $N^{\uparrow}$ and $N^{\downarrow}$ in each ϕ_{RS} bin is taken as the poisson error of $\sqrt{N^{\uparrow}}$ or $\sqrt{N^{\uparrow}}$ for that bin. By propagating this through, we find the relevant bin error:

$$
\delta\left(\frac{1}{P}\frac{\mathcal{L}-\mathcal{R}}{\mathcal{L}+\mathcal{R}}\right)_{\phi_{RS}} = \frac{1}{P^2\left(\sqrt{N^{\uparrow}_{\phi_{RS}}N^{\downarrow}_{\phi_{RS}+\pi}} + \sqrt{N^{\downarrow}_{\phi_{RS}}N^{\uparrow}_{\phi_{RS}+\pi}}\right)^2}
$$
$$
\times \sqrt{P^2\left[N^{\uparrow}_{\phi_{RS}+\pi}N^{\downarrow}_{\phi_{RS}}\left(N^{\downarrow}_{\phi_{RS}+\pi} + N^{\uparrow}_{\phi_{RS}}\right) + N^{\downarrow}_{\phi_{RS}+\pi}N^{\uparrow}_{\phi_{RS}}\left(N^{\uparrow}_{\phi_{RS}+\pi} + N^{\downarrow}_{\phi_{RS}}\right)\right]}
$$

(6.10)

A smaller contribution to the total error due to the error on the polarization measurement is neglected because it is significantly smaller than the term shown above.
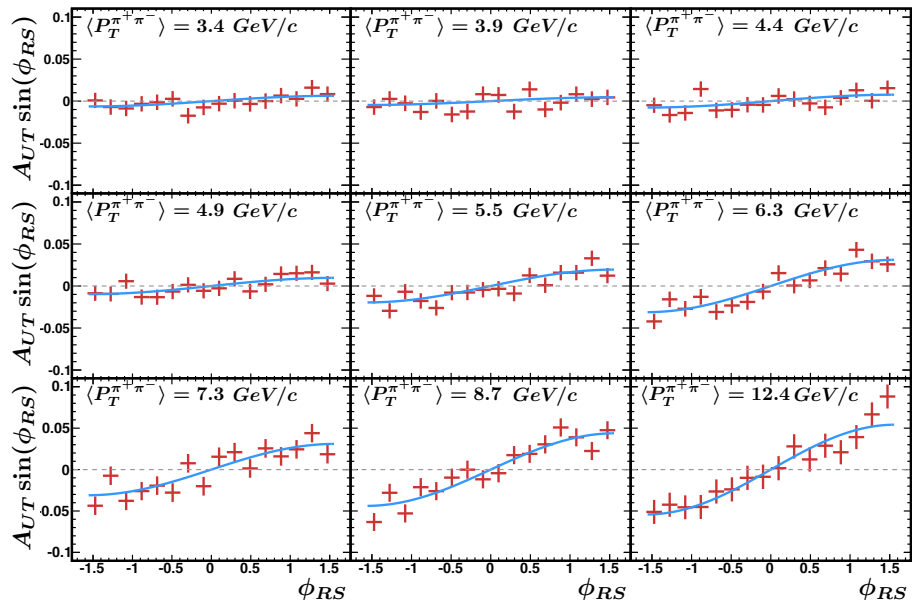
Figure 6.31: Example of the sine fitting. Here different pair transverse momentum ranges are fit with a sine. as the transverse momentum increases, the amplitude of the fit, and thus the asymmetry A_{UT}, increases.

6.6 Analysis Code

The analysis code is broken up into two stages. The first stage finds pion pairs in the raw data and saves them in a "pion pair tree". The second stage analyses all the pairs and calculates the asymmetry.

The relevant files for the first stage are:

/star/u/klandry/ucladisk/2012IFF/xml/2012_200GeV_FinalRunList.txt
/star/u/klandry/ucladisk/2012IFF/xml/makeTrees.xml
/star/u/klandry/ucladisk/2012IFF/xml/submitMakeTrees.sh
/star/u/klandry/ucladisk/2012IFF/StRoot/pionPair/pionPair.h
/star/u/klandry/ucladisk/2012IFF/StRoot/pionPair/pionPair.cxx
/star/u/klandry/ucladisk/2012IFF/StRoot/pionPairTreeMaker/pionPairTreemaker.h
/star/u/klandry/ucladisk/2012IFF/StRoot/pionPairTreeMaker/pionPairTreemaker.cxx
/star/u/klandry/ucladisk/2012IFF/makeTrees.C
/star/u/klandry/ucladisk/2012IFF/StRoot/LoadLibs.C

A diagram of the code flow can be seen in Fig. 6.32.

The first step is to call submitMakeTrees.sh. This loops through the good runs we will use for the analysis in 2012_200GeV_FinalRunList.txt and submits makeTrees.xml to the scheduler with the run number as an input. All the relevent MuDst files for the specific run number are found by the scheduler and made into a file list. Inside makeTrees.xml, this file list is passed as an argument when makeTrees.C runs. In makeTrees.C, a chain of makers is created to carry out the work, one of which is pionPairTreeMaker. This class looks through each event. If two oppositely charged pions are found which pass $n_\sigma(\pi)$, vertex, P_T, and η cuts, it will save the two tracks in an instance of the class pionPair, provided the two pion are less than 1 unit apart in η, ϕ space. The class pionPair stores all the track information for each pion, as well as the trigger and other event information. It also handles all the angle calculations. A .root file is created as output from makeTrees.C for each job. After all jobs are processed, all these files are combined and the second stage is ready to begin.
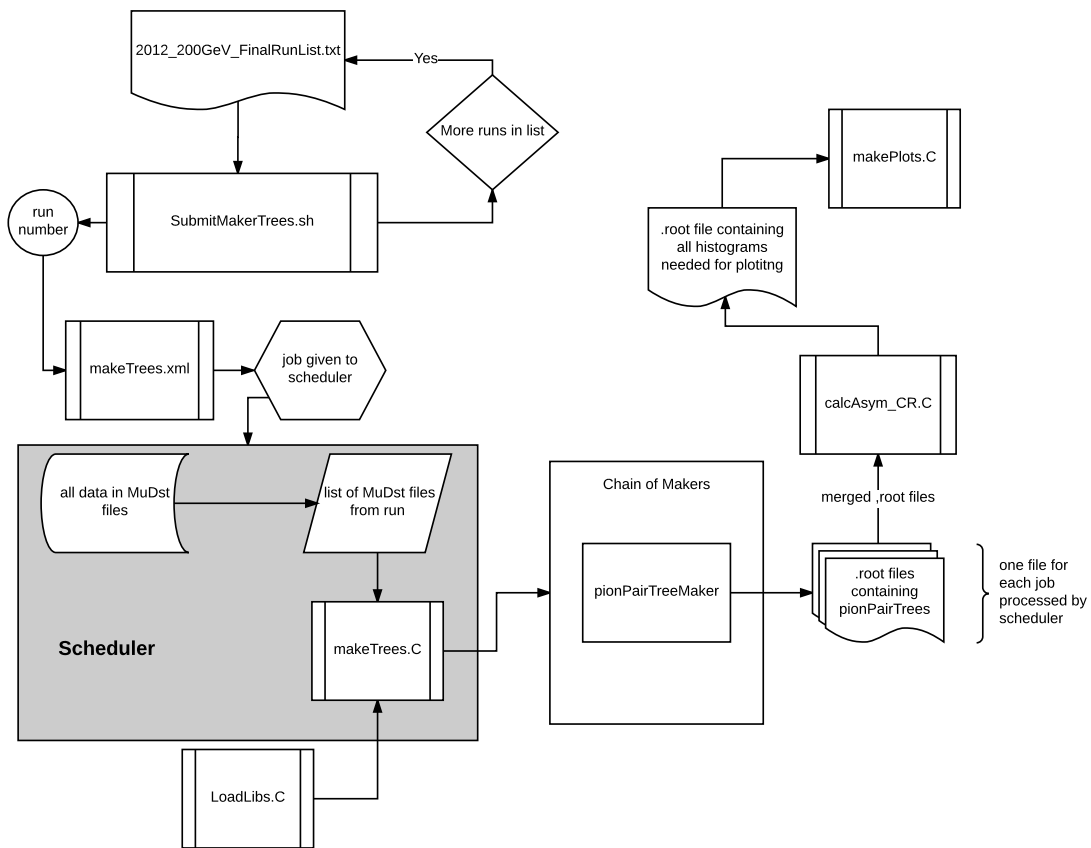
Figure 6.32: Diagram of analysis code flow

The second stage consists mainly of two files:

/star/u/klandry/ucladisk/2012IFF/calcAsym_CR.C

/star/u/klandry/ucladisk/2012IFF/calcAsym_2dCR.C

They are almost identical except calcAsym_2dCR.C keeps the asymmetry differential in two kinematic variables simultaneously while calcAsym_CR.C only keeps it differential in one at a time.

This step carries out the asymmetry calculation. During this calculation, A_{UT} must be kept differential in as many kinematic variables as possible. For this reason, $P_T^{\pi^+\pi^-}$, $M_{inv}^{\pi^+\pi^-}$, and $\eta^{\pi^+\pi^-}$ are divided into different bins. The binning scheme can be seen in table 6.5. The 2D binning scheme used in calcAsym_2dCR.C is shown in table 6.6. For each of these bins, a set of several histograms are created. Two of these histograms are responsible for storing the number of pairs from spin up and from spin down beam states. The x-axis of these histograms, which represents ϕ_{RS}, is divided into 32 bins and range from $-\pi$ to π. For every pair, these histograms are incremented by one at the corresponding value of pair ϕ_{RS}. In this manner they hold the number of pairs from spin up and down protons at every value of ϕ_{RS}. A third histogram is created for each bin to store every pair's kinematic value to be plotted against the calculated asymmetry. The final piece needed in the asymmetry calculation is the polarization of the beam. A final histogram for each bin is required to hold the polarization for each pair.

Since both beams are polarized, we first treat the blue beam as the polarized beam. The histograms are filled according the this beam's polarization. The pair is then revisited with the yellow beam considered the polarized beam, and the histograms are filled again according to this beam's state. Positive $\eta^{\pi^+\pi^-}$ corresponds to the direction of the "polarized" beam. This gives us two values for each pair. Since only one beam is considered polarized at a time, the spin state of the other beam is integrated over. Once all the pairs are processed, the asymmetry calculation begins.

Table 6.5: Binning for asymmetries differential in one kinematic variable

$P_T^{\pi^+\pi^-}$ binning			$M_{inv}^{\pi^+\pi^-}$ binning			$\eta^{\pi^+\pi^-}$ binning		
3.0	-	3.7	0.0	-	0.38	-2	-	-0.6
3.7	-	4.15	0.38	-	0.44	-0.6	-	-0.3
4.15	-	4.63	0.44	-	0.50	-0.3	-	0.0
4.63	-	5.19	0.50	-	0.56	0.0	-	0.4
5.19	-	5.87	0.56	-	0.62	0.4	-	0.75
5.87	-	6.80	0.62	-	0.72	0.75	-	2
6.80	-	7.8	0.72	-	0.86			
7.8	-	10.0	0.86	-	1.1			
10.0	-	50.0	1.1	-	100.5			

As part of the asymmetry calculation, another histogram is created for each kinematic variable bin. It is constructed to be the right hand side of equation 6.9. Like the pion number histograms, it's x-axis corresponds to ϕ_{RS}. The bin errors for this new histogram are calculated using equation 6.10. These new histograms are then fit with a sine function. The amplitude is taken as the value of A_{UT} for that kinematic bin. The output of calcAsym_CR.C is a root file containing all the histograms. These can then quickly be refit and plotted using /star/u/klandry/ucladisk/2012IFF/makePlots.C.

6.6.1 Advanced Treatment of Beam Polarization

The polarization varies from fill to fill due to differences in source and accelerator conditions. Because of this, I attempted a more advanced treatment of the

Table 6.6: Binning for asymmetries differential in two kinematic variables

$P_T^{\pi^+\pi^-}$ binning			$M_{inv}^{\pi^+\pi^-}$ binning			$\eta^{\pi^+\pi^-}$ binning		
3.0	-	4.0	0.0	-	0.4	-2	-	-0.5
4.0	-	5.0	0.4	-	0.6	-0.5	-	0.0
5.0	-	6.5	0.6	-	0.8	0.0	-	0.5
6.5	-	8.0	0.8	-	1.0	0.5	-	2
8.0	-	50.0	1.0	-	100.5			

polarization. The following section will be a detailed explanation of how exactly it is calculated. As an example, I will focus on just one of the kinematic bins with the assumption that this will be done in each kinematic bin separately.

To handle the polarization, histograms are created for each of the 32 ϕ_{RS} bins. These histograms store the beam polarization of pairs from spin up and down events, as well as the error of the beam polarization squared from spin up and spin down events. The latter will be used when calculating errors. Because the average polarization can differ between spin up and down pairs as well as between ϕ_{RS} bins, I alter how the polarization is used in the calculation compared to equation 6.9. Instead of having one value for the polarization, I use several values for the polarization, one for each spin state and ϕ_{RS} bin.

$$A_{UT}\sin(\phi_{RS}) = \frac{\sqrt{\frac{N_{\phi_{RS}}^{\uparrow}}{\left\langle p_{\phi_{RS}}^{\uparrow}\right\rangle}\frac{N_{\phi_{RS}+\pi}^{\downarrow}}{\left\langle p_{\phi_{RS}+\pi}^{\downarrow}\right\rangle}} - \sqrt{\frac{N_{\phi_{RS}+\pi}^{\uparrow}}{\left\langle p_{\phi_{RS}+\pi}^{\uparrow}\right\rangle}\frac{N_{\phi_{RS}}^{\downarrow}}{\left\langle p_{\phi_{RS}}^{\downarrow}\right\rangle}}}{\sqrt{N_{\phi_{RS}}^{\uparrow}N_{\phi_{RS}+\pi}^{\downarrow}} + \sqrt{N_{\phi_{RS}+\pi}^{\uparrow}N_{\phi_{RS}}^{\downarrow}}} \qquad (6.11)$$

Where $\left\langle p_{\phi_{RS}}^{\uparrow}\right\rangle$, $\left\langle p_{\phi_{RS}+\pi}^{\downarrow}\right\rangle$, $\left\langle p_{\phi_{RS}+\pi}^{\uparrow}\right\rangle$, and $\left\langle p_{\phi_{RS}}^{\downarrow}\right\rangle$ are the average beam polarizations in pairs from spin up, down events and at angle ϕ_{RS}, $\phi_{RS}+\pi$. Therefore the number of pairs from each spin state and angle are weighted by their own separate average polarization.

The histogram responsible for storing the values to be fit is now used. The x-axis of this histogram is also separated into 32 ϕ_{RS} bins and ranges from $-\pi$ to π. For each ϕ_{RS} bin the left hand side of Eqn. 6.11 is calculated and used to set the value of the corresponding ϕ_{RS} bin in the fit histogram.

The bin errors seen in Fig. 6.31 are calculated by a somewhat more complicated procedure.

$$\text{Let } \mathcal{E} = \frac{\sqrt{\frac{N^{\uparrow}_{\phi_{RS}}}{\langle p^{\uparrow}_{\phi_{RS}} \rangle} \frac{N^{\downarrow}_{\phi_{RS}+\pi}}{\langle p^{\downarrow}_{\phi_{RS}+\pi} \rangle}} - \sqrt{\frac{N^{\uparrow}_{\phi_{RS}+\pi}}{\langle p^{\uparrow}_{\phi_{RS}+\pi} \rangle} \frac{N^{\downarrow}_{\phi_{RS}}}{\langle p^{\downarrow}_{\phi_{RS}} \rangle}}}{\sqrt{N^{\uparrow}_{\phi_{RS}} N^{\downarrow}_{\phi_{RS}+\pi}} + \sqrt{N^{\uparrow}_{\phi_{RS}+\pi} N^{\downarrow}_{\phi_{RS}}}} \tag{6.12}$$

The error on $\mathcal{E}$ is defined as $\delta\mathcal{E} = \sqrt{E^2_{stat} + E^2_{pol}}$. Where E^2_{stat} is the statistical error and E^2_{pol} is the error from the polarization uncertainty. Let's look at these two individually starting with the statistical error term.

To make our lives easier let's introduce two new variables, $a = \sqrt{N^{\uparrow}_{\phi_{RS}} N^{\downarrow}_{\phi_{RS}+\pi}}$ and $b = \sqrt{N^{\uparrow}_{\phi_{RS}+\pi} N^{\downarrow}_{\phi_{RS}}}$

Rewriting Eqn. 6.12 with these new variables, gives

$$\mathcal{E} = \frac{\frac{a}{\sqrt{\langle p^{\uparrow}_{\phi_{RS}} \rangle \langle p^{\downarrow}_{\phi_{RS}+\pi} \rangle}} - \frac{b}{\sqrt{\langle p^{\uparrow}_{\phi_{RS}+\pi} \rangle \langle p^{\downarrow}_{\phi_{RS}} \rangle}}}{a + b} \tag{6.13}$$

With this notation, the statistical error becomes

$$E^2_{stat} = \left(\frac{\partial \mathcal{E}}{\partial a}\right)^2 \delta a^2 + \left(\frac{\partial \mathcal{E}}{\partial b}\right)^2 \delta b^2 \tag{6.14}$$

The errors on a and b are similarly calculated.

$$\delta a^2 = \left(\frac{\partial a}{\partial N^\uparrow_{\phi_{RS}}}\right)^2 \left(\delta N^\uparrow_{\phi_{RS}}\right)^2 + \left(\frac{\partial a}{\partial N^\downarrow_{\phi_{RS}+\pi}}\right)^2 \left(\delta N^\downarrow_{\phi_{RS}+\pi}\right)^2 \qquad (6.15)$$

$$\delta b^2 = \left(\frac{\partial b}{\partial N^\uparrow_{\phi_{RS}+\pi}}\right)^2 \left(\delta N^\uparrow_{\phi_{RS}+\pi}\right)^2 + \left(\frac{\partial b}{\partial N^\downarrow_{\phi_{RS}}}\right)^2 \left(\delta N^\downarrow_{\phi_{RS}}\right)^2 \qquad (6.16)$$

Taking the errors on the number of pairs in a bin as $\delta N = \sqrt{N}$,

$$\delta a^2 = \frac{1}{4}\left(N^\uparrow_{\phi_{RS}} + N^\downarrow_{\phi_{RS}+\pi}\right) \qquad (6.17)$$

$$\delta b^2 = \frac{1}{4}\left(N^\uparrow_{\phi_{RS}+\pi} + N^\downarrow_{\phi_{RS}}\right) \qquad (6.18)$$

Putting everything together E_{stat} becomes

$$E^2_{stat} = \frac{1}{4}\frac{1}{(a+b)^4}\left[\frac{1}{\sqrt{\left\langle p^\uparrow_{\phi_{RS}}\right\rangle\left\langle p^\downarrow_{\phi_{RS}+\pi}\right\rangle}} + \frac{1}{\sqrt{\left\langle p^\uparrow_{\phi_{RS}+\pi}\right\rangle\left\langle p^\downarrow_{\phi_{RS}}\right\rangle}}\right]^2 \qquad (6.19)$$

$$\times \left[b^2\left(N^\uparrow_{\phi_{RS}} + N^\downarrow_{\phi_{RS}+\pi}\right) + a^2\left(N^\uparrow_{\phi_{RS}+\pi} + N^\downarrow_{\phi_{RS}}\right)\right]$$

Assuming all Ns and polarizations are equal, we see that the statistical error scales like $E^2_{stat} \sim \frac{1}{p^2 N}$; as expected from the simple treatment of the error.

The error from the polarization uncertainty is a little bit trickier to tackle. Since each pair comes with it's own polarization uncertainty, I want to take all of them into account. To do this I have to change how I write $\mathcal{E}$. Namely I want to explicitly write out how each pair's polarization comes in instead of the average polarization.

$$\mathcal{E} = \frac{\sqrt{\frac{N^{\uparrow\,2}_{\phi_{RS}} N^{\downarrow\,2}_{\phi_{RS}+\pi}}{\sum\limits_{i=1}^{N^\uparrow_{\phi_{RS}}} p_i \sum\limits_{j=1}^{N^\downarrow_{\phi_{RS}+\pi}} p_j}} - \sqrt{\frac{N^{\downarrow\,2}_{\phi_{RS}} N^{\uparrow\,2}_{\phi_{RS}+\pi}}{\sum\limits_{n=1}^{N^\downarrow_{\phi_{RS}}} p_n \sum\limits_{m=1}^{N^\uparrow_{\phi_{RS}+\pi}} p_m}}}{a+b} \qquad (6.20)$$

To obtain this form of $\mathcal{E}$ I have used, $\langle p_x \rangle = \frac{1}{N_x} \sum\limits_{x=1}^{N_x} p_x$.

By writing $\mathcal{E}$ as in Eqn. 6.20, we obtain how the polarization uncertainty propagates to the error of $\mathcal{E}$.

$$E_{pol}^2 = \sum_{i=1}^{N_{\phi_{RS}}^{\uparrow}} \left(\frac{\partial \mathcal{E}}{\partial p_i} \right)^2 \delta p_i{}^2 + \sum_{j=1}^{N_{\phi_{RS}+\pi}^{\downarrow}} \left(\frac{\partial \mathcal{E}}{\partial p_j} \right)^2 \delta p_j{}^2 + \sum_{n=1}^{N_{\phi_{RS}}^{\downarrow}} \left(\frac{\partial \mathcal{E}}{\partial p_n} \right)^2 \delta p_n{}^2 + \sum_{m=1}^{N_{\phi_{RS}+\pi}^{\uparrow}} \left(\frac{\partial \mathcal{E}}{\partial p_m} \right)^2 \delta p_m{}^2$$

$$(6.21)$$

Computing the derivative $\frac{\partial \mathcal{E}}{\partial p_i}$ gives,

$$\frac{\partial \mathcal{E}}{\partial p_i} = \frac{-1}{2(a+b)} \frac{a^2 \sum\limits_{j=1}^{N_{\phi_{RS}+\pi}^{\downarrow}} p_j}{\left(\sum\limits_{j=1}^{N_{\phi_{RS}+\pi}^{\downarrow}} p_i \sum\limits_{j=1}^{N_{\phi_{RS}+\pi}^{\downarrow}} p_j \right)^{3/2}} \tag{6.22}$$

Using again the fact that $\langle p_x \rangle = \frac{1}{N_x} \sum\limits_{x=1}^{N_x} p_x$, it follows that

$$\sum_{i=1}^{N_{\phi_{RS}}^{\uparrow}} \left(\frac{\partial \mathcal{E}}{\partial p_i} \right)^2 \delta p_i{}^2 = \sum_{i=1}^{N_{\phi_{RS}}^{\uparrow}} \frac{a^4}{4(a+b)^2} \frac{\delta p_i{}^2}{N_{\phi_{RS}}^{\uparrow}{}^3 \left\langle p_{\phi_{RS}}^{\uparrow} \right\rangle^3 N_{\phi_{RS}+\pi}^{\downarrow} \left\langle p_{\phi_{RS}+\pi}^{\downarrow} \right\rangle} \tag{6.23}$$

$$= \frac{1}{4} \frac{N_{\phi_{RS}+\pi}^{\downarrow}}{(a+b)^2} \frac{\left\langle \delta p_{\phi_{RS}}^{\uparrow}{}^2 \right\rangle}{\left\langle p_{\phi_{RS}}^{\uparrow} \right\rangle^3 \left\langle p_{\phi_{RS}+\pi}^{\downarrow} \right\rangle} \tag{6.24}$$

Each term has a similar form. Putting them all together gives the error from the

polarization uncertainty.

$$E_{pol}^2 = \frac{1}{4(a+b)^2} \left[N_{\phi RS+\pi}^{\downarrow} \frac{\left\langle \delta p_{\phi RS}^{\uparrow}{}^2 \right\rangle}{\left\langle p_{\phi RS}^{\uparrow} \right\rangle^3 \left\langle p_{\phi RS+\pi}^{\downarrow} \right\rangle} + N_{\phi RS}^{\uparrow} \frac{\left\langle \delta p_{\phi RS+\pi}^{\downarrow}{}^2 \right\rangle}{\left\langle p_{\phi RS+\pi}^{\downarrow} \right\rangle^3 \left\langle p_{\phi RS}^{\uparrow} \right\rangle} \right.$$

$$\left. + N_{\phi RS+\pi}^{\uparrow} \frac{\left\langle \delta p_{\phi RS}^{\downarrow}{}^2 \right\rangle}{\left\langle p_{\phi RS}^{\downarrow} \right\rangle^3 \left\langle p_{\phi RS+\pi}^{\uparrow} \right\rangle} + N_{\phi RS}^{\downarrow} \frac{\left\langle \delta p_{\phi RS+\pi}^{\uparrow}{}^2 \right\rangle}{\left\langle p_{\phi RS+\pi}^{\uparrow} \right\rangle^3 \left\langle p_{\phi RS}^{\downarrow} \right\rangle} \right] \qquad (6.25)$$

To compare this error to the statistical error, lets check to see how it scales with the number of pairs in the same way we did before. It turns out $E_{pol}^2 \sim \frac{1}{p^2 N} \frac{\delta p^2}{p^2}$. In other words the error due to the polarization uncertainty is smaller than the statistical error by a factor of $\frac{\delta p^2}{p^2}$. A typical value for this is .01. The total bin error is then

$$E = \sqrt{E_{stat}^2 + E_{pol}^2}. \qquad (6.26)$$

The difference between taking a uniform polarization for the run or the correct fill-by-fill values is negligible. This can be seen in Fig. 6.33.

89
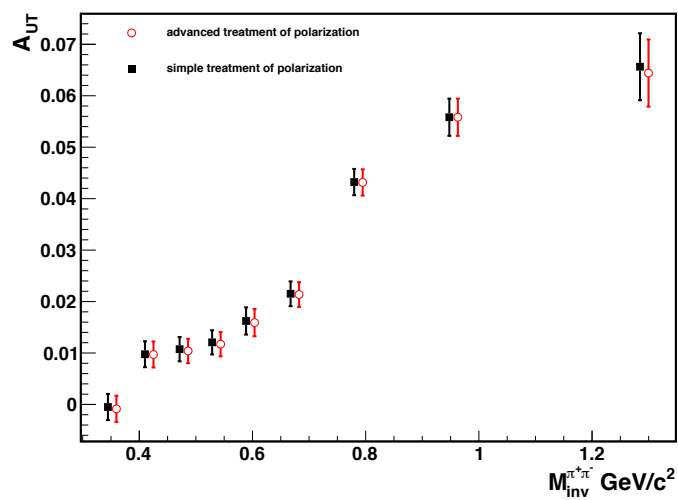
Figure 6.33: The black squares are obtained by treating the asymmetry and error as in Eqns. 6.9 and 6.10. The red circles are obtained using the advanced treatment of beam polarization in Eqns. 6.11 and 6.26. The red circles are shifted to a higher mass by 0.015 GeV/c² to avoid overlap.

CHAPTER 7

Results

7.1   One Dimensional Kinematic Binning

The first step was to recreate the results of the 2006 study shown in chapter 5. The larger data set from the 2012 run allowed for more bins in each kinematic variable. The results can be seen in figures 7.1, 7.2, and 7.3. The dependence of the asymmetry on $P_T^{\pi^+\pi^-}$ and $\eta^{\pi^+\pi^-}$ mostly agrees within errors between 2006 and 2012 analyses. The mass dependence shows the same trend but there seems to be some differences between the two years. The large errors of the 2006 data prohibit us from determining anything other than the two years to be anything other than consistent within errors.

Changing the radius changes the invariance mass, transverse momentum relationship.

$$M_{inv}^{\pi^+\pi^-} = 2P_T^{\pi^+} P_T^{\pi^-} \left[\cosh\left(\eta^{\pi^+} - \eta^{\pi^-} \right) - \cos\left(\phi^{\pi^+} - \phi^{\pi^-} \right) \right] \qquad (7.1)$$

As the difference in η and ϕ of the π^+ and π^- decreases, the quantity in the square brackets in Eqn. 7.2 also decreases. To keep the same invariant mass, the transverse momenta must increase. Examining the asymmetry in the same invariant mass bins across several different cone radii, we expect the smaller radii to have a larger average transverse momentum. As we have seen previously, a larger transverse momentum corresponds to an increased asymmetry. Therefore a smaller radius should result in a larger asymmetry for each invariant mass. This can be seen in Fig. 7.5. This gives us a hint at how the IFF and transversity
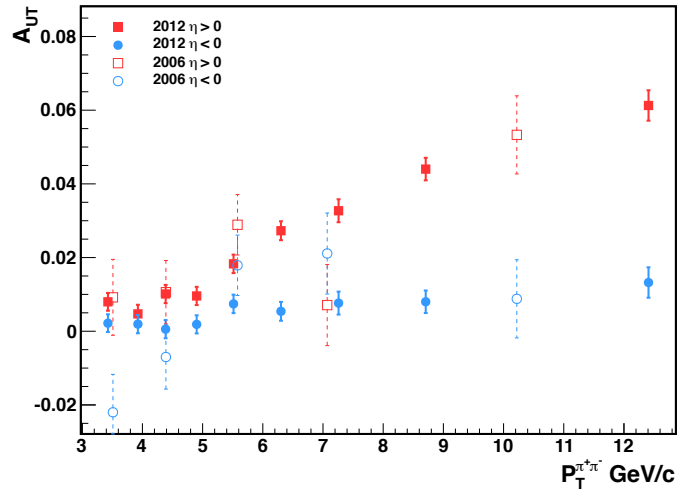
Figure 7.1: Comparison of $P_T^{\pi^+\pi^-}$ Asymmetries from 2012 and 2006
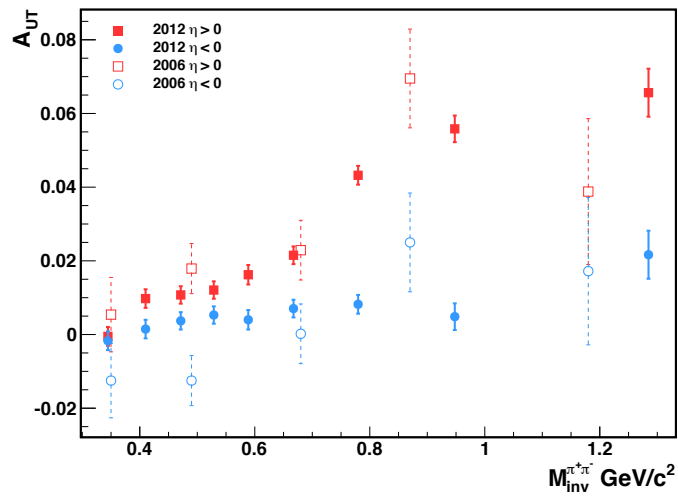
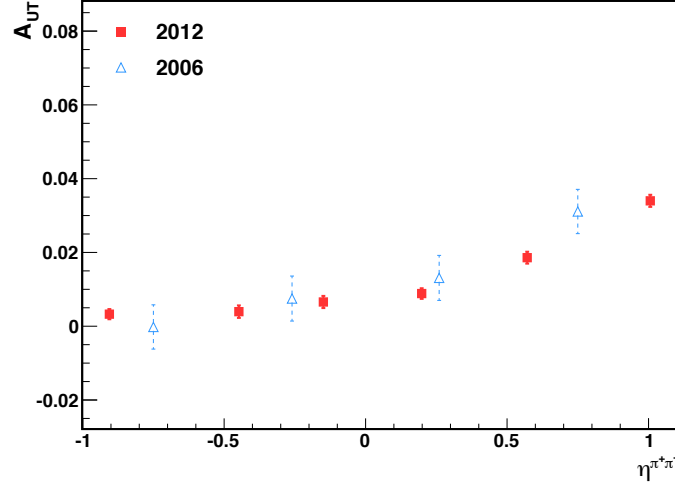Figure 7.2: Comparison of $M_{inv}^{\pi^+\pi^-}$ Asymmetries from 2012 and 2006

92

Figure 7.3: Comparison of $\eta^{\pi^+\pi^-}$ Asymmetries from 2012 and 2006

depend on z. Recall that z is the fraction of fragmenting quark momentum the pion pair retains.

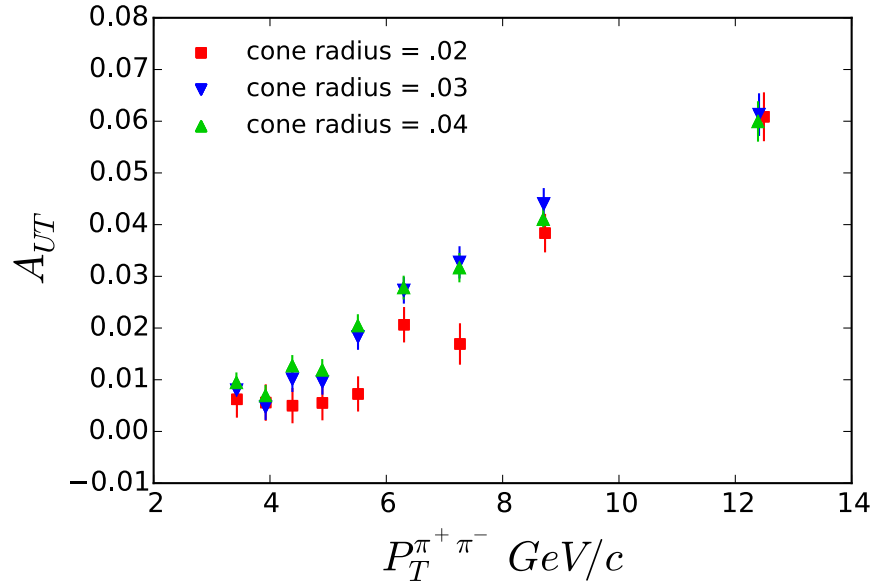$$z = \frac{\vec{P}_{\pi^+} + \vec{P}_{\pi^-}}{\vec{P}_q} \tag{7.2}$$

Figure 7.4: Asymmetry *vs* $P_T^{\pi^+\pi^-}$ for different cone radii $\eta^{\pi^+\pi^-} > 0$.
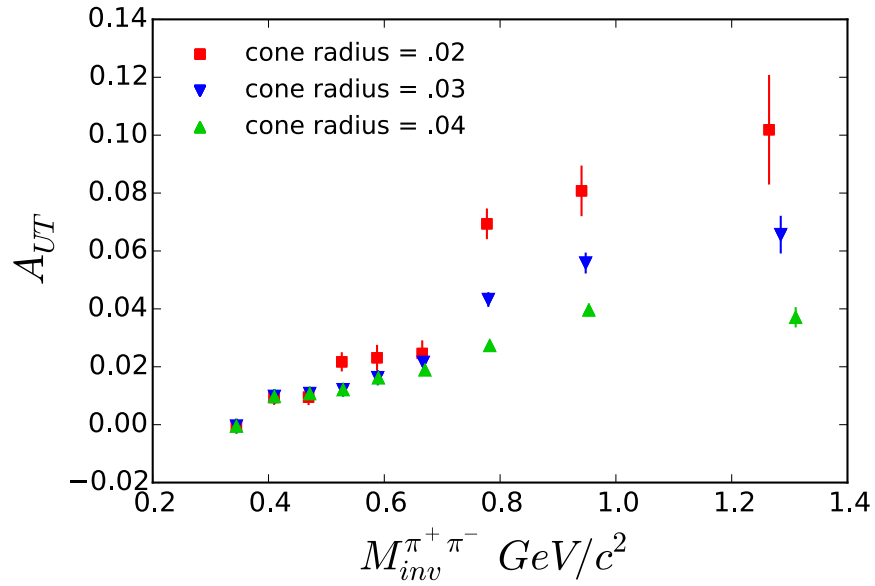
Figure 7.5: Asymmetry *vs* $M_{inv}^{\pi^+\pi^-}$ for different cone radii $\eta^{\pi^+\pi^-} > 0$.

94
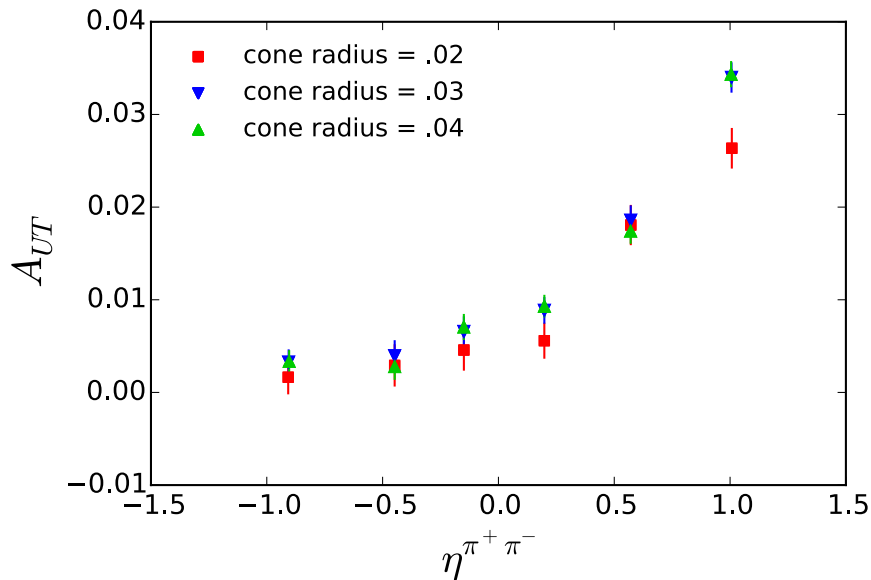
Figure 7.6: Asymmetry *vs* $\eta^{\pi^+\pi^-}$ for different cone radii.

7.2 Check for Asymmetry in Same Sign Pairs

In order to test if the asymmetry we see is due to the physics we are investigating, or some other actuation, we perform the same analysis on pion pairs of the same charge. We would expect the asymmetry to be zero for same sign pairs since the IFF only results in oppositely charge pairs due to the sequential nature of parton fragmentation. I have performed exactly the same procedure described above, except matching up same-sign pions in each event instead of opposite-sign pions. The analysis was performed over the entire pseudorapidity range. A comparison of the asymmetry of opposite-sign and same-sign pion pairs can be seen in Fig. 7.7. As expected, the asymmetry for same sign-pairs is consistent with zero. This is a good indication that our analysis for the opposite sign pairs is correct and does not contain a significant contribution from pions whose charge sign is mis-identified.
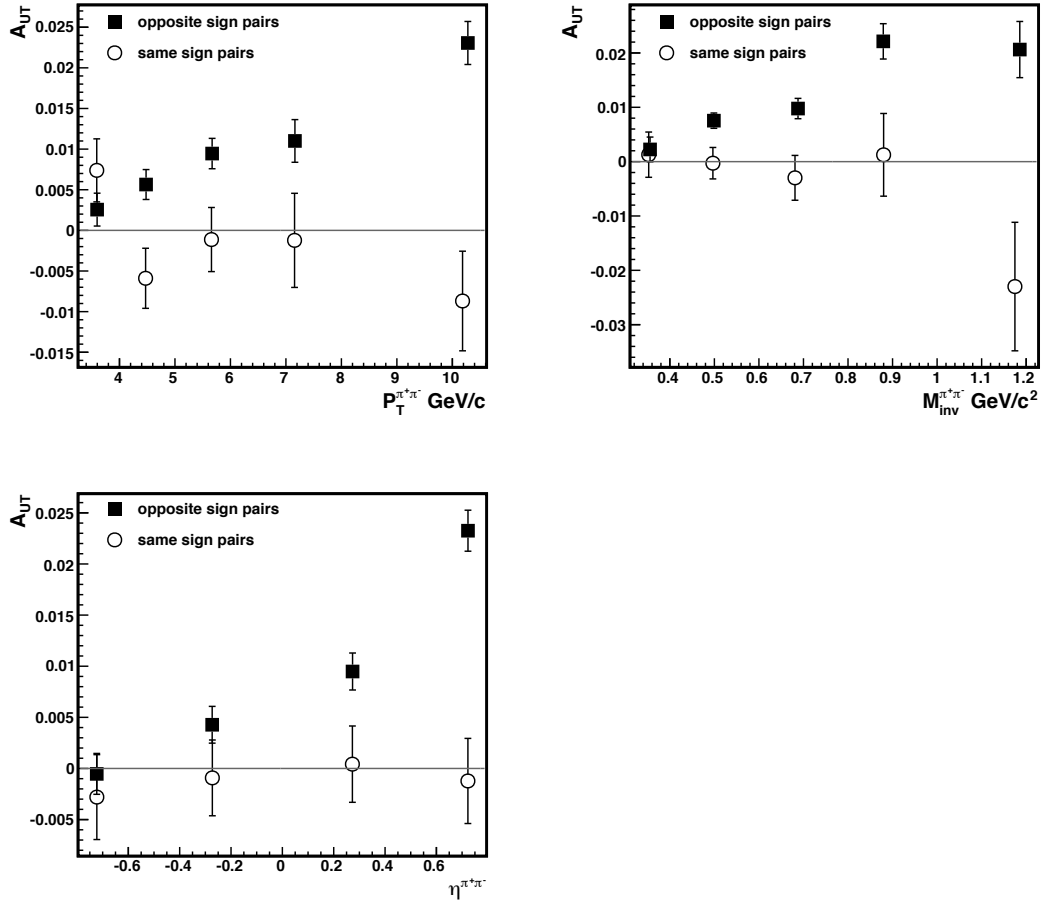
Figure 7.7: Comparison of the asymmetry in same-sign pairs and opposite-sign pairs.

7.3 Check For Other False Asymmetries

In order to make sure the asymmetries we detect are not caused by some detector factor or an error in the code, we perform checks on situations where zero asymmetry is expected. The first check is done by analyzing the same data but randomly assigning a spin state to the polarized proton. A randomly chosen spin is assigned correctly half the time and incorrectly the other half. Looking at the cross ratio formula from earlier (Eqn. 6.8) for both cases we see the asymmetry should vanish. The correct spin assignment is represented to the left of the plus sign in Eqn. 7.3, and the incorrect assignment to the right. The incorrect assignment is taken into account by the change in the spin orientation superscripts right of the plus sign in Eqn. 7.3. The two factors cancel exactly with enough statistics and should lead to zero observed asymmetry.

$$\frac{1}{2}\frac{\sqrt{N^{\uparrow}_{\phi_{RS}}N^{\downarrow}_{\phi_{RS}+\pi}}-\sqrt{N^{\downarrow}_{\phi_{RS}}N^{\uparrow}_{\phi_{RS}+\pi}}}{\sqrt{N^{\uparrow}_{\phi_{RS}}N^{\downarrow}_{\phi_{RS}+\pi}}+\sqrt{N^{\downarrow}_{\phi_{RS}}N^{\uparrow}_{\phi_{RS}+\pi}}}+\frac{1}{2}\frac{\sqrt{N^{\downarrow}_{\phi_{RS}}N^{\uparrow}_{\phi_{RS}+\pi}}-\sqrt{N^{\uparrow}_{\phi_{RS}}N^{\downarrow}_{\phi_{RS}+\pi}}}{\sqrt{N^{\downarrow}_{\phi_{RS}}N^{\uparrow}_{\phi_{RS}+\pi}}+\sqrt{N^{\uparrow}_{\phi_{RS}}N^{\downarrow}_{\phi_{RS}+\pi}}}=0$$

$$(7.3)$$

You can see in Fig. 7.8 we see no false asymmetry for random proton spin assignment.

Just as we randomly assigned the spin state of the proton, we also randomly assign the charges on the π^+, π^-. This changes the direction of $\boldsymbol{R}$.

$$\sin(\phi_R)=\frac{(\boldsymbol{P}_B\times\boldsymbol{R})\hat{\boldsymbol{P}}_h}{|\hat{\boldsymbol{P}}_h\times\boldsymbol{P}_B||\hat{\boldsymbol{P}}_h\times\boldsymbol{R}|} \tag{7.4}$$

$$\cos(\phi_R)=\frac{\hat{\boldsymbol{P}}_h\times\boldsymbol{P}_B}{|\hat{\boldsymbol{P}}_h\times\boldsymbol{P}_B|}\frac{\hat{\boldsymbol{P}}_h\times\boldsymbol{R}}{|\hat{\boldsymbol{P}}_h\times\boldsymbol{R}|} \tag{7.5}$$

By making the substitution $R \to -R$ in equations 7.4 and 7.5, it is seen that $\phi_R \to \phi_R + \pi$ (or $\phi_R \to \phi_R - \pi$ because ϕ_R is restricted to the range $-\pi$ to π).

Since R doesn't appear in the definition of $\sin(\phi_S)$ or $\cos(\phi_S)$, ϕ_S is unchanged. This leads to $\phi_{RS} \to \phi_{RS} + \pi$ (or $\phi_{RS} \to \phi_{RS} - \pi$ again because of the restriction on the values of ϕ_{RS}). Just like the random spin assignment, the random pion charge assignment will be correct half the time and incorrect the other half. By substituting $\phi_{RS} \to \phi_{RS} \pm \pi$ into the cross ratio equation 6.8 half the time, we come to an equation similar to equation 7.3 with both factors canceling.

$$\frac{1}{2} \frac{\sqrt{N^{\uparrow}_{\phi_{RS}} N^{\downarrow}_{\phi_{RS}+\pi}} - \sqrt{N^{\downarrow}_{\phi_{RS}} N^{\uparrow}_{\phi_{RS}+\pi}}}{\sqrt{N^{\uparrow}_{\phi_{RS}} N^{\downarrow}_{\phi_{RS}+\pi}} + \sqrt{N^{\downarrow}_{\phi_{RS}} N^{\uparrow}_{\phi_{RS}+\pi}}} + \frac{1}{2} \frac{\sqrt{N^{\uparrow}_{\phi_{RS}+\pi} N^{\downarrow}_{\phi_{RS}}} - \sqrt{N^{\downarrow}_{\phi_{RS}+\pi} N^{\uparrow}_{\phi_{RS}}}}{\sqrt{N^{\uparrow}_{\phi_{RS}+\pi} N^{\downarrow}_{\phi_{RS}}} + \sqrt{N^{\downarrow}_{\phi_{RS}+\pi} N^{\uparrow}_{\phi_{RS}}}} = 0$$

$$(7.6)$$

Again, as figure 7.9 shows, we detect no asymmetry from randomly assigned pion charges.
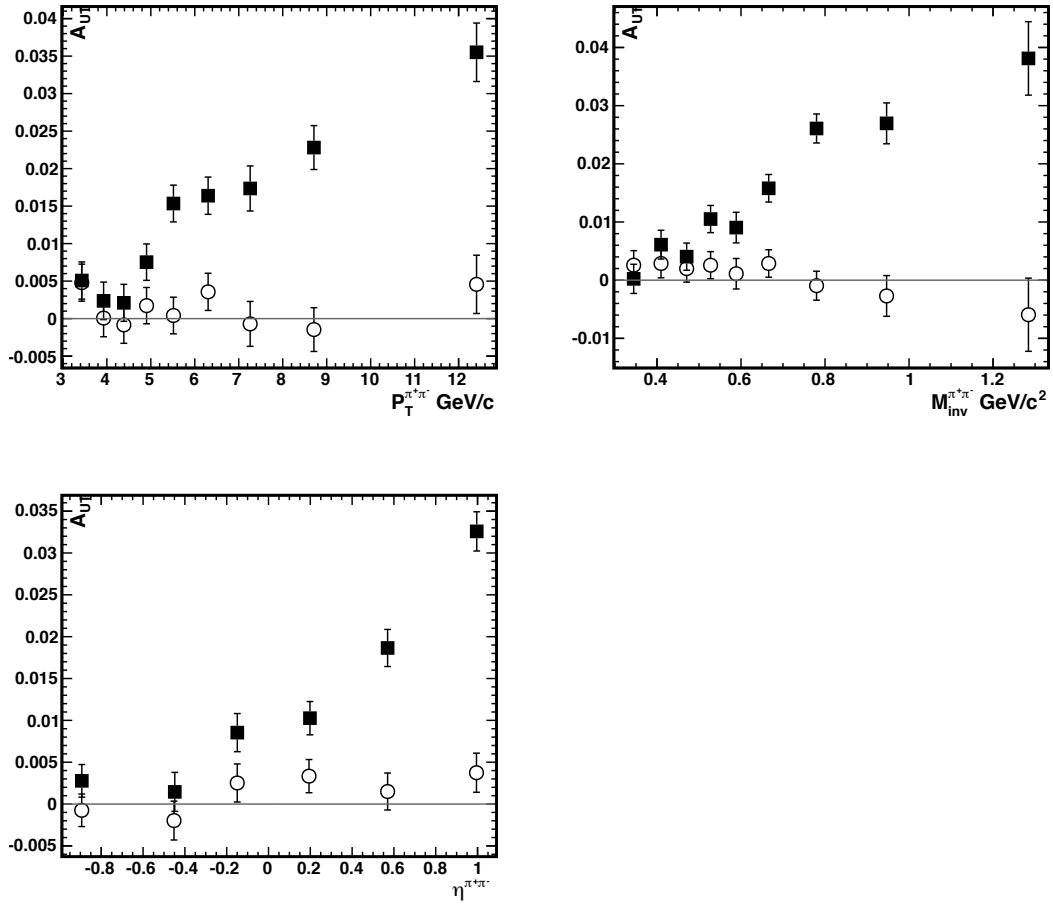
Figure 7.8: Randomly assigned spin state (open circles) show no sign of asymmety in any kinematic variable. Correct asignment (solid squares) shown for comparison. $-2 < \eta^{\pi^+\pi^-} < 2$ for $P_T^{\pi^+\pi^-}$ and $M_{inv}^{\pi^+\pi^-}$ plots.
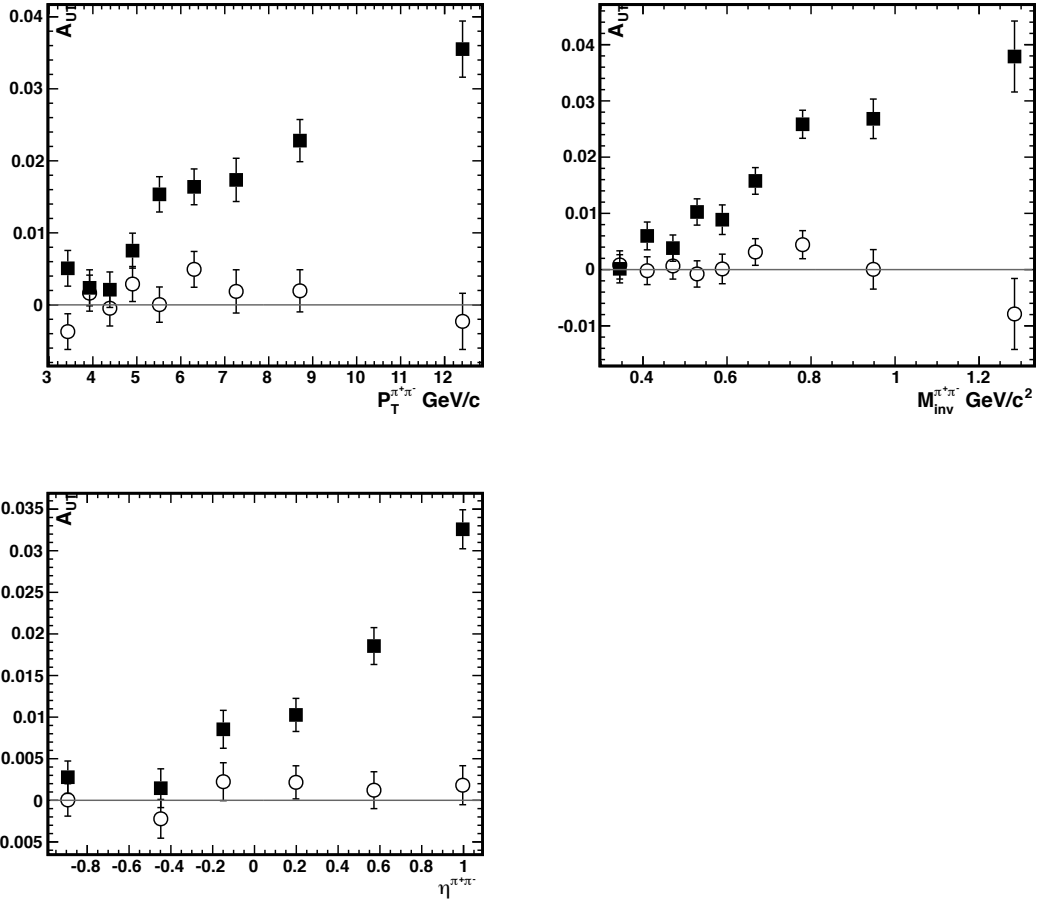
Figure 7.9: Randomly assigned pion charges (open circles) show no sign of asymmety in any kinematic variable. Correct asignment (solid squares) shown for comparison. $-2 < \eta^{\pi^+\pi^-} < 2$ for $P_T^{\pi^+\pi^-}$ and $M_{inv}^{\pi^+\pi^-}$ plots.

7.4 Two Dimensional Kinematic Binning

We have obtained a much larger data set in 2012 than 2006. This enabled us to not only divide each kinematic variable into more bins but also bin in multiple kinematic variables simultaneously. This is ideal for extracting the transversity distribution. The asymmetry is determined as a function of $M_{inv}^{\pi^+\pi^-}$ and $\eta^{\pi^+\pi^-}$ (Figs. 7.10 and 7.11), as function of $\eta^{\pi^+\pi^-}$ and $P_T^{\pi^+\pi^-}$ (Figs. 7.12 and 7.13), and as a function of $M_{inv}^{\pi^+\pi^-}$ and $P_T^{\pi^+\pi^-}$ (Figs. 7.14 and 7.15). A cone radius cut of 0.7 was used for all 2D binning measurements. There is an $\eta^{\pi^+\pi^-} > 0$ cut used when measuring the asymmetry as a function of $M_{inv}^{\pi^+\pi^-}$ and $P_T^{\pi^+\pi^-}$. Again there is an increase in the asymmetry around the ρ mass, and the highest mass bin $M_{inv}^{\pi^+\pi^-} > 1 GeV/c^2$ shows decreased asymmetry as in the 2006 analysis.
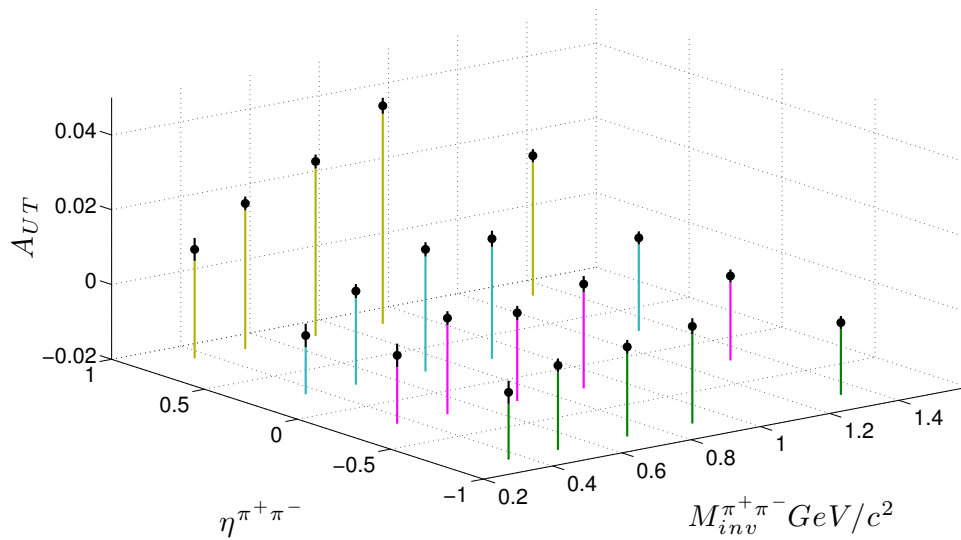
Figure 7.10: A_{UT} vs $M_{inv}^{\pi^+\pi^-}$ and $\eta^{\pi^+\pi^-}$. Different colored stands denote different $\eta^{\pi^+\pi^-}$ bins. Note: zero is suppressed in this plot.
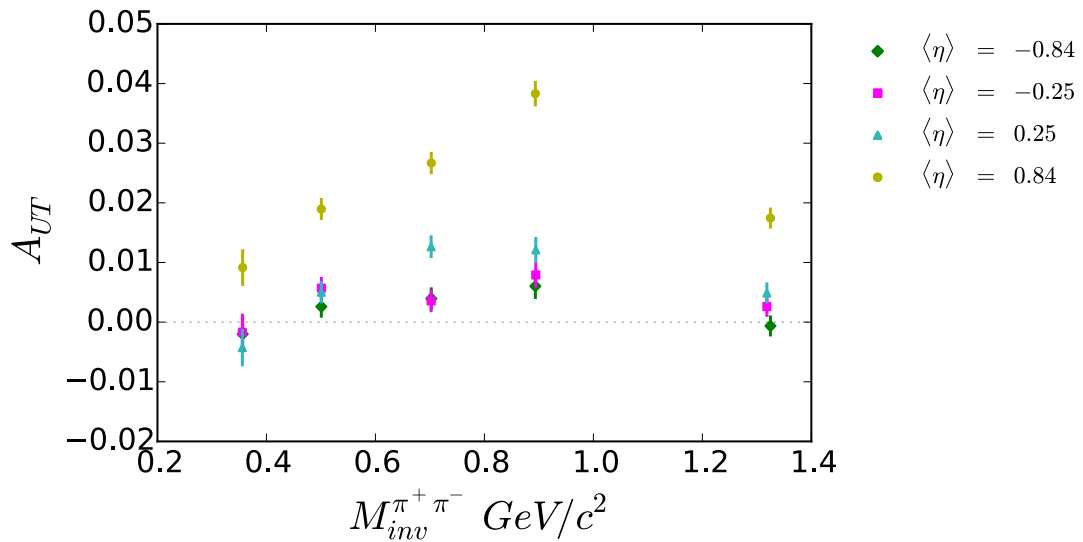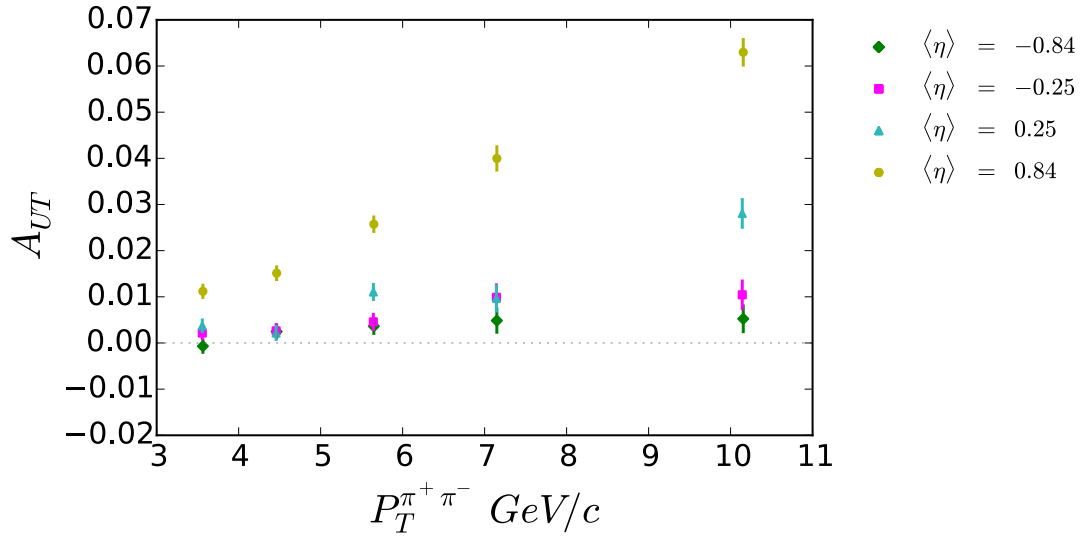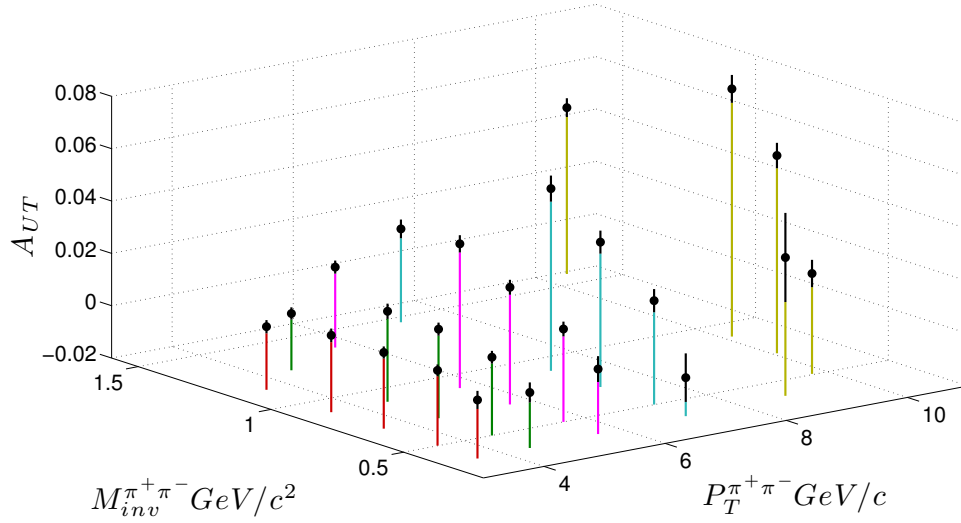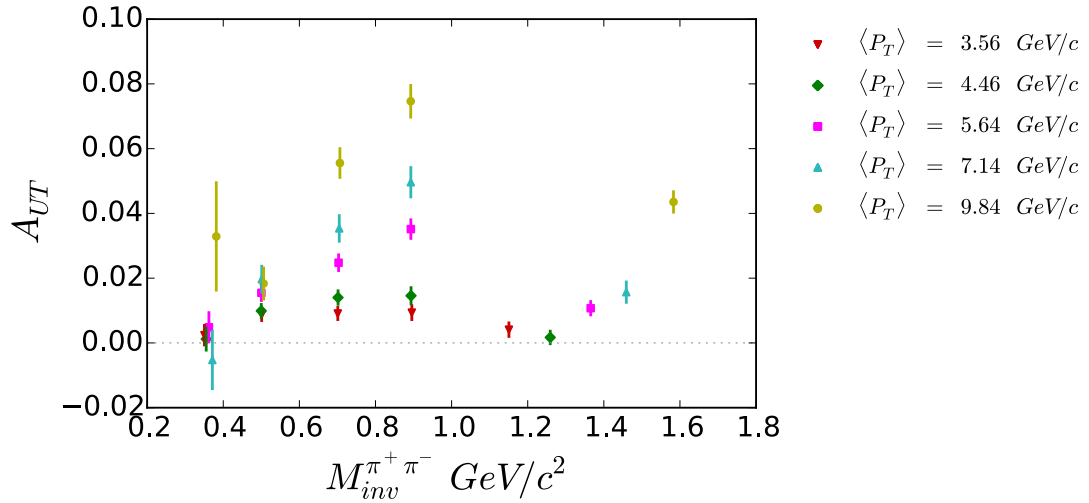

Figure 7.11: 2D view of A_{UT} vs $M_{inv}^{\pi^+\pi^-}$ for different $\eta^{\pi^+\pi^-}$
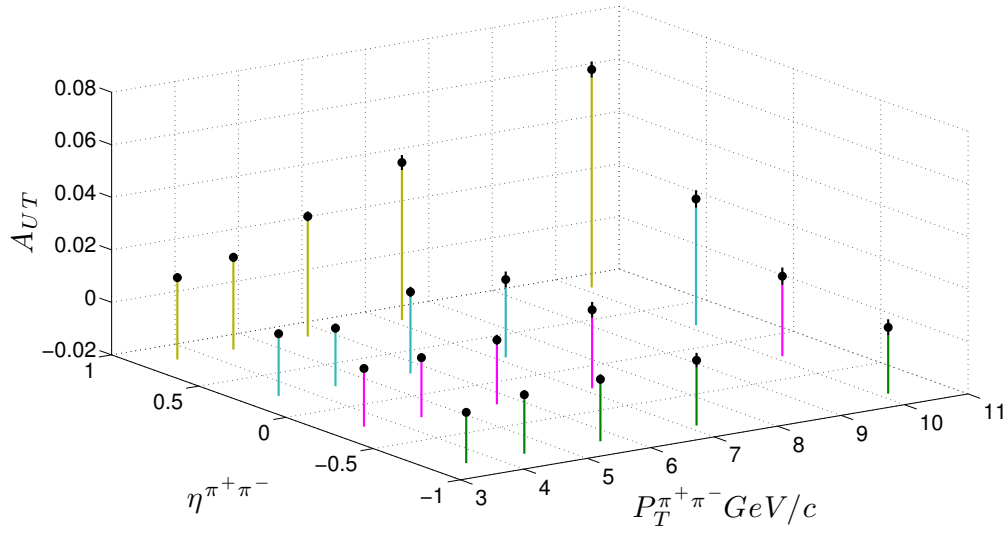
Figure 7.12: A_{UT} vs $P_T^{\pi^+\pi^-}$ and $\eta^{\pi^+\pi^-}$. Different colored stands denote different $\eta^{\pi^+\pi^-}$ bins. Note: zero is suppressed in this plot.

Figure 7.13: 2D view of A_{UT} vs $P_T^{\pi^+\pi^-}$ for different $\eta^{\pi^+\pi^-}$

Figure 7.14: A_{UT} vs $M_{inv}^{\pi^+\pi^-}$ and $P_T^{\pi^+\pi^-}$. Different colored stands denote different $P_T^{\pi^+\pi^-}$ bins. Note: zero is suppressed in this plot. $(\eta^{\pi^+\pi^-} > 0)$

Figure 7.15: 2D view of A_{UT} vs $M_{inv}^{\pi^+\pi^-}$ for different $P_T^{\pi^+\pi^-}$, $\eta^{\pi^+\pi^-} > 0$

7.5 Asymmetry with partial wave expansion

As stated in chapter 4, the cross section for the scattering process can be expanded.

$$\sin\theta H_1^{\triangleleft c}(\bar{z}_c, \cos\theta, M_{inv}^{\pi^+\pi^-2}) \approx H_{1,ot}^{\triangleleft c}(\bar{z}_c, M_{inv}^{\pi^+\pi^-2})\sin\theta$$
$$+ H_{1,lt}^{\triangleleft c}(\bar{z}_c, M_{inv}^{\pi^+\pi^-2})\sin\theta\cos\theta \qquad (7.7)$$

Starting from 6.2, one can come up with a relationship for the yield of pion pairs from spin up and spin down after the expansion. This time the polarization is encapsulated in the asymmetry coefficients A_{sp} and A_{pp}.

$$N^\uparrow = L^\uparrow\left[1 + \sin(\theta)\left(A_{sp} + A_{pp}\cos(\theta)\right)\sin(\phi_{RS})\right] \qquad (7.8)$$

$$N^\downarrow = L^\downarrow\left[1 - \sin(\theta)\left(A_{sp} + A_{pp}\cos(\theta)\right)\sin(\phi_{RS})\right] \qquad (7.9)$$

The data was separated into two different sets, one for spin up collisions and one for spin down, and fit simultaneously with the corresponding yield relationship using an unbinned maximum likelihood fit. The luminosity values and asymmetry coefficients are both determined from the fit. As a cross-check, the number of pairs from up and down were counted separately and compared to the luminosity values determined from the fit. These were always consistent. A histogram of the data in ϕ_{RS} and θ is shown in Fig. 7.16a, and an example of with the unbinned maximum likelihood fit can be seen in Fig. 7.16b.

The fitting procedure was done for pairs in the forward direction ($\eta > 0$) in the same invariant mass and transverse momentum bins as the previous section, and the results are shown below. Since the polarization was folded into the asymmetry coefficients in the fit the values here must be scaled by 1/polarization in order to make a fair comparison to the values shown in the previous section. The average
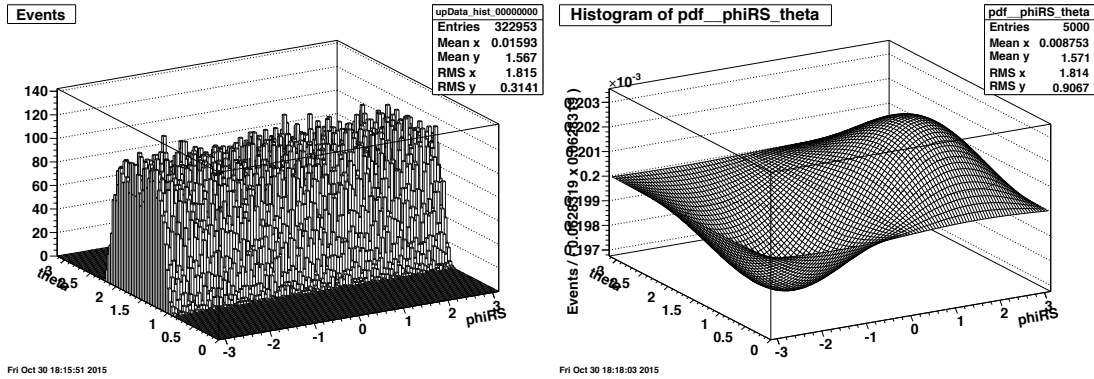
(a) Histogram of $N^{\uparrow}$

(b) Maximum Likelyhood Fit

Figure 7.16: Data and unbinned maximum likilihood fit

polarization for data analyzed is 61.6%. This puts the black points in Fig. 7.17 very close to the values seen in the original two dimensional analysis. This makes sense because if θ is integrated over, as was the case in the previous 2D binning, only A_{sp} would survive. The red points corresponding to the A_{pp} coefficient are consistent with zero, and have no noticeable trend. If one looks hard enough, the sign of A_{pp} seems to be positive at lower invariant mass and negative at higher invariant mass, the change coming at the ρ mass. However the size of the error bars make this not significant.
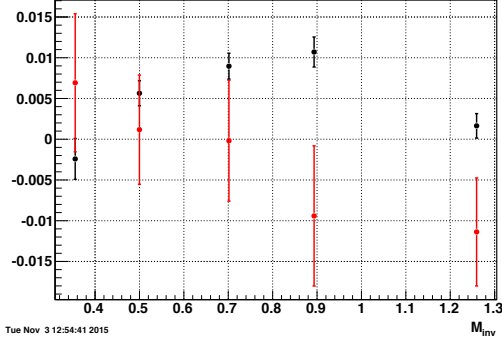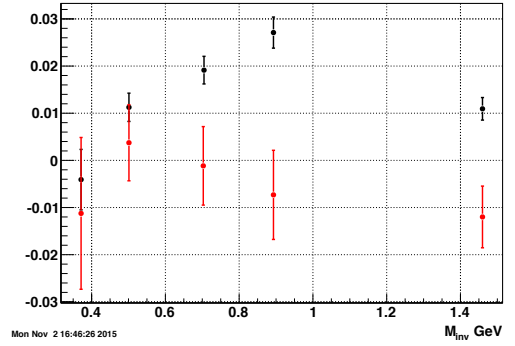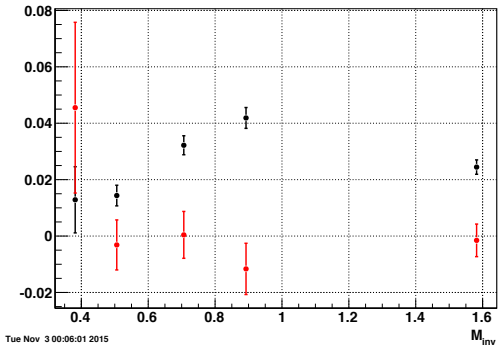
(a) $0.0 \leq P_T^{\pi^+\pi^-} < 0.4$
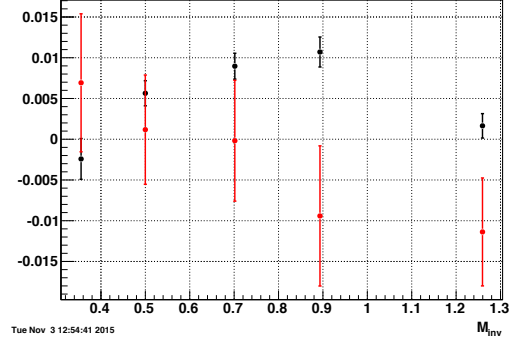
(b) $0.4 \leq P_T^{\pi^+\pi^-} < 0.6$
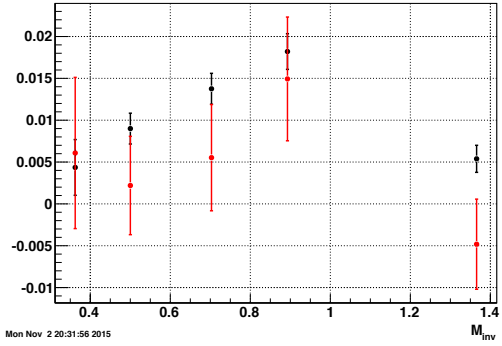
(c) $0.6 \leq P_T^{\pi^+\pi^-} < 0.8$

(d) $0.8 \leq P_T^{\pi^+\pi^-} < 01.0$

(e) $1.0 \leq P_T^{\pi^+\pi^-}$

Figure 7.17: A_{sp} (black) and A_{pp} (red) vs invariant mass for different $P_T^{\pi^+\pi^-}$ ranges for pion pairs scattered into the forward ($\eta > 0$) direction

7.6 Kaon Pion Pairs

We can perform a similar analysis for other dihadron pairs. In this section, we focus on kaon-pion pairs. Since Kπ pairs go through an intermediate vector meson K*(892) the IFF for the fragmentation of a transversely polarized quark into a kaon and a pion, and therefore observed asymmetry, should be enhanced in this range just like in the ρ mass range for $\pi^+\pi^-$ pairs [29].

In the $\pi^+\pi^-$ pair analysis the identification of pions was relatively simple and unimportant because there are so many more pions than kaons or protons. We attempt to cut as many kaons and protons out as possible and the rest just come as a dilution to the pion sample. It is a lot more difficult to look specifically for kaons. To do this we have to use the ToF as well as the ionization energy loss in the TPC to distinguish between pions and kaons accurately. Figure 7.18 shows a heat map of the particle mass determined by the ToF vs the track $n_\sigma(\pi)$ determined by the ionization energy loss. This is separated into 11 different track momentum ranges. Looking at the first momentum range in the upper left hand plot, the protons are seen as the faint green region at an time of flight mass of just under one GeV/c^2. As expected the pions are located around the bright red region at centered at $n_\sigma(\pi) = 0$. The kaons are the faint green region just above and to the left of the pion region. Since protons are so far away from kaons and pions, they are easily removed from the sample with a ToF mass cut. However in order to correctly identify kaons, we need to make a distinction between them and pions.

Looking at each momentum bin individually I constructed the interface between the pion region and the kaon region. I then removed the overlap region where it is impossible to distinguish pions and kaons. This can be seen for the lowest momentum bin in Fig. 7.19. Everything between the white lines is not included in the analysis. Particles above the top line is taken to be a kaon, except
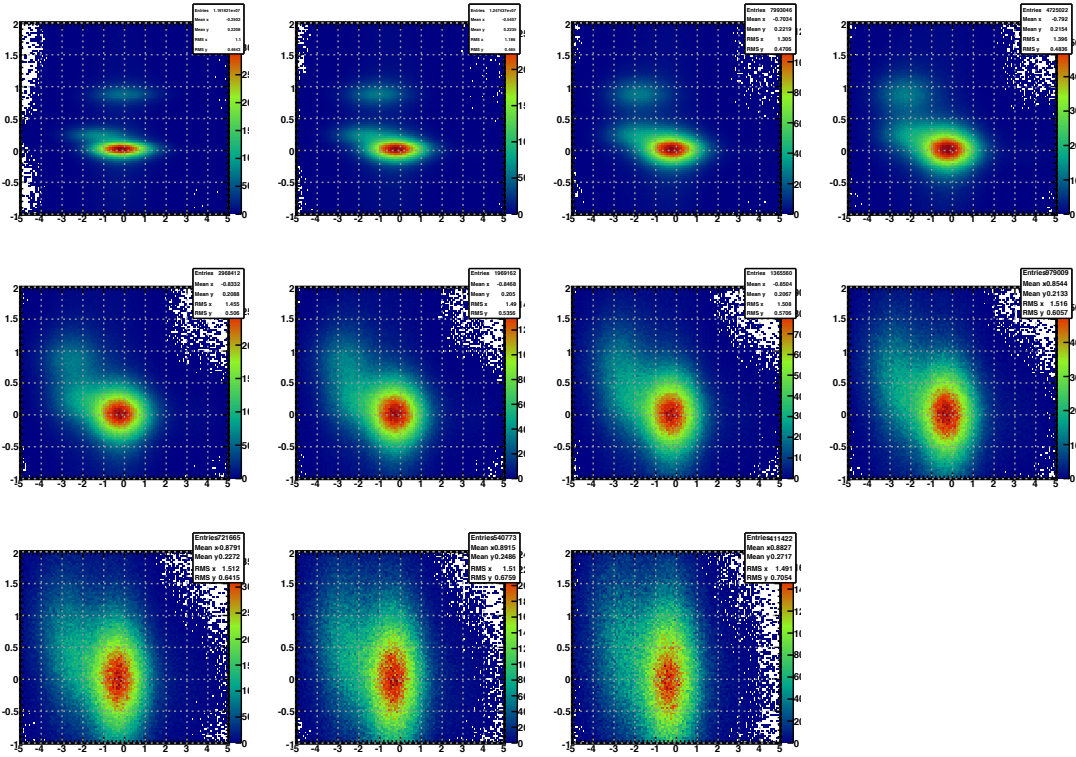
Figure 7.18: 2D histograms of mass determined from ToF vs $n_\sigma(\pi)$ for differnet track momenta

for the clear proton region which is removed by a horizontal ToF mass cut. Everything below the bottom line is declared a pion. I was able to do this method with varying success for the first four momentum bins. The bin limits can be seen in table 7.1. The pion, kaon, and sometimes even proton regions in the remaining bins overlapped too much and were not included in the analysis. As the track momentum increases the exclusion region between the white lines increases.

Once $K\pi$ pairs are found, the analysis continues as in the $\pi^+\pi^-$ pair case, however with much lower statistics. Figure 7.20 shows the asymmetry vs the invariant mass of the $K\pi$ pair for $\eta^{K\pi} > 0$. The lower limit on invariant mass in now 633.25 MeV/c^2 and the invariant mass bins are changed accordingly. The low statistics only allow for three invariant mass bins. More bins result in huge
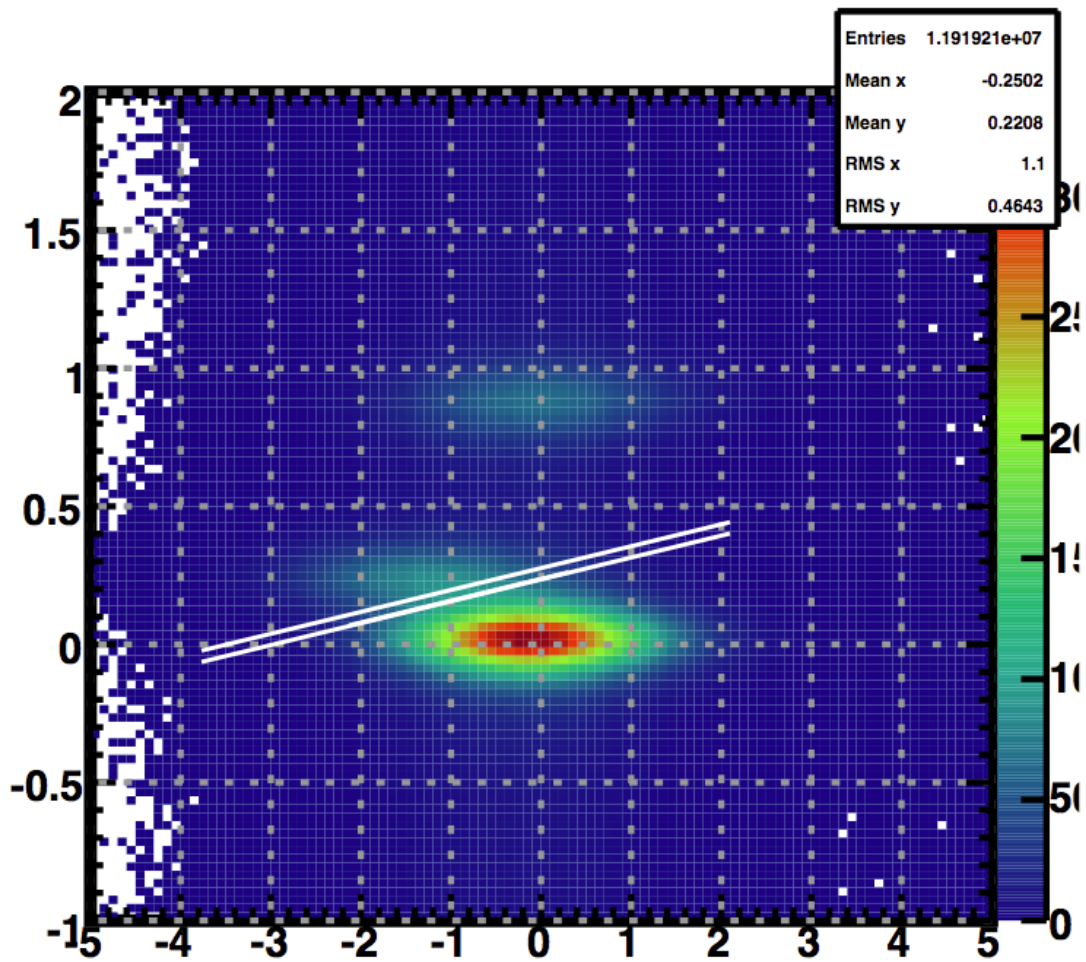
109

Figure 7.19: Separation of kaons and pions. Tracks between the white lines are discarded.

Table 7.1: Track momentum bins for Kπ analysis

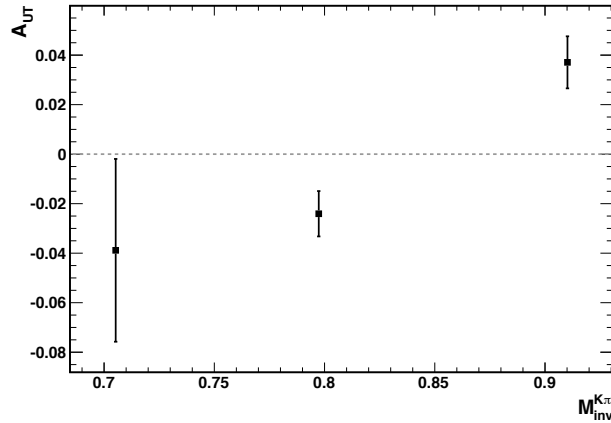| momentum bin	momentum range (GeV)
1	1.5 - 1.9
2	1.9 - 2.3
3	2.3 - 2.7
4	2.7 - 3.1

Figure 7.20: Asymmetry vs Invariant Mass for Kaon Pion Pairs. Nonzero asymmetry is only seen in the mass bin containing the K*(892) mass. $\eta^{K\pi} > 0$

error bars in the largest bin. Just like the $\pi^+\pi^-$ pair scenario, we expect an enhancement to the asymmetry in the vicinity of K^* mass (892 MeV/c^2). As shown in Fig. 7.20, we do see an enhancement in this mass region, however we also see a sizable negative asymmetry in the mass region directly before it. It is possible that the asymmetry near the K^* mass may just be do to statistical fluctuations and our low statistics. More investigation is needed to make a clear statement.

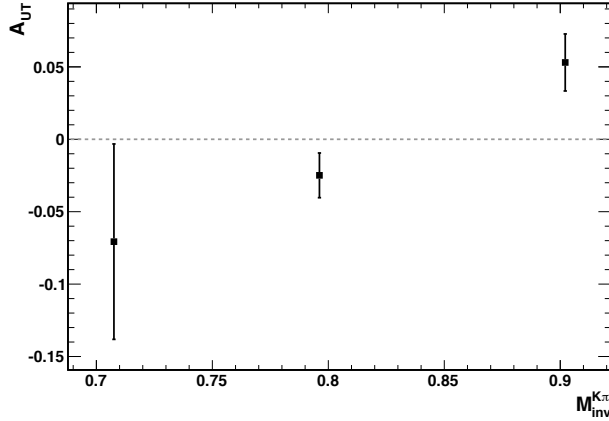We know from the $\pi^+\pi^-$ pair case that the asymmetry should increase with

Figure 7.21: Asymmetry *vs* Invariant Mass for Kaon Pion Pairs. Nonzero asymmetry is only seen in the mass bin containing the K*(892) mass. $\eta^{K\pi} > 0.50$

the pseudorapidity of the pair. In Fig. 7.20 we had a lower $\eta^{K\pi}$ limit of 0. If we increased the lower limit, we should see an increase in the asymmetry. Seeing an increase in the asymmetry near the K^* could be evidence that the asymmetry is real and not a product of statistical fluctuations. The asymmetry when $\eta^{K\pi} > 0.5$ can be seen in Fig. 7.21.

The third mass bin has an asymmetry of 0.0530 ± 0.0197 when the lower $\eta^{K\pi}$ limit is 0.5 and 0.0371 ± 0.0105 when the lower $\eta^{K\pi}$ limit is 0. This suggests the asymmetry in this bin could be physical. Not only that but the asymmetry in the second bin has decreased when the lower $\eta^{K\pi}$ limit was changed to 0.5.

In the $\pi^+\pi^-$ analysis, the pions were ordered by electric charge; the positive pion always chosen to be hadron 1 in the calculation of the vector $\boldsymbol{R}$ (refer to chapter 4). In the $K\pi$ analysis, it is not so clear. The two particles could be ordered by charge or by particle type. As a check, the asymmetry was determined in $K^+\pi^-$ and $K^-\pi^+$ pairs separately when using charge ordering. This can be seen in Fig. 7.22. With the exception of the lowest mass bin, which is hindered by low statistics, the asymmetry is equivalent between $K^+\pi^-$ and $K^-\pi^+$ pairs.
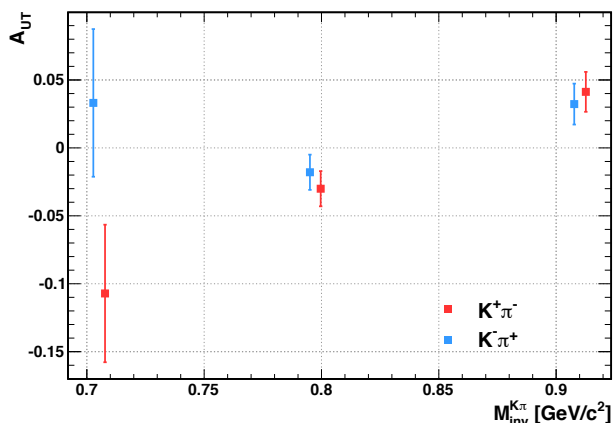
Figure 7.22: Asymmetry *vs* Invariant Mass for different charge cobininations of Kaon Pion Pairs. $\eta^{K\pi} > 0$

As with the pion pair analysis, I would like to explore the effect of the radius cut on the asymmetry. Since there is only one invariant mass bin with a significant asymmetry, I look at the asymmetry in this bin for different radii. In the pion analysis, the smallest radius cut (0.2) resulted in the highest observed asymmetries. In the $K\pi$ analysis, this same radius cut results in zero observed asymmetry. To investigate this more deeply, I measured the asymmetry at the same three values which were used in the pion analysis (0.2, 0.3, 0.4), as well as other intermediate values of the radius cut. The results are shown in Fig. 7.23. As in the pion analysis, the asymmetry decreases with increasing radius cut, with the exception of the smallest cuts. Since only three radii were used in the pion analysis, it is not clear whether a decrease in asymmetry would have been seen at lower radii. This may be something to investigate, as it could give insight into very low z behavior of the IFF.

Unfortunately, this is all we could have done so for $K\pi$ pairs. The statistics are so sparse that we cannot do a multivariable analysis as we did for $\pi^+\pi^-$ pairs. Since the only nonzero asymmetry we see is in the vicinity of K^* integrating over
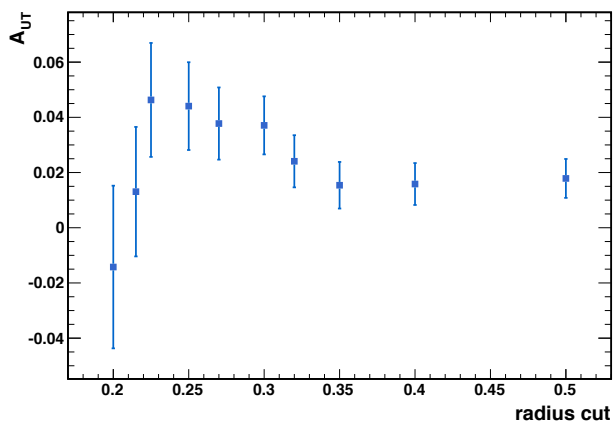
Figure 7.23: Asymmetry *vs* radius cut for the highest invariant mass bin. $\eta^{K\pi} > 0$

the invariant mass washes out any asymmetry we see. Thus investigating how the asymmetry behaves with $P_T^{K\pi}$ or $\eta^{K\pi}$ when the invariant mass is integrated over results in zero asymmetry. With more statistics it would be interesting to look at how varying the transverse momentum affects the asymmetry near K^*.

CHAPTER 8

Comparison with Theoretical Calculations

With the IFF extracted from electron positron annihilation at BELLE (see 2.6) half the puzzle is complete. Once the IFF is known, the transversity distribution can be extracted, also using the replica method [10] described in Sec. 2.6, from the observed asymmetry in di-hadron lepto-production [37]. Combining the results of the extraction of the IFF and the transversity distribution, Radici et. al. made predictions for the observed asymmetry in hadron collisions [35] by replacing the IFF and the transversity distribution in

$$
A_{UT} = 2 P_T^{\pi^+\pi^-} \sum_{a,b,c,d} \frac{|\boldsymbol{R}|}{M_{inv}^{\pi^+\pi^-}} \int \frac{dx_a dx_b}{16\pi z_c} f_1(x_a) h_1(x_b) \frac{d\Delta\hat{\sigma}_{ab^\uparrow \to c^\uparrow d}}{d\hat{t}} H_1^{\triangleleft c}\left(\bar{z}_c, M_{inv}^{\pi^+\pi^- 2}\right)
$$

$$(8.1)$$

with the extracted replica. These replicas are first evolved to the STAR transverse momentum scale using the DGLAP evolution equations [35].

8.1   Comparison for 2006 data

Predictions for A_{UT} as a function of invariant mass of the $\pi^+\pi^-$ pair are shown in Fig. 8.1. The grey band corresponds to the predicted value of 68% of the replicas. It is superimposed behind the data points shown in Fig. 5.1 for $\eta > 0$. The 68% replica band does well to predict the data. The prediction for A_{UT} as a function of $\eta^{\pi^+\pi^-}$ can be seen in Fig. 8.2. The convention used is opposite to the one used in this thesis - the direction of the polarized beam is taken to be in
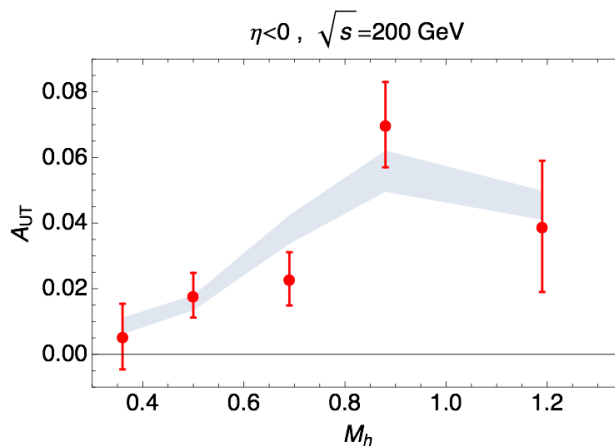
Figure 8.1: Comparison of theoretically calculated asymmetry and 2006 experimental result versus pion pair invariant mass for forward pairs. The grey The uncertainty band corresponds to the 68% of all replicas.

the negative η direction. The 68% replica band does not do as well to predict the results especially in the most forward direction. Three replicas (6, 31, and 43) are shown that fall outside the 68% replica band but predict the result with more accuracy.
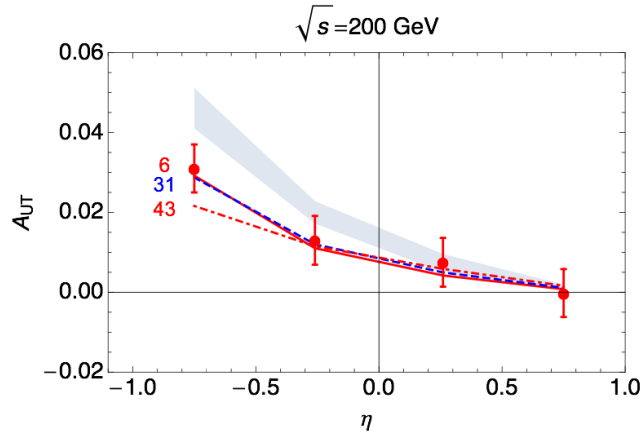
Figure 8.2: Comparison of theoretically calculated asymmetry and 2006 experimental result versus pion pair pseudorapidity.

8.2 Comparison for 2012 data

The predictions for 2012 are done in the same manner as for 2006. With more data from the 2012 production, these predictions can be put to better test. Figure 8.3 shows the prediction values of A_{UT} as a function of $\eta^{\pi^+\pi^-}$ and the 2012 data points shown in Fig. 7.3. This time the predicted 68% replica band perfectly matches the data. In Fig. 8.4, the prediction for A_{UT} is shown as a function of $M_{inv}^{\pi^+\pi^-}$ along with the 2012 data for $\pi^+\pi^-$ pairs in the direction of the polarized beam ($\eta^{\pi^+\pi^-} < 0$, in the convention of the authors). There is a slight discrepancy between the prediction and the 2012 data at larger $M_{inv}^{\pi^+\pi^-}$. There is also one data point from 2012 at higher $M_{inv}^{\pi^+\pi^-}$ that has been left off. This data point, which can be see in Fig. 7.2 at $M_{inv}^{\pi^+\pi^-} > 1.2$, would disagree with the prediction even further. Figure 8.5 shows the prediction for pairs in the backwards direction from the polarized beam. Here the calculations do a better job. The accuracy seen in these calculations, although not excellent, hints at the universality of the transversity distribution function.
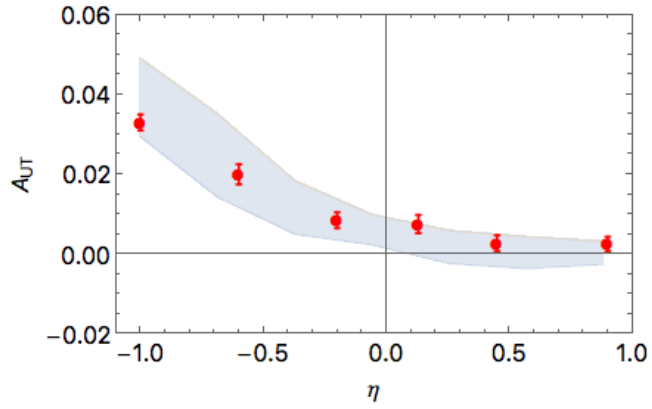
Figure 8.3: Comparison of theoretically calculated asymmetry and 2012 experimental result versus pion pair pseudorapidity
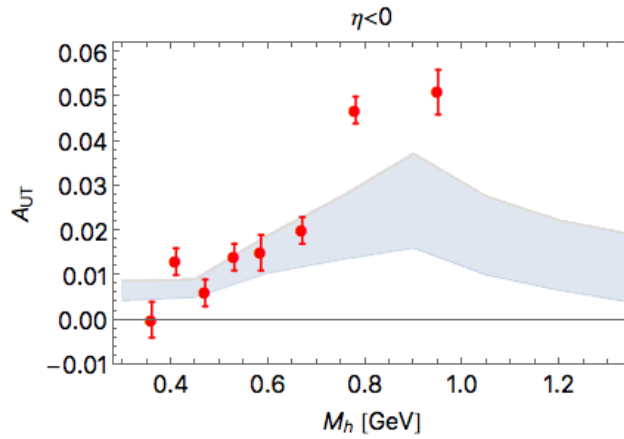

Figure 8.4: Comparison of theoretically calculated asymmetry and 2012 experimental result versus pion pair invariant mass for forward pairs.
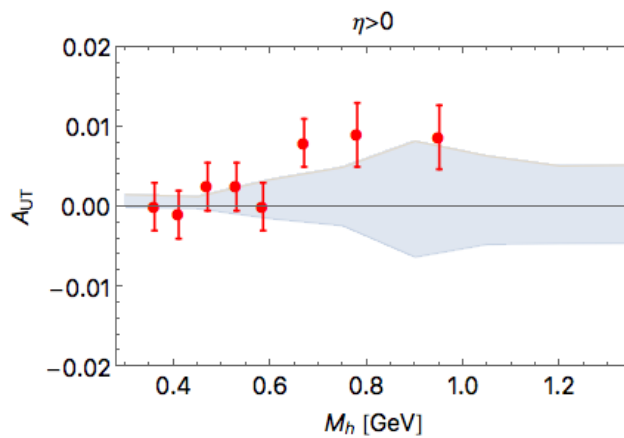
Figure 8.5: Comparison of theoretically calculated asymmetry and 2012 experimental result versus pion pair invariant mass for backward pairs.

CHAPTER 9

Discussion

The goal of this thesis was to measure the spin dependent asymmetry in the production of pion pairs. This was done differentially in $M_{inv}^{\pi^+\pi^-}$, $P_T^{\pi^+\pi^-}$, and $\eta^{\pi^+\pi^-}$. The possibility of this asymmetry in kaon-pion pairs was also investigated. In the near future, the transversity distribution will be extracted from a global fit of the STAR data presented here as well as the 500 GeV analysis by Mike Skoby in conjunction with the HERMES/COMPASS data [35]. This should give us the best understanding of the transversity distribution to date. At that point the universality of the transversity distribution as well as the Q^2 evolution of the transversity distribution can be investigated. In the following appendix, I present a supplemental analysis on simulated data to aid in the comparison of the asymmetries measured here and theorists lattice calculations of the asymmetry.

APPENDIX A

Pythia Tune Selection

Typically additional information is needed to frame experimental results which are not accessible experimentally. For this purpose we use embedding with events generated by Pythia and detector simulation with Geant. This year, much work was done by Kevin Adkins (University of Kentucky) to select Pythia settings in such a way that the simulated events reflect the actual data as well as possible.

The first step was selecting which Pythia tune produced particle yields most comparable to the STAR data. A total of five tunes were investigated. Figure A.1 shows the ratio of π^+ yields in simulation to real data as a function of transverse momentum. Perugia 0 seems to be the worst fit out of all the tunes. The only Pythia tune to match at low p_T is CDF Tune A which doesn't match for higher p_T. Perugia 2012 seems to be the best fit overall even though the it doesn't match at low p_T.

One idea is to decrease the value of the primordial k_T in Perugia 0 which has a high default k_T value at 2 GeV/c. This parameter accounts for the infrared effects [40]. The quality of the Perugia 0 is drastically increased when changing this parameter from 2 GeV/c to 0.5 GeV/c as seen in Fig. A.2. It seems as though this corrected disagreement at low p_T as caused Perugia 0 to be satisfactory fit at higher p_T as well. In fact, it worked so well that the primordial k_T was decreased to 0.5 GeV/c in Perugia 2012 and Perugia 6 as well. As with Perugia 0, low p_T yields for Perugia 2012 are also improved with the change in primordial k_T, as seen in Fig. A.3. It is possible that, although it corrects particle yields, altering
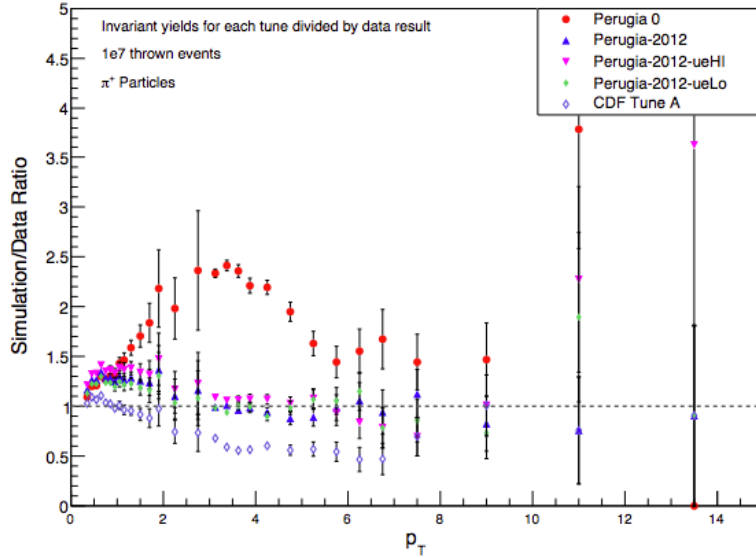
Figure A.1: Ratio of simulated pion yield to real data pion yield for five different Pythia tunes as a function of pion transverse momentum.

the default primordial k_T value could have adverse effects on different properties of the data. Because of this we want to keep in mind the Pythia tune which performs best at nominal k_T. This seems to be Perugia 2012 as seen in Fig. A.1.

With two possible tunes in hand we investigate the effect of our choice of parton distribution function set. Figure A.4 shows the π^+ yield ratio for default PDF sets for nominal k_T and for reduced k_T. By comparing the yield ratio of the default PDF set to other we find the most suitable PDF set to be NNPDF 3.0 Lo for nominal k_T Perugia 2012 shown in figure A.5, and CT10 for reduced k_T and Perugia 0 shown in figure A.6

The best two candidates are Perugia 0 with PDF set CT10 and reduced k_T and Perugia 2012 with PDF set NNPDF 2.0 Lo and nominal k_T. The next thing to look at is if each generates jets with subprocess fractions similar to NLO Theory calculations. Figure A.7 shows how the Pythia subprocess fractions compare to NLO theoretical curves for both candidates. It is clearly seen that Perugia 0
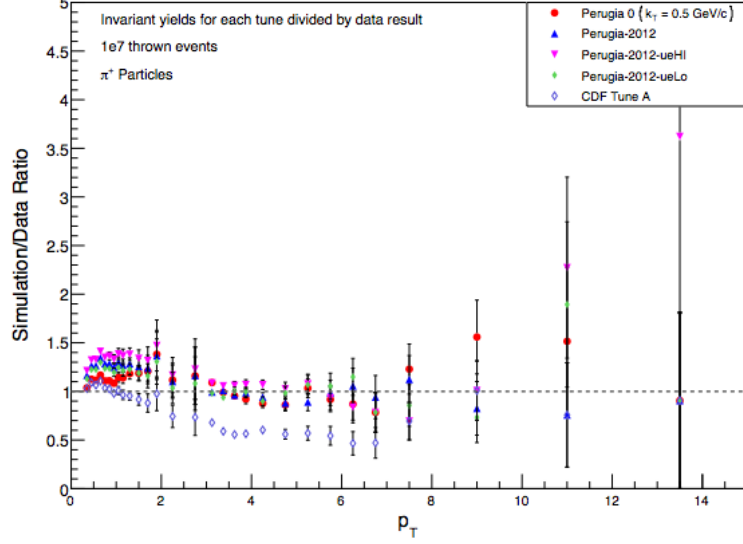
Figure A.2: Ratio of simulated pion yield to real data pion yield for five different Pythia tunes as a function of pion transverse momentum with reduced k_T for Perugia 0.
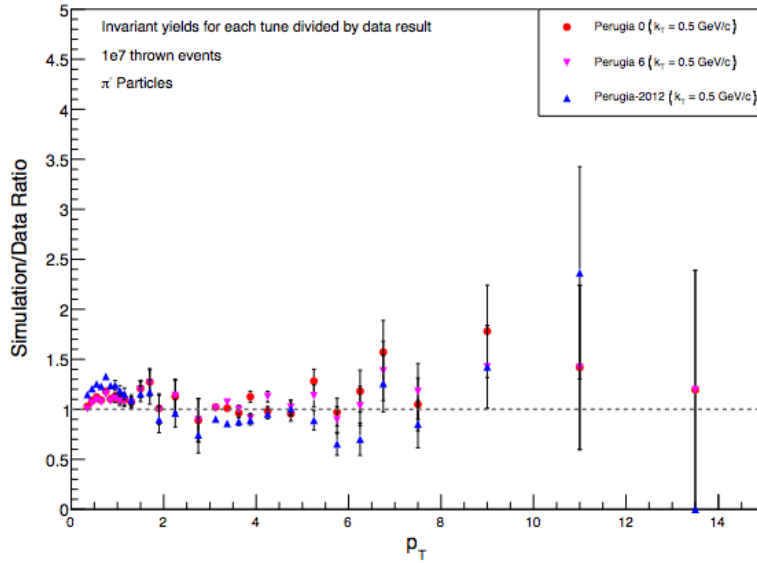

Figure A.3: Ratio of simulated pion yield to real data pion yield for best three Pythia tunes as a function of pion transverse momentum all with reduced k_T.
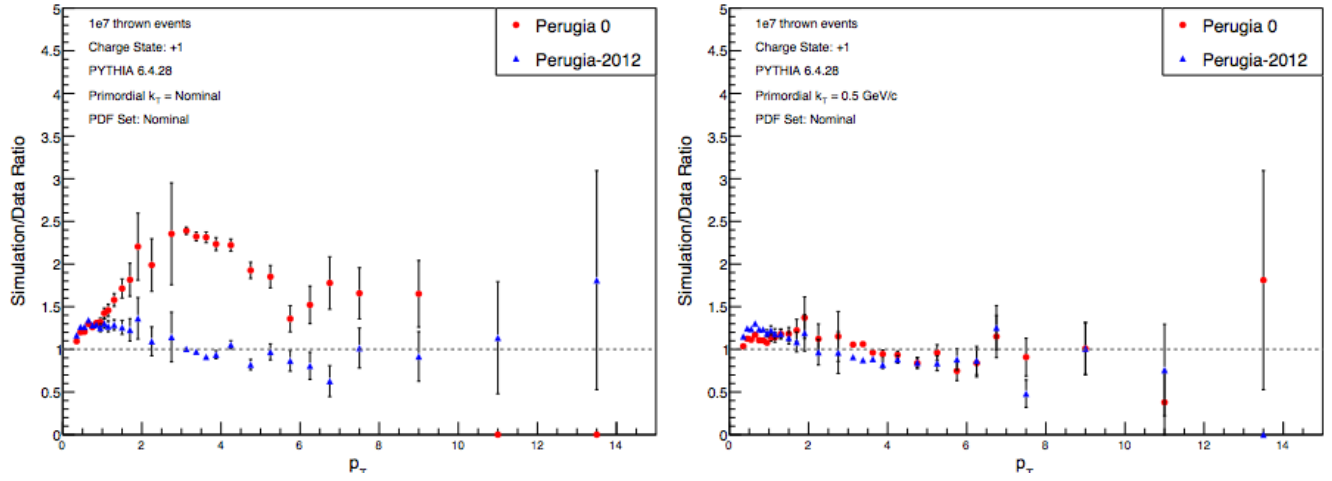
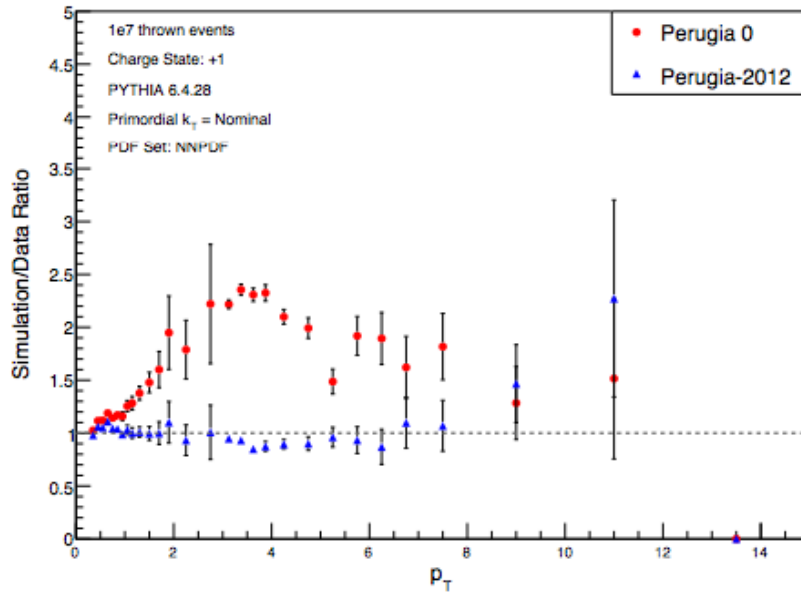Figure A.4: Pion yield ratios for Perugia 0 and Perugia 2012 for nominal k_T and reduced k_T.

Figure A.5: The best PDF set for Perugia 2012 and nominal k_T is NNPDF 3.0 Lo.
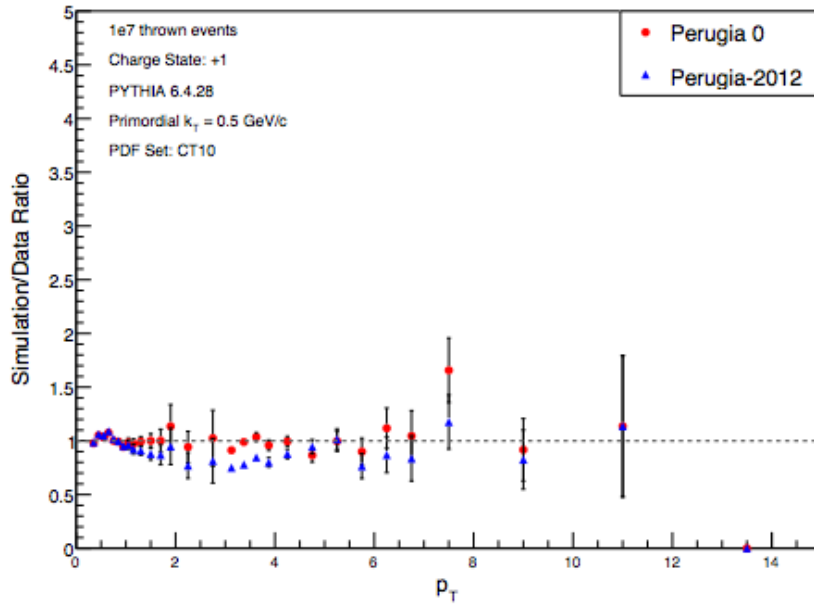
Figure A.6: The best PDF set for Perugia 0 and reduced k_T is CT10.

matches the theoretical curves much better than Perugia 2012. After this investigation we will choose Perugia 0 with PDF set CT10 and reduced k_T to generate the simulated data for the embedding analysis.
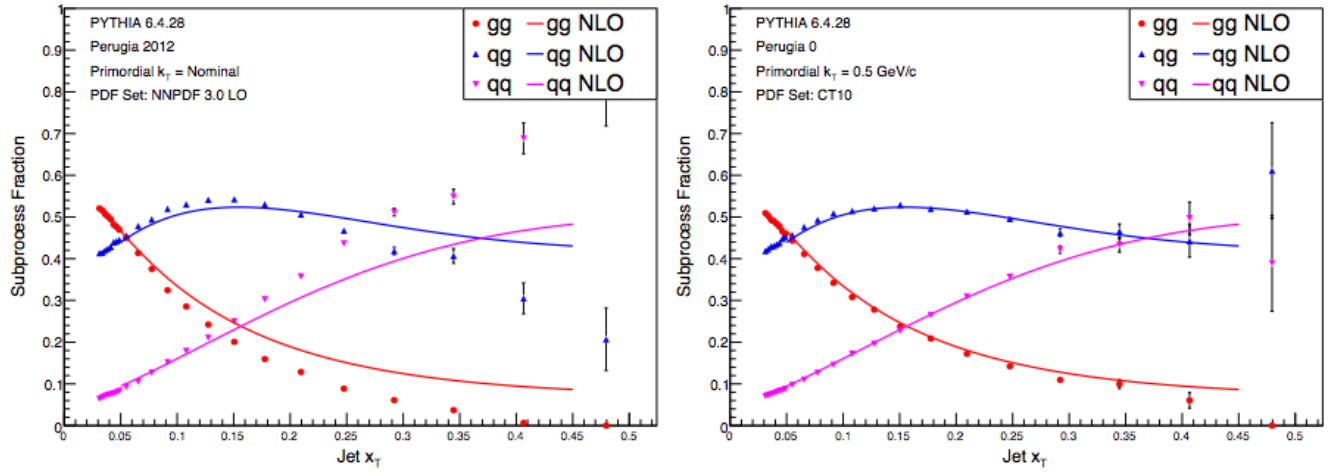
Figure A.7: Comparison of subprocess fractions from different pythia tunes. The CT10 tune with primordial $k_t = 0.5$ GeV/c (right) reproduces the NLO calculations better.

APPENDIX B

Trigger Bias and Embedding Analysis

The way the STAR triggers select events introduces a bias to our sample. It does this in two ways. First, it can trigger on quark jets and gluon jets in a different ratio than they are produced in the collisions. This is important to quantify because a theorist interpreting results from this analysis will assume the ratio of quark jets to gluon jets is consistent with their production ratio. To investigate how this affects the asymmetry we will start by revisiting Eqns. 6.2 through 6.5. It is convenient to introduce two variables $g = N_g/2\pi$ and $q = N_q/2\pi$, where N_g and N_q are the total number of pion pairs from gluons jets and quark jets at any angle ϕ_{RS}. Since pairs from gluons don't contribute to the asymmetry [31, 6], the number of gluon jets at any angle ϕ_{RS} is simply g. There is no sinusoidal modulation associated with pion pairs from gluons as you would see with pion pairs from fragmenting quarks. Using these two new variables, Eqns. 6.2 through 6.5 can be rewritten as:

$$N^{\uparrow}_{\phi_{RS}} = L^{\uparrow} I_{\phi_{RS}}(\theta) \left[g + q + q A_{UT} P \sin(\phi_{RS}) \right] \tag{B.1}$$

$$N^{\downarrow}_{\phi_{RS}} = L^{\downarrow} I_{\phi_{RS}}(\theta) \left[g + q - q A_{UT} P \sin(\phi_{RS}) \right] \tag{B.2}$$

$$N^{\downarrow}_{\phi_{RS}+\pi} = L^{\downarrow} I_{\phi_{RS}+\pi}(\theta) \left[g + q + q A_{UT} P \sin(\phi_{RS}) \right] \tag{B.3}$$

$$N^{\uparrow}_{\phi_{RS}+\pi} = L^{\uparrow} I_{\phi_{RS}+\pi}(\theta) \left[g + q - q A_{UT} P \sin(\phi_{RS}) \right] \tag{B.4}$$

By defining $\mathcal{L}$ and $\mathcal{R}$ in the same manner as before,

$$\frac{\mathcal{L} - \mathcal{R}}{\mathcal{L} + \mathcal{R}} = \frac{\sqrt{N^{\uparrow}_{\phi_{RS}} N^{\downarrow}_{\phi_{RS}+\pi}} - \sqrt{N^{\downarrow}_{\phi_{RS}} N^{\uparrow}_{\phi_{RS}+\pi}}}{\sqrt{N^{\uparrow}_{\phi_{RS}} N^{\downarrow}_{\phi_{RS}+\pi}} + \sqrt{N^{\downarrow}_{\phi_{RS}} N^{\uparrow}_{\phi_{RS}+\pi}}} = f_q^{detector} A_{UT} P \sin(\phi_{RS}) \qquad \text{(B.5)}$$

where $f_q^{detector} = \frac{q}{q+g}$ is the fraction of pion pairs originating from quarks after trigger selection has occurred. What was measured in the analysis should actually be thought of as $A_{UT}^{experiment} = f_q^{detector} A_{UT}$, where A_{UT} is now the "true" asymmetry due solely to pion pairs from fragmenting quarks.

The theorist will have a similar result,

$$\frac{\mathcal{L} - \mathcal{R}}{\mathcal{L} + \mathcal{R}} = \frac{\sqrt{N^{\uparrow}_{\phi_{RS}} N^{\downarrow}_{\phi_{RS}+\pi}} - \sqrt{N^{\downarrow}_{\phi_{RS}} N^{\uparrow}_{\phi_{RS}+\pi}}}{\sqrt{N^{\uparrow}_{\phi_{RS}} N^{\downarrow}_{\phi_{RS}+\pi}} + \sqrt{N^{\downarrow}_{\phi_{RS}} N^{\uparrow}_{\phi_{RS}+\pi}}} = f_q^{collision} A_{UT} P \sin(\phi_{RS}). \qquad \text{(B.6)}$$

This time $f_q^{collision}$ is the fraction of pion pairs originating from quarks before triggers are taken into account. Their perception of the asymmetry is $A_{UT}^{theory} = f_q^{collision} A_{UT}$. From this, it can be seen that

$$A_{UT}^{experiment} = \frac{f_q^{detector}}{f_q^{collision}} A_{UT}^{theory}. \qquad \text{(B.7)}$$

The values for $f_q^{detector}$ and $f_q^{collision}$ can be determined from simulated data. These are shown in Fig. B.1.

It turns out that, for the most part, there are about the same number pion pairs originating from quarks in the both triggered and untriggered samples. This is unexpected. It turns out that the triggered sample contains an increased number of $q_i q_j \to q_i q_j$ events and a decreased number of $gg \to gg$ events when compared to the untriggered sample, while maintaining roughly the same number of $q_i g \to q_i g$ events. This would seem to indicate there is a larger number of pairs from quarks, however the percentage of pairs matched with gluons in $q_i g \to q_i g$ events is about five percent higher in the triggered sample than the untriggered sample. This
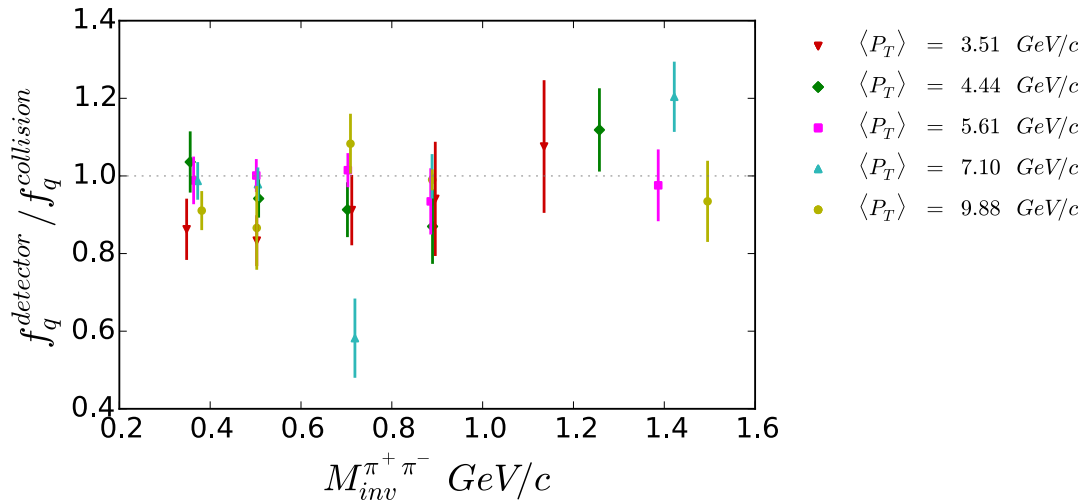
Figure B.1: Ratio of number of pairs coming from quarks to number coming from gluons (covers full η range)

effect seems to balance the effect of triggering on more $q_i q_j \rightarrow q_i q_j$ events and less $gg \rightarrow gg$ events.

The trigger also has a bias toward events coming from a parton carrying a high momentum fraction x. A quark with a large x will lead to outgoing products carrying more energy. These products will have a greater chance to be over the trigger threshold. This bias toward higher x events is shown in Fig. B.2.

There is also a bias introduced toward pairs carrying a lower momentum fraction, z, of the fragmenting parton. Because the triggers fire mainly on neutral energy, triggered pairs will belong to a jet with substantial neutral energy. Since so much energy from the fragmenting parton must be allocated to neutral energy, triggered pairs tend to carry a smaller momentum fraction. An untriggered pair does not need this requirement. The difference in z between triggered and untriggered pairs can be seen in Fig. B.3.
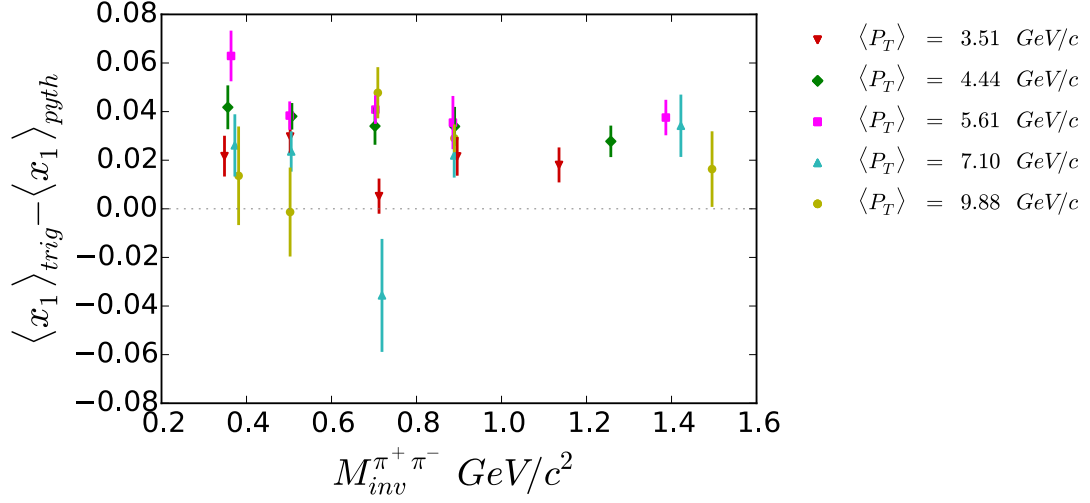
Figure B.2: The averge momentum fraction x of the parton from the polarized beam (beam 1) is larger for triggered events than for all events.
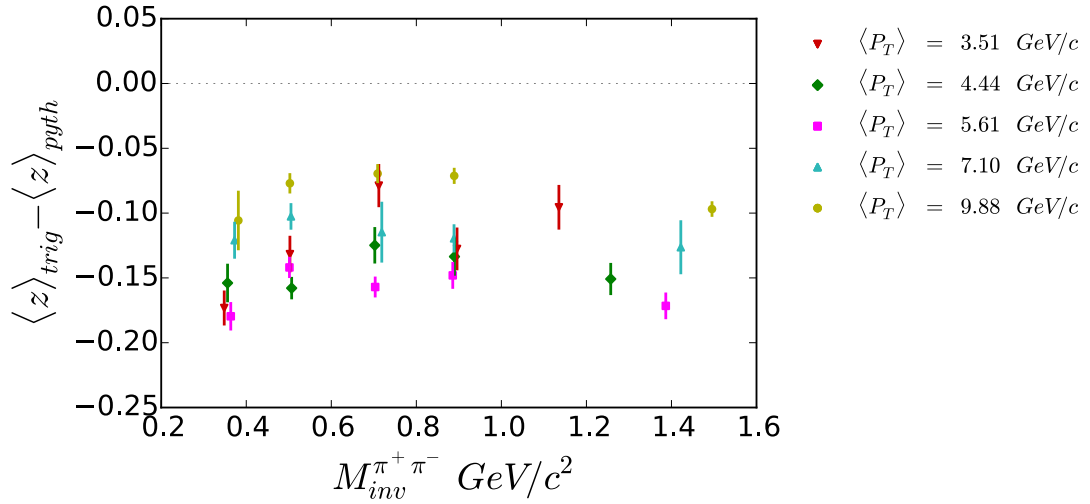

Figure B.3: The averge momentum fraction x of the polarized quark (quark 1) is larger for triggered events than for all events.
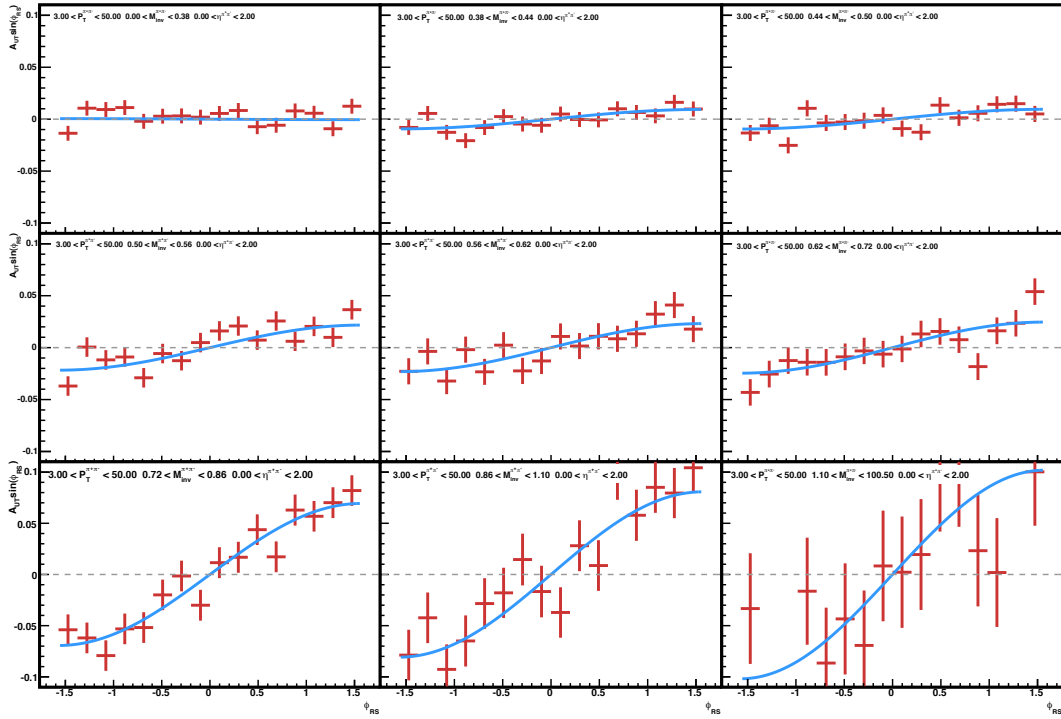
APPENDIX C

Sine fits for all results

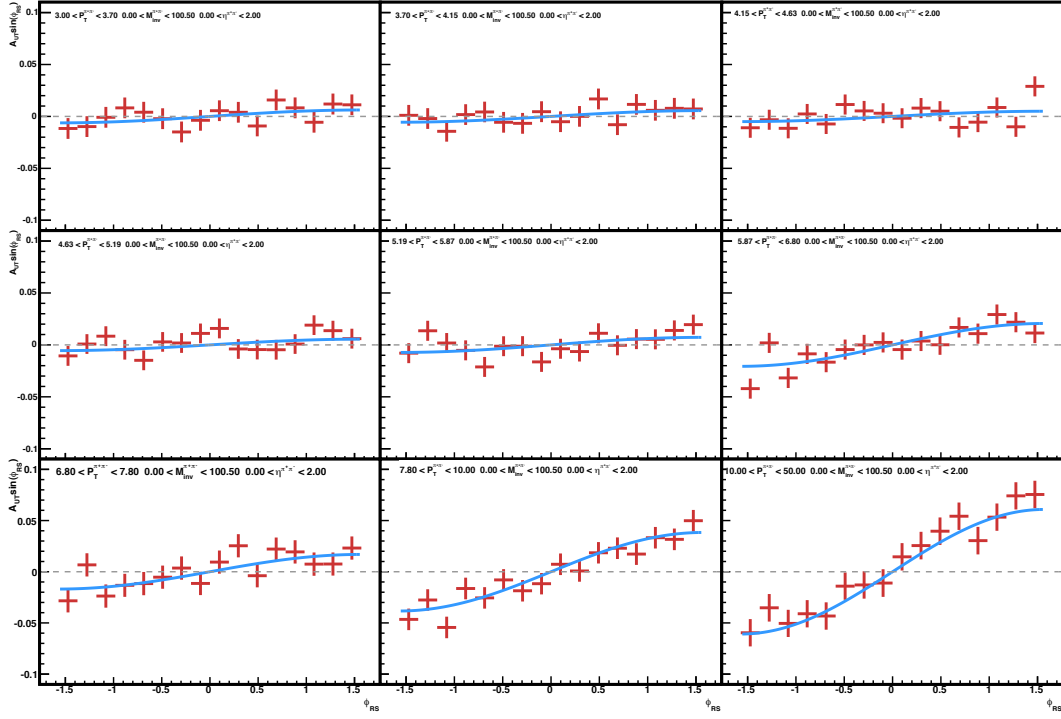Figure C.1: sine fits for different mass bins with radius cut 0.2, $\eta > 0$

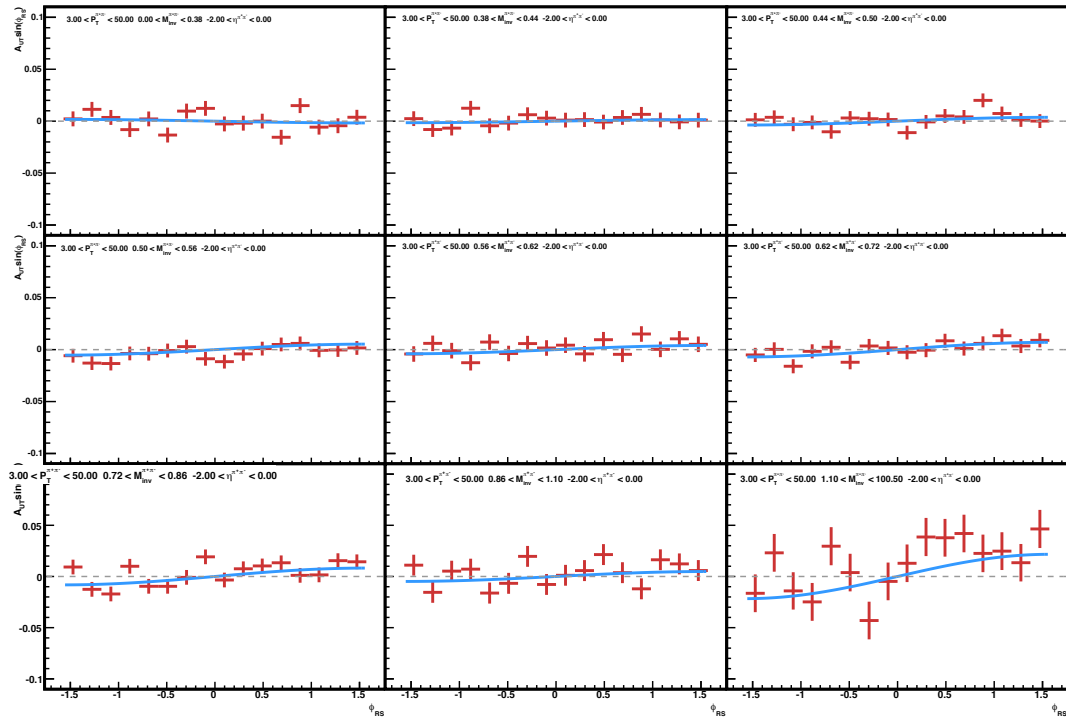Figure C.2: sine fits for different transverse momemtum bins with radius cut 0.2, $\eta > 0$

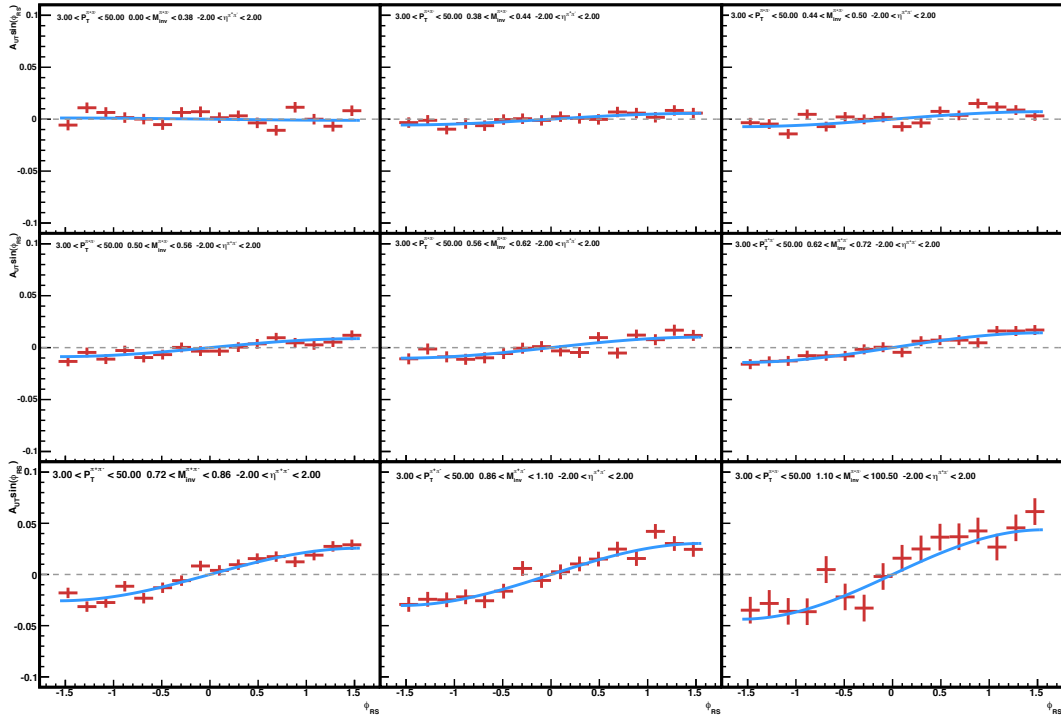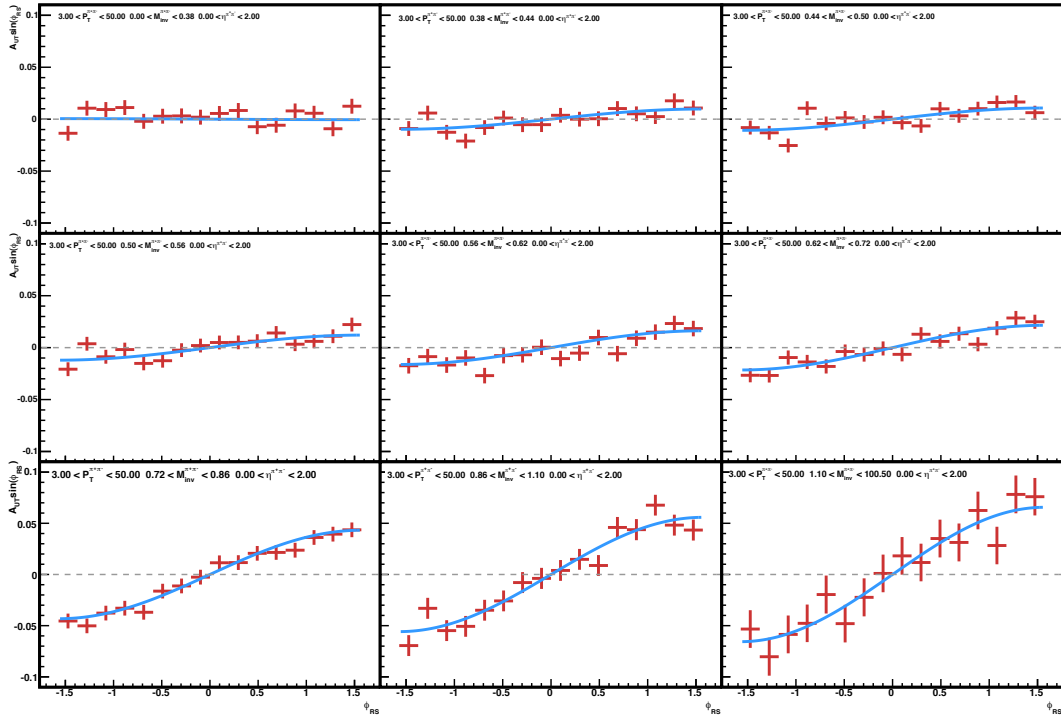Figure C.3: sine fits for different mass bins with radius cut 0.3, $\eta < 0$

Figure C.4: sine fits for different mass bins with radius cut 0.3

Figure C.5: sine fits for different mass bins with radius cut 0.3, $\eta > 0$

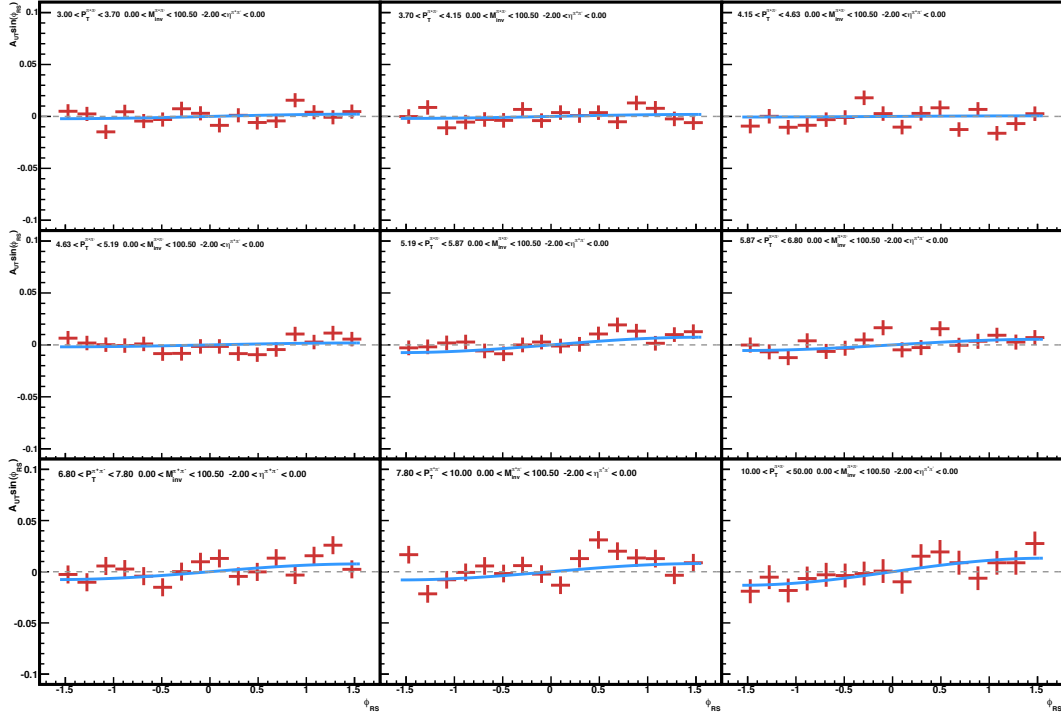Figure C.6: sine fits for different transverse momemtum bins with radius cut 0.3, $\eta < 0$
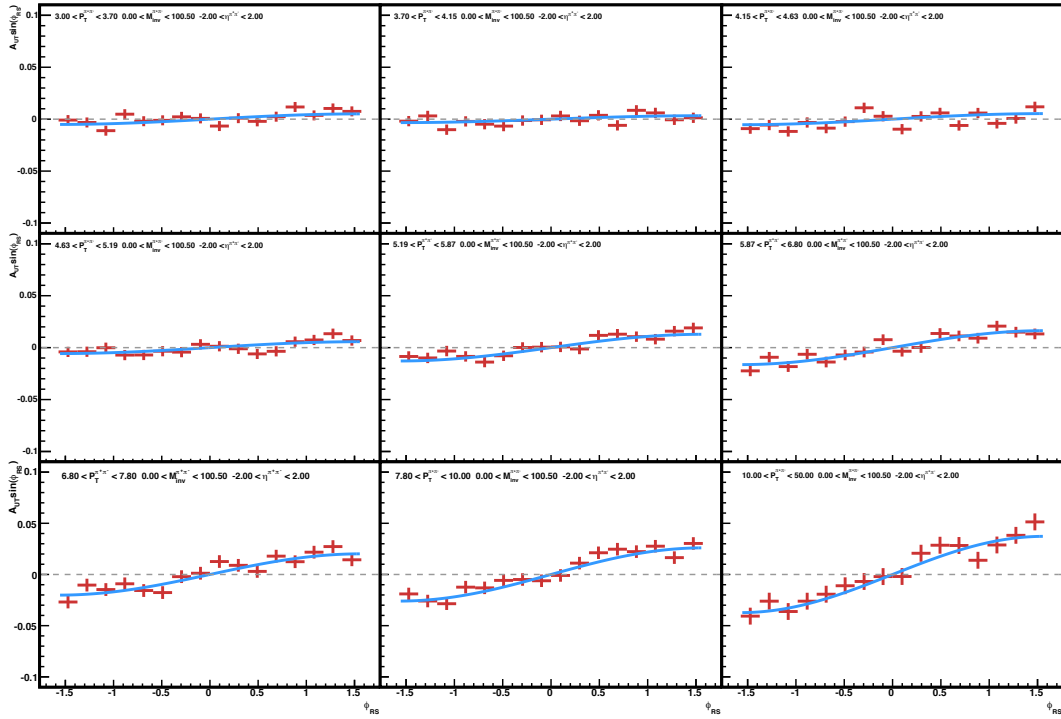
Figure C.7: sine fits for different transverse momemtum bins with radius cut 0.3
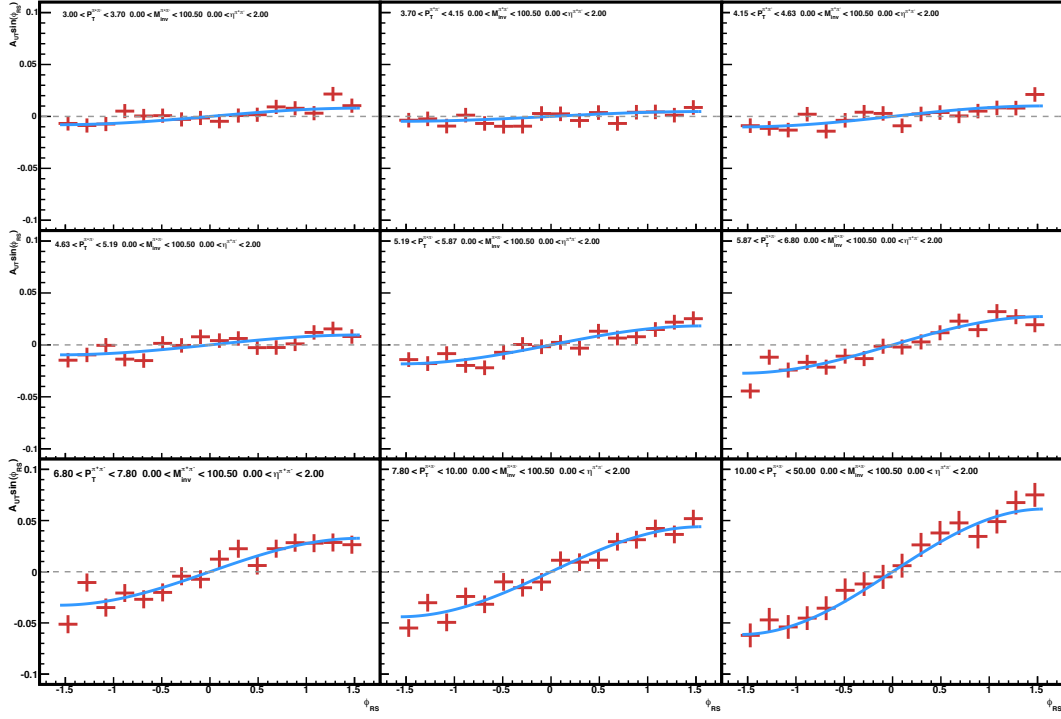
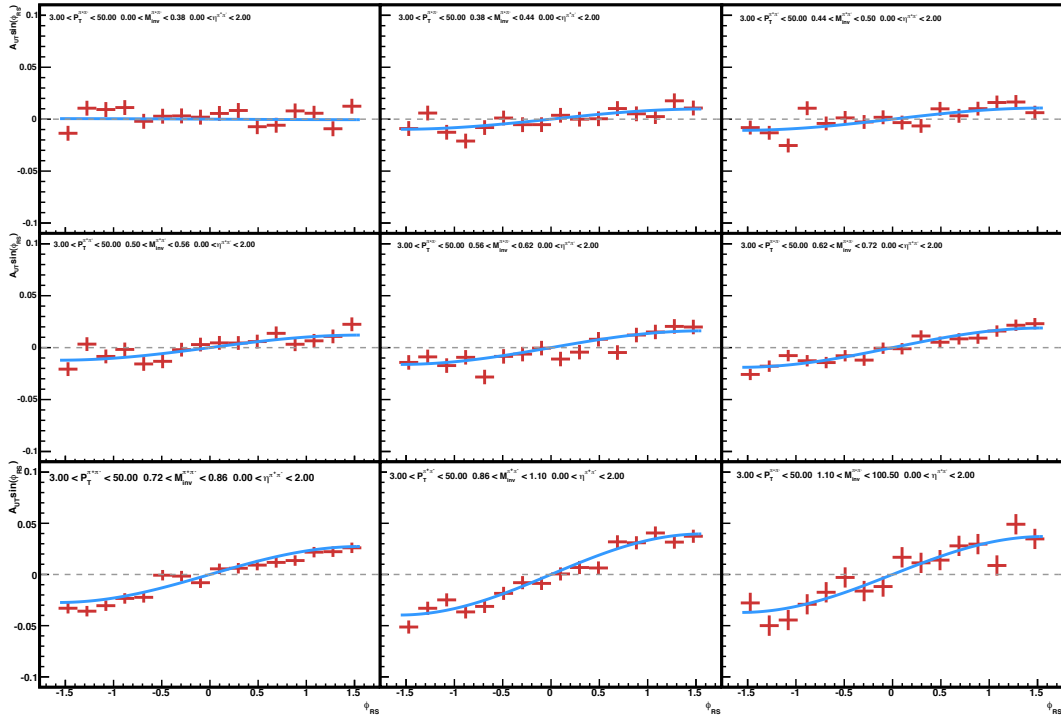Figure C.8: sine fits for different transverse momemtum bins with radius cut 0.3, $\eta > 0$

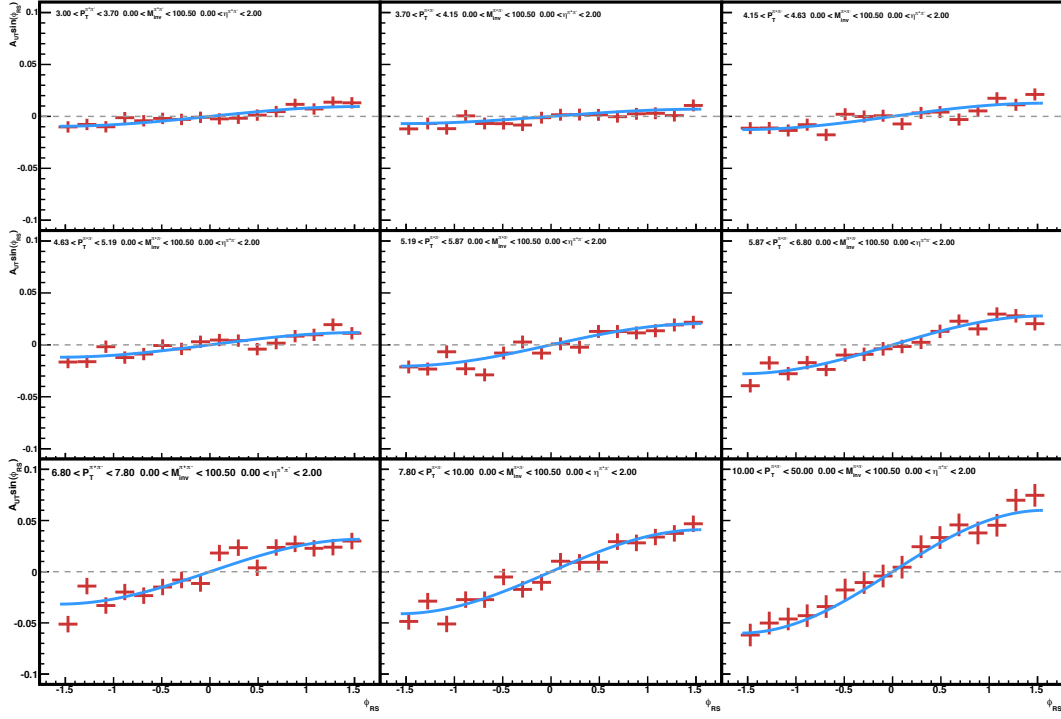Figure C.9: sine fits for different mass bins with radius cut 0.4, $\eta > 0$

Figure C.10: sine fits for different transverse momemtum bins with radius cut 0.4, $\eta > 0$
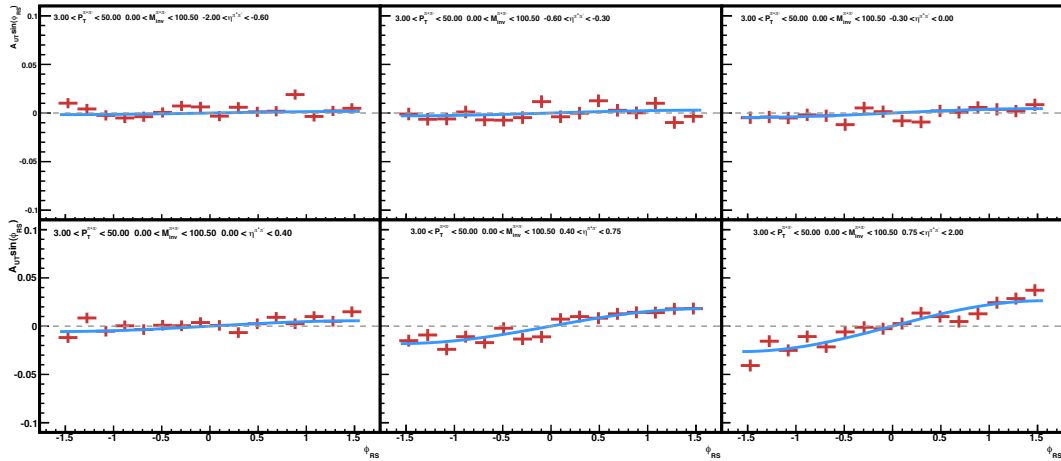

Figure C.11: sine fits for different pseudorapidity bins with radius cut 0.2
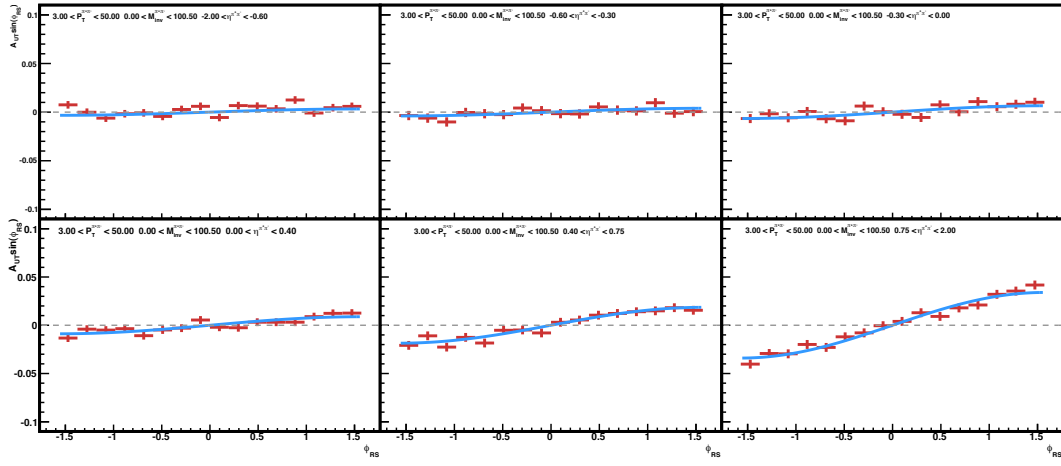
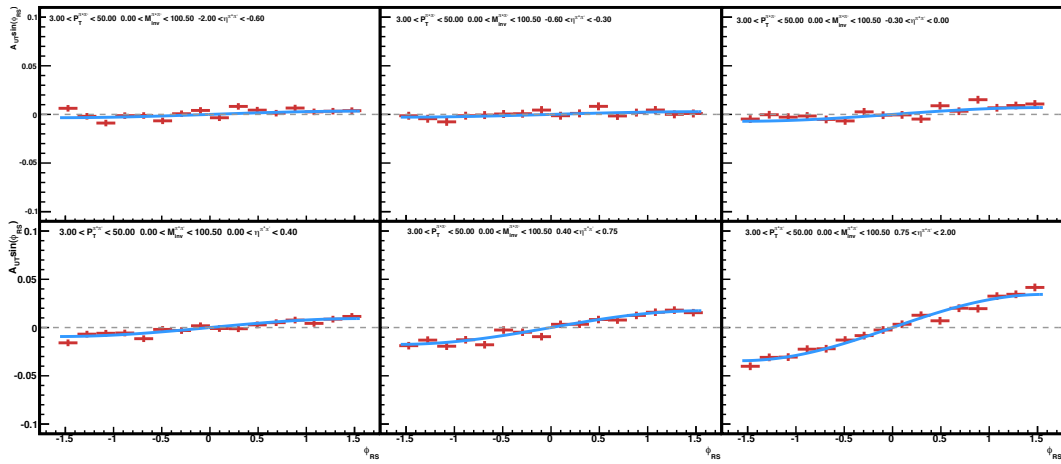Figure C.12: sine fits for different pseudorapidity bins with radius cut 0.3

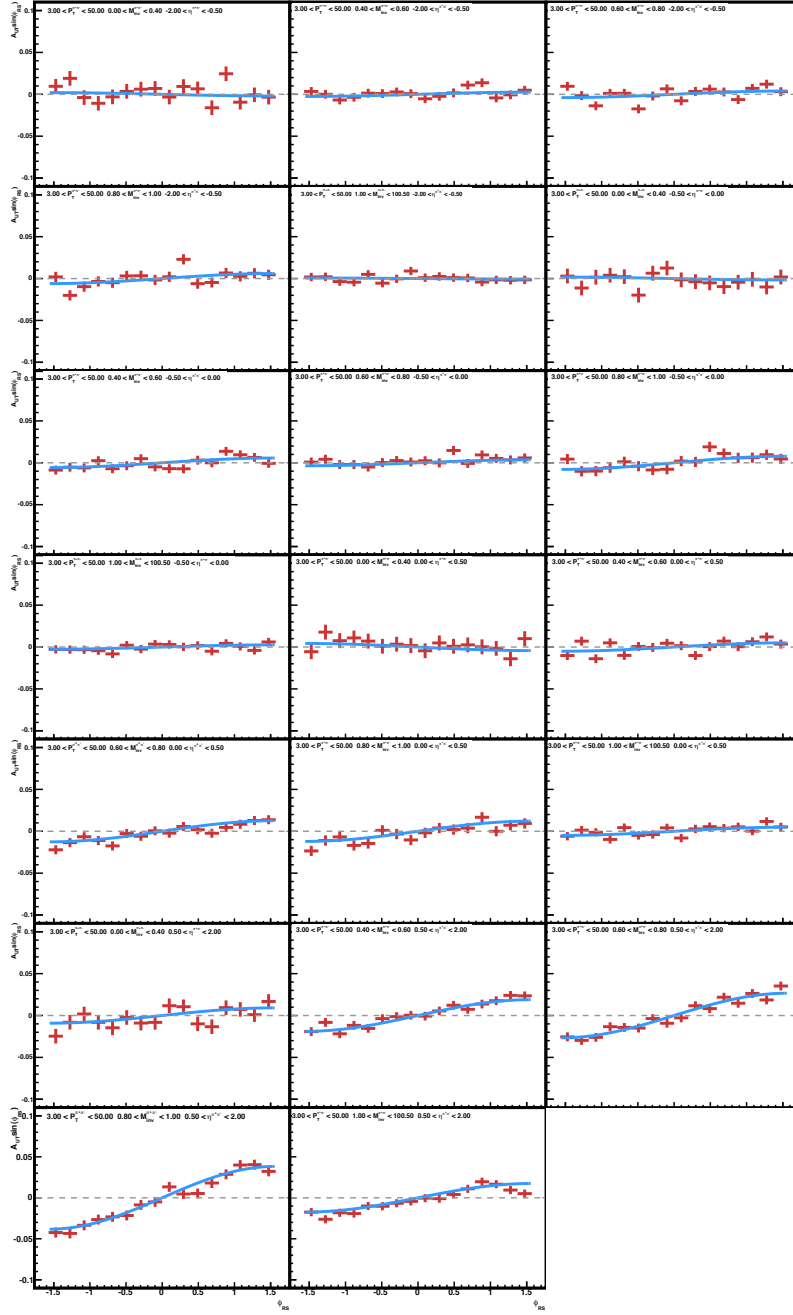Figure C.13: sine fits for different pseudorapidity bins with radius cut 0.4

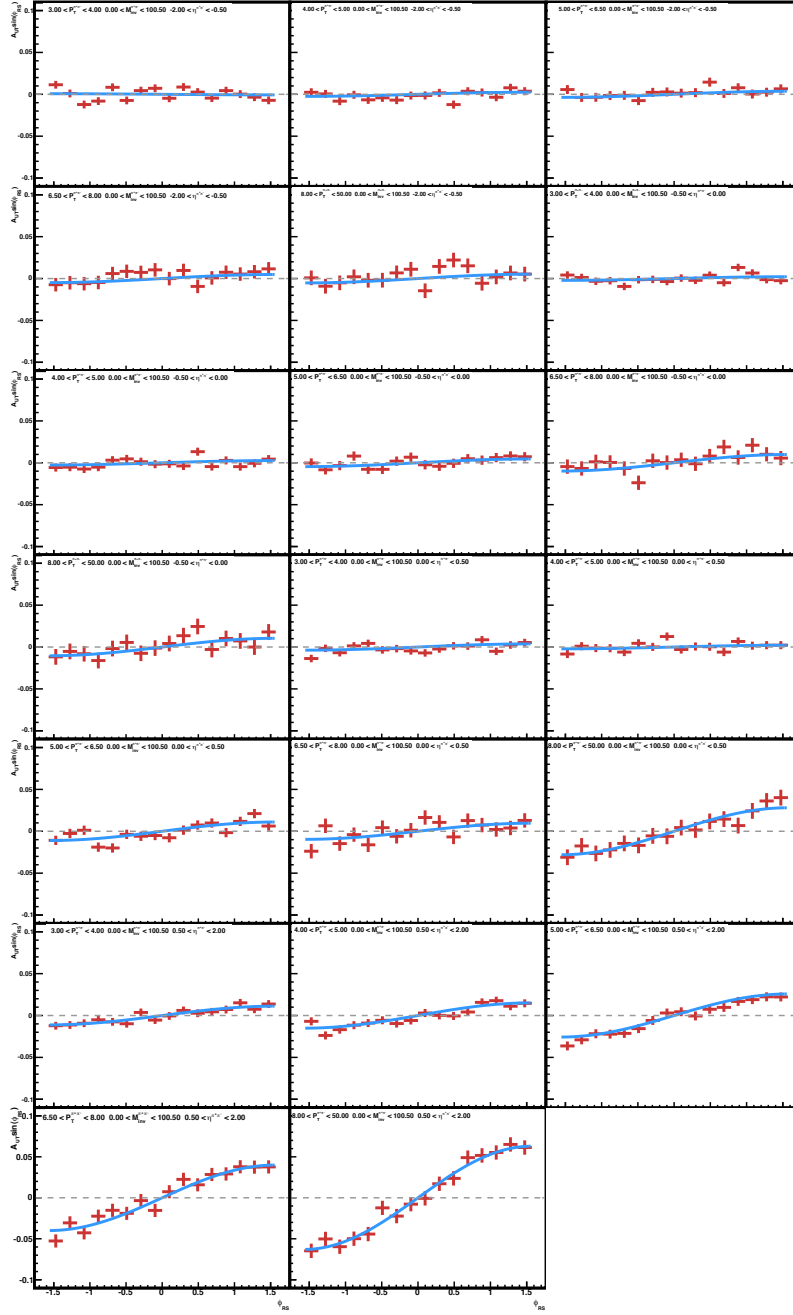Figure C.14: sine fits for 2D binning in invariant mass and pseudorapidity

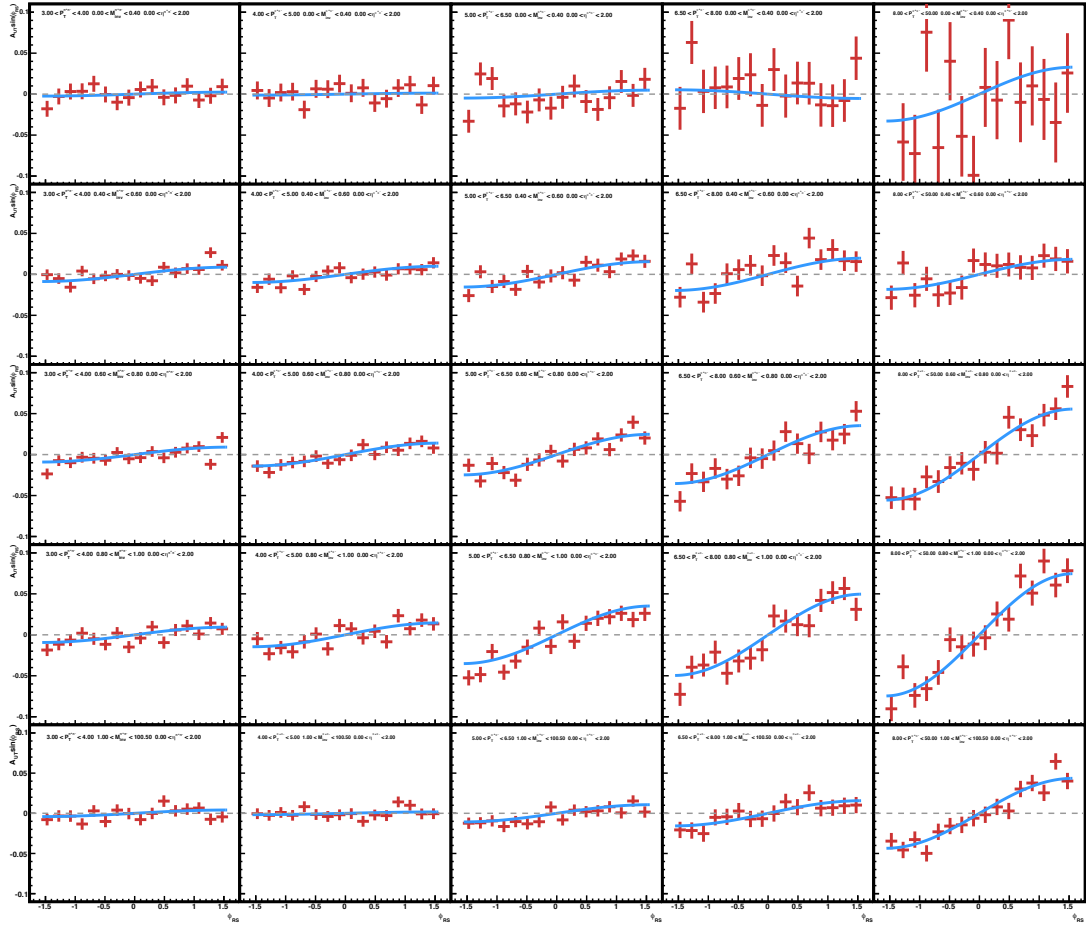Figure C.15: sine fits for 2D binning in transverse momentum and pseudorapidity

Figure C.16: sine fits for 2D binning in transverse momentum and invariant mass

Bibliography

[1] K. Abe et al. "Measurements of the proton and deuteron spin structure functions g(1) and g(2)". In: *Phys. Rev.* D58 (1998), p. 112003. DOI: 10. 1103/PhysRevD.58.112003. arXiv:hep-ph/9802357 [hep-ph].

[2] L. Adamczyk et al. "Observation of Transverse Spin-Dependent Azimuthal Correlations of Charged Pion Pairs in $p^\uparrow + p$ at $\sqrt{s} = 200$ GeV". In: *Phys. Rev. Lett.* 115 (24 2015), p. 242501. DOI: 10.1103/PhysRevLett.115. 242501. URL: http://link.aps.org/doi/10.1103/PhysRevLett.115. 242501.

[3] Stephen L. Adler and Wu-Ki Tung. "Breakdown of Asymptotic Sum Rules in Perturbation Theory". In: *Phys. Rev. Lett.* 22 (18 1969), pp. 978–981. DOI: 10.1103/PhysRevLett.22.978. URL: http://link.aps.org/doi/ 10.1103/PhysRevLett.22.978.

[4] A. Airapetian et al. "Measurement of the Proton Spin Structure Function g_1^p with a Pure Hydrogen Target". In: *Phys.Lett.B* 442 (1998), pp. 484–492. URL: http://arxiv.org/abs/hep-ex/9807015v1.

[5] A. Airapetian et al. "Single-spin asymmetries in semi-inclusive deep-inelastic scattering on a transversely polarized hydrogen target". In: *Phys. Rev. Lett.* 94 (2005), p. 012002. DOI: 10.1103/PhysRevLett.94.012002. arXiv:hep-ex/0408013 [hep-ex].

[6] Marco Radici Alessandro Bacchetta. "Dihadron interference fragmentation functions in proton-proton collisions". In: *Phys. Rev. D* 70 (3 2004). URL: DOI:10.1103/PhysRevD.70.094032.

[7] M. Anderson et al. "The STAR time projection chamber: a unique tool for studying high multiplicity events at RHIC". In: *Nuclear Instruments*

and Methods in Physics Research A 499 (2003), pp. 659–678. URL: `http://arxiv.org/abs/nucl-ex/0301015`.

[8]   M. Anselmino et al. "Transversity and Collins functions from SIDIS and e+ e- data". In: *Phys. Rev.* D75 (2007), p. 054032. DOI: `10.1103/PhysRevD.75.054032`. arXiv:`hep-ph/0701006` [hep-ph].

[9]   F. Arbabifar et al. "Symmetry breaking effect on determination of polarized and unpolarized parton distributions". In: (2012). [Nucl. Phys. Proc. Suppl.234,66(2013)]. DOI: `10.1016/j.nuclphysbps.2012.11.016`. arXiv:1208.5234 [hep-ph].

[10]   Marco Radici Aurore Courtoy Alessandro Bacchetta and Andrea Bianconi. "First extraction of Interference Fragmentation Functions from e^+e data". In: *Phys.Rev.D* 85 (2012). URL: `http://arxiv.org/abs/1202.0323`.

[11]   Alessandro Bacchetta. "Probing the Transverse Spin of Quarks in Deep Inelastic Scattering". PhD thesis. Vrije U., Amsterdam, 2002. arXiv:`hep-ph/0212025` [hep-ph]. URL: `https://inspirehep.net/record/594456/files/arXiv:hep-ph_0212025.pdf`.

[12]   Alessandro Bacchetta and Marco Radici. "Partial wave analysis of two hadron fragmentation functions". In: *Phys. Rev.* D67 (2003), p. 094002. DOI: `10.1103/PhysRevD.67.094002`. arXiv:`hep-ph/0212300` [hep-ph].

[13]   Vincenzo Barone, Alessandro Drago, and Philip G. Ratcliffe. "Transverse polarisation of quarks in hadrons". In: *Phys. Rept.* 359 (2002), pp. 1–168. DOI: `10.1016/S0370-1573(01)00051-5`. arXiv:`hep-ph/0104283` [hep-ph].

[14]   M. Beddoa et al. "The STAR Barrel Electromagnetic Calorimeter". In: *Nuclear Instruments and Methods in Physics Research A* 499 (2003), pp. 725–739. URL: `http://dx.doi.org/10.1016/S0168-9002(02)01970-8`.

[15] A. Bianconi et al. "Two hadron interference fragmentation functions. Part 1. General framework". In: *Phys. Rev.* D62 (2000), p. 034008. DOI: `10.1103/PhysRevD.62.034008`. arXiv:`hep-ph/9907475 [hep-ph]`.

[16] HERMES Collaboration. "Evidence for a transverse single-spin asymmetry in leptoproduction of $\pi^+\pi^-$ pairs". In: *Journal of High Energy Physics* 0806 (2008), p. 017. URL: `http://arxiv.org/abs/0803.2367`.

[17] The COMPASS Collaboration. "Transverse spin effects in hadron-pair production from semi-inclusive deep inelastic scattering". In: *Phys. Lett. B* 713 (2012), pp. 10–16. URL: `http://arxiv.org/abs/1202.6150`.

[18] The STAR Collaboration. "RHIC Beam Use Request For Runs 13 and 14". In: May (2012).

[19] The STAR TOF Collaboration. "Proposal for a Large Area Time of Flight System for STAR". In: (2004).

[20] John C. Collins, Davison E. Soper, and George F. Sterman. "Factorization of Hard Processes in QCD". In: *Adv. Ser. Direct. High Energy Phys.* 5 (1989), pp. 1–91. DOI: `10.1142/9789814503266_0001`. arXiv:`hep-ph/0409313 [hep-ph]`.

[21] Aurore Courtoy et al. "First extraction of Interference Fragmentation Functions from e^+e^- data". In: *Phys. Rev.* D85 (2012), p. 114023. DOI: `10.1103/PhysRevD.85.114023`. arXiv:`1202.0323 [hep-ph]`.

[22] A.V. Efremov, L. Mankiewicz, and N.A. Trnqvist. "Jet handedness as a measure of quark and gluon polarization". In: *Physics Letters B* 284.3 (1992), pp. 394 –400. ISSN: 0370-2693. DOI: `http://dx.doi.org/10.1016/0370-2693(92)90451-9`. URL: `http://www.sciencedirect.com/science/article/pii/037026939290451.`

[23] Daniel de Florian et al. "Evidence for polarization of gluons in the proton". In: *Phys. Rev. Lett.* 113.1 (2014), p. 012001. DOI: `10.1103/PhysRevLett.113.012001`. arXiv:`1404.4293 [hep-ph]`.

[24] David Griffiths. *Introduction to Elementary Particles.* Germany: Wiley-Vch, 2004.

[25] David J. Gross. "Asymptotic freedom and the emergence of QCD". In: *The Rise of the standard model: Particle physics in the 1960s and 1970s. Proceedings, Conference, Stanford, USA, June 24-27, 1992.* 1992, pp. 199–232. arXiv:`hep-ph/9210207 [hep-ph]`.

[26] I.Alekseev et al. "Polarized proton collider at RHIC". In: *Nuclear Instruments and Methods in Physics Research A* 499 (2003), pp. 392–414. URL: `http://dx.doi.org/10.1016/S0168-9002(02)01946-0`.

[27] R. L. Jaffe. "Can transversity be measured?" In: *Deep inelastic scattering off polarized targets: Theory meets experiment. Physics with polarized protons at HERA. Proceedings, Workshops, SPIN'97, Zeuthen, Germany, September 1-5, 1997 and Hamburg, Germany, March-September 1997.* 1997. arXiv:`hep-ph/9710465 [hep-ph]`. URL: `http://alice.cern.ch/format/showfull?sysnb=0260728`.

[28] R. L. Jaffe. "The Theory of the nucleon spin". In: *Phil. Trans. Roy. Soc. Lond.* A359 (2001), pp. 391–404. DOI: `10.1098/rsta.2000.0731`. arXiv:`hep-ph/0008038 [hep-ph]`.

[29] R. L. Jaffe, Xuemin Jin, and Jian Tang. "Interference Fragmentation Functions and the Nucleon's Transversity". In: *Phys. Rev. Lett.* 80 (6 1998), pp. 1166–1169. DOI: `10.1103/PhysRevLett.80.1166`. URL: `http://link.aps.org/doi/10.1103/PhysRevLett.80.1166`.

[30] Robert L. Jaffe. "Spin, twist and hadron structure in deep inelastic processes". In: *The spin structure of the nucleon. Proceedings, International School of Nucleon Structure, 1st Course, Erice, Italy, August 3-10, 1995.* 1996, pp. 42–129. arXiv:hep-ph/9602236 [hep-ph].

[31] Robert L. Jaffe. "Spin, twist and hadron structure in deep inelastic processes". In: (1996). [Lect. Notes Phys.496,178(1997)]. DOI: 10.1007/BFb0105860. arXiv:hep-ph/9602236 [hep-ph].

[32] Robert L. Jaffe. "Where Does the Proton Really Get Its Spin?" In: (1995).

[33] S. Ozaki M. Harrison T. Ludlam. "RHIC project overview". In: *Nuclear Instruments and Methods in Physics Research A* 499 (2003), pp. 235–244. URL: http://dx.doi.org/10.1016/S0168-9002(02)01937-X.

[34] Gerald G. Ohlsen and P.W. Keaton Jr. "Techniques for Measurement of spin-$\frac{1}{2}$ and spin-1 Polarization Analyzing Tensors". In: *Nuclear Instuments and Methods* 109 (1973), pp. 41–59.

[35] Marco Radici et al. "Exploring universality of transversity in proton-proton collisions". In: (2016). arXiv:1604.06585 [hep-ph].

[36] Marco Radici et al. "Improved extraction of valence transversity distributions from inclusive dihadron production". In: *JHEP* 05 (2015), p. 123. DOI: 10.1007/JHEP05(2015)123. arXiv:1503.03495 [hep-ph].

[37] Marco Radici et al. "Realistic estimate of valence transversity distributions from inclusive dihadron production". In: (2015).

[38] John P. Ralston and Davison E. Soper. "Production of dimuons from high-energy polarized proton-proton collisions". In: *Nuclear Physics B* 152 (1979), pp. 109–124. URL: http://dx.doi.org/10.1016/S0168-9002(02)01946-0.

[39] Burkard Reisert, Agustin Sabio Vera, and Zhiqing Zhang. "Structure Functions and Low-x: Working Group Summary". In: *Proceedings, 17th International Workshop on Deep-Inelastic Scattering and Related Subjects (DIS 2009): Madrid, Spain, April 26-30, 2009.* 2009. arXiv:0908.2194 [hep-ex]. URL: https://inspirehep.net/record/828715/files/arXiv:0908.2194.pdf.

[40] P. Z. Skands. "Tuning Monte Carlo Generators: The Perugia Tunes". In: *PhysRevD* 82 (2010). URL: http://arxiv.org/abs/1005.3457v5.

[41] Jian Tang. "Probing the Nucleon's Transversity Via Two-Meson Production in Polarized Nucleon-Nucleon Collisions". In: *Submitted to Phys. Rev. D* (1998). URL: arXiv:hep-ph/9807560.

[42] A. Vossen et al. "Observation of Transverse Polarization Asymmetries of Charged Pion Pairs in e^+e^- Annihilation near $\sqrt{s} = 10.58$ GeV". In: *Phys. Rev. Lett.* 107 (7 2011), p. 072004. DOI: 10.1103/PhysRevLett.107.072004. URL: http://arxiv.org/abs/1104.2425.